IN SITU STRESS EVOLUTION ON AN Au THIN FILM CATHODE ELECTRODE DURING DISCHARGING/CHARGING IN LITHIUM-OXYGEN BATTERIES

By

HANNAH DYKES

Bachelor of Science in Chemical Engineering

University of Kentucky

Lexington, KY

2019

Submitted to the Faculty of the
Graduate College of the
Oklahoma State University
in partial fulfillment of
the requirements for
the Degree of
MASTER OF SCIENCE
December, 2021

IN SITU STRESS EVOLUTION ON AN Au THIN FILM CATHODE ELECTRODE DURING DISCHARGING/CHARGING IN LITHIUM-OXYGEN BATTERIES

Thesis Approved:

Dr. Omer Ozgur Capraz

Thesis Adviser

Dr. Jindal Shah

Dr. Jeff White

Dr. Mari Andiappan

ACKNOWLEDGEMENTS

I would like to thank my fellow graduate student lab members, Bertan Ozdogru and Darrell Gregory for all their help and support throughout my time at OSU. I would also like to thank my family for motivating me to overcome research challenges I faced as well.

Name: HANNAH DYKES

Date of Degree: DECEMBER, 2021

Title of Study: IN SITU STRESS EVOLUTION ON AN Au THIN FILM CATHODE ELECTRODE DURING DISCHARGING/CHARGING IN LITHIUM-OXYGEN BATTERIES

Major Field: CHEMICAL ENGINEERING

Abstract: Li-O_2 batteries have over ten times the theoretical energy density that current Li-ion batteries have, but their practical energy density is hindered by a low cycle life, rapid capacity fade, and the high overpotential needed to oxidize the primary discharge product. The primary bottleneck preventing the commercialization of Li-O_2 batteries are issues related to the cathode. The slow reaction kinetics occurring during cycling lead to an irreversible accumulation of the insulating primary discharge product, lithium peroxide (Li_2O_2), on the cathode surface. This accumulation can lead to the passivation of the cathode surface. Many studies have focused on improving the reaction kinetics and investigating the driving forces behind the chemical instabilities of both the cathode surface and the electrolyte, but few studied have examined the mechanical implications that result from these chemical instabilities as well as the formation and decomposition of the Li_2O_2 discharge product. To fill this gap in knowledge, the surface deformation that occurs on the cathode surface during both the formation and removal of the Li_2O_2 product has been studied. The formation and decomposition of Li_2O_2 involves a series of complex reactions that are still being studied. Li_2O_2 is formed during discharging by either a solution or a surface-based reaction pathway. The dynamic chemo-mechanical changes occurring on the cathode surface will be monitored during cycling and this information will be linked to the redox potentials. To elucidate these changes occurring on the cathode surface, a new experimental technique was developed by utilizing a kSA Multi-beam optical sensor (MOS) to monitor the in-situ stress evolution that results during cycling. These stress measurements were synchronized with the electrochemical response of the electrodes during cycling. Electrolytes with different salts and solvents were used to compare the stress evolution occurring with the expected discharge reaction pathway that results. During discharging the cathode experienced stress evolution due to the formation of Li_2O_2, while the cathode experienced stress evolution due the removal of Li_2O_2 during charging. The sign and behavior of the stress shows the dependance on the electrolyte chemistry, which indicates the fundamental differences between surface versus solution-based reaction processes.

TABLE OF CONTENTS

Chapter Page

I. INTRODUCTION TO LITHIUM-OXYGEN BATTERIES 1

1.1 Outline of Thesis 1
1.2 Motivation behind the Commercialization of Battery Technologies 2
1.3 Introduction to Lithium-ion Batteries 4
1.4 Electrochemistry of Lithium-ion Batteries 4
1.5 Introduction to Lithium-Oxygen Batteries 5
1.5.1 Current Issues existing in Lithium-Oxygen Batteries 6
1.5.2 Electrochemistry of Lithium-Oxygen Batteries 8
1.5.3 Overview of Various Lithium-Oxygen Batteries 11
1.5.4 Overview of Cathode Materials 12
1.5.5 Overview of Parasitic Reaction Species 14
1.5.6 Lithium Peroxide Formation Mechanism during Discharging in Nonaqueous Solvents 16
1.5.7 Proposed Mechanisms for the Decomposition of Lithium Peroxide 20
1.5.8 Overview of Nonaqueous Solvents used in Lithium-Oxygen Batteries 21
1.5.9 Overview of Lithium Salts used in Lithium-Oxygen Batteries 23
1.6 Proposed Study 23

II. INTRODUCTION TO ELECTROCHEMICAL SYSTEMS AND STRESS 25

2.1 Introduction to Electrochemical Systems 25
2.2 Introduction to Terminology 27
2.3 Introduction to Electrochemical Techniques 28
2.3.1 Cyclic Voltammetry 28
2.3.2 Linear Sweep Voltammetry 30
2.3.3 Galvanostatic Cycling 31
2.3.4 Electrochemical Impedance Spectroscopy 32
2.4 Introduction to Stress 35
2.5 Techniques to Monitor Curvature 37
2.6 Investigation into the Origin of Stress Evolution 39
2.6.1 Island Coalescence 39
2.6.2 The Deposition of Nuclei at Grain Boundaries 39

Chapter Page

III. IN SITU STRESS MEASUREMENTS ON A THIN FILM Au CATHODE DURING THE FIRST DISCHARGE OF LI-O2 BATTERIES 43

3.1 Introduction 45
3.2 Experimental 47
3.2.1 Electrochemical Cycling 47
3.2.2 Curvature Measurement Technique 49
3.2.3 Electrochemical Custom Cell Design 50
3.3 Results and Discussion 52
3.3.1 Stress evolution on an Au anode in a Li-ion Battery 52
3.3.2 Stress evolution during the formation of Li_2O_2 54
3.3.3 Surface stress measurements on an Au cathode in oxygen vs argon-saturated electrolytes 57
3.4 Discussion 58
3.5 Conclusions 61

IV. THE IMPACT OF THE LITHIUM SALT/SOLVENT CHOICE ON THE STRESS EVOLUTION DURING CYCLING IN LITHIUM OXYGEN BATTERIES 63

4.1 Introduction 65
4.2 Experimental 65
4.3 Results 67
4.3.1 Stress Development during Discharging 67
4.3.2 Stress Development during Charging 73
4.4 Conclusions 75

V. FUTURE WORK 77
5.1 Future Work 77

REFERENCES 79

APPENDICES 100
APPENDIX A: Supplemental Information for In Situ Stress Measurements on Thin Film Au Cathode during First Discharge of Li-O_2 Batteries 100
APPENDIX B: Elucidating Cycling Rate-Dependent Electrochemical Strains in Sodium Iron Phosphate Cathodes for Na-ion Batteries 105
APPENDIX C: Standard Operating Procedure for the Operation of the kSA Multi-beam Optical Sensor (MOS) Curvature Measurement Technique 120
APPENDIX D: Standard Operating Procedure for the Assembly of the Custom Electrochemical Cell 131

LIST OF TABLES

Table Page

1. Donor Number of Commonly Used Li-O_2 Nonaqueous Solvents 22
B1. Average concentration in the electrode particle $\bar{C}_{ave}$, and mismatch strains in the particle along a-axis ($\varepsilon_{a,ave}$) and b-axis ($\varepsilon_{b,ave}$) 113
B2. Material Properties of the Composite Electrode Matrix 117
B3. Nomenclature for Equations 119

LIST OF FIGURES

Figure Page

1. Global net electricity generation and carbon dioxide emissions 2
2. Practical vs Theoretical Energy Density for various battery configurations. 3
3. Schematic of a Lithium-ion Battery 5
4. Schematic of a Nonaqueous Lithium-Oxygen Battery 6
5. The Capacity of Li-O_2 Batteries with and without redox mediators 8
6. Schematic of Various Lithium-Oxygen Battery Systems 10
7. Representation of the stability issues of carbon cathodes during cycling 15
8. Representation of Li_2O_2 Formation Pathways 17
9. Representation of the variables affecting the Li_2O_2 morphology during discharge 18
10. Morphology of Li_2O_2 at low current density and high current density 19
11. Representation of a Rechargeable Battery 26
12. Schematic of the potential versus time in a cyclic voltammogram 29
13. Current density versus potential for a cyclic voltammogram 29
14. Schematic of the potential versus time during linear sweep voltammetry 30
15. Schematic of the current evolution during galvanostatic cycling 31
16. One full galvanostatic cycle of a gold cathode vs a lithium anode in a 1 M $LiNO_3$ in DMSO electrolyte solution at an applied current of 10 µA/cm2 32
17. Randle's circuit to model the electrical response of electrochemical systems 33
18. Representation of an Electrochemical Impedance Spectroscopy plot 35
19. Depiction of compressive stress versus tensile stress in materials 38
20. Depiction of stress-thickness evolution with respect to the thickness of the film 41
21. Picture of the custom electrochemical cell designed for in situ curvature monitoring while cycling Li-ion or Li-O_2 batteries 51
22. The current density, stress generation, and the first derivative of the stress during the third cycle on Au anode in 1 M $LiClO_4$ in PC at 1 mV/s (under Argon environment).53

Figure Page

23. The stress-thickness product development prior to (red line) and during (black line) the oxygen reduction reaction on the Au cathode cycled in 1 M $LiNO_3$ in Diglyme. The cathode was discharged either by linear sweep voltammetry (A-E) starting from the open circuit potential down to 2.0 V by decreasing it by 1 mV/s or via galvanostatic cycling (F-G) at a constant current of -10 μAcm-2 for one hour. (A, B and C) show the potential, current density and stress-thickness plotted against time. (D and E) demonstrates the current density and stress-thickness product plotted against the potential during linear sweep voltammetry only. (F and G) shows the potential and stress-thickness product plotted against discharge capacity..... 56
24. The current response and stress generation on Au cathode during linear sweep voltammetry at 1 mV/s rate until 2.0V A) in oxygen-saturated (blue) or argon-saturated (grey) $LiNO_3$ in Diglyme electrolyte B) in an oxygen-saturated (blue) or argon-saturated (grey) $LiNO_3$ in DMSO electrolyte..... 58
25. The current response and the force development during discharge cycles 1-4 on the Au cathode cycled in an oxygen-saturated electrolyte of 1 M LiTFSI in DMSO (A and C) and 1 M $LiNO_3$ in DMSO (B and D). Cyclic Voltammetry was conducted from 2-4.1 V for LiTFSI in DMSO (A and C) at 1 mV/s and from 2-4.4 V for 1 M $LiNO_3$ in DMSO (B and D) at the same scan rate. The force was set to zero at the onset of each discharge cycle for Figures A and B. Figures C and D show the current response and the force development from 2-3.2 V for cycles 2-4 for LiTFSI and $LiNO_3$, respectively. The force was set to zero at 3.2 V in Figures C and D to show the complex behaviors in this potential regime..... 68
26. The current response and the force development during the third discharge cycle on the Au cathode cycled in an argon-saturated electrolyte (red line) and an oxygen-saturated electrolyte (blue) of 1 M LiTFSI in DMSO (A) and 1 M $LiNO_3$ in DMSO (B). Cyclic Voltammetry was conducted from 2-4.1 V for LiTFSI in DMSO (A) at 1 mV/s and from 2-4.4 V for 1 M $LiNO_3$ in DMSO (B) at the same scan rate. The force was set to zero at 3.2 V to show the complex behaviors in this potential regime. 70
27. The current response and the first derivative of the force with respect to the applied potential during the 2-4 discharge cycles on the Au cathode cycled in an oxygen-saturated electrolyte (A and C) and an argon-saturated electrolyte (B and D) of 1 M LiTFSI in DMSO (A and B) and 1 M $LiNO_3$ in DMSO (C and D). Cyclic Voltammetry was conducted from 2-4.1 V at 1 mV/s for LiTFSI in DMSO (A and B) and from 2-4.4 V for 1 M LiNO3 in DMSO (C and D)..... 71
28. The current response and force development during charge cycles 1-4 on the Au cathode cycled in an oxygen-saturated 1 M LiTFSI in DMSO (A) and 1 M $LiNO_3$ in DMSO (B) electrolyte. Cyclic Voltammetry was conducted from 2-4.1 V at 1 mV/s for LiTFSI in DMSO (A) and from 2-4.4 V for 1 M $LiNO_3$ in DMSO (B). The force was set to zero at the onset of each charge cycle for Figures A and B..... 73
29. The current response and the force development during charge cycles 1-4 on the Au cathode cycled in 1 M LiTFSI in DMSO (A) and 1 M $LiNO_3$ in DMSO (B). Cyclic Voltammetry was conducted from 2-4.1 V at 1 mV/s for LiTFSI in DMSO (A) and from 2-4.4 V for 1 M $LiNO_3$ in DMSO (B) at the same scan rate. The force was set to zero at the onset of each charge cycle for Figures A and B..... 74

Figure Page

A1. A) Representation of kSA MOS Components, B) Laser Beam Array, C, D) representation of the geometry associated with curvature measurements conducted on a flat and a curved substrate, respectively..... 101
A2. Cyclic Voltammetry of Au vs Li cycled in 1 M $LiClO_4$ in PC at 1 mV/s during 2nd cycle. A) Current density, B) Stress generation C) derivative of the stress-thickness product versus the potential. (Argon environment) 102
A3. Cyclic Voltammetry of Au vs Li cycled in 1 M $LiClO_4$ in PC at 1 mV/s during 4th cycle. A) Current density, B) Stress generation C) derivative of the stress-thickness product versus the potential. (Argon environment) 103
A4. Cyclic Voltammetry of Au vs Li cycled in 1 M $LiClO_4$ in PC at 1 mV/s during 5th cycle. A) Current density, B) Stress generation C) derivative of the stress-thickness product versus the potential. (Argon environment) 104
B1. Voltage and strain evolution in iron phosphate composite electrode during sodium intercalation in 1 M $NaClO_4$ in EC/DMC electrolyte at different scan rates during the 4th cycle. Dotted points indicate the predicted strains calculated from the mathematical model..... 109
B2. Na Concentration and Mismatch Strains in Electrode Particle: The sodium concentration profiles and the mismatch strains at five different scan rates. In the calculations, it is assumed that the electrode particles are discharged until 0.15, 0.27, 0.50, 0.62, 0.84 and 0.9% state of discharge for 2C, 1C, C/4, C/10, C/25 and C/100. The state of discharge values for each rate is chosen based on experimentally measured electrode capacity in Figure 5 112
B3. The lattice parameters for each direction of the unit cell, as well as the total change in the unit cell volume were calculated by using *in-situ* XRD during the sodiation of Na_xFePO_4 at C/66. The figure is re-generated from the previous publication [240] 116
B4. The change in the total unit cell volume during sodiation at C/66 is compared to the change in the unit cell volume change for each phase of Na_xFePO_4. This figure is regenerated from a previous publication[240]. 117
C1. Turning on and Setting Laser Power..... 121
C2. kSA MOS board layout..... 122
C3. Turning on the CCD Camera. 123
C4. X and Y Etalon adjustments. 124
C5. Focus Mode..... 124
C6. Mirror Calibration 125
C7. Mirror Calibration 125
C8. Curvature Mode Tab 127
C9. Curvature Mode Screen..... 128
D1. Images of the O-rings used for the current collectors (top), the cell (bottom), and the stainless steel plates (bottom)..... 132
D2. Images of current collector that will be used for the lithium foil (left) and for the cantilever (right)..... 133
D3. Image of the Au cantilever samples and the diamond tipped pen 133

Figure Page

D4. Image of the PTFE tape used to wrap the PTFE plugs or barbed adapters. 134
D5. Image of the PTFE barbed adapter with tubing 135
D6. Image of the assembled cell outside of the glovebox in lithium-ion battery configuration (due to the PTFE plugs) 135
D7. Image of assembled cell 137
D8. Image of the flowmeter inlet and outlet tubing 138
D9. Image of ultra-high purity oxygen tank with regulator 139
D10. Image of assembled cell on aluminum breadboard 141
D11. Image of fine adjustments knobs on tip/tilt and rotation stage 142
D12. Image of the z translator 142
D13. Image of the assembled cell on the optical table 143

CHAPTER I

INTRODUCTION TO LITHIUM-OXYGEN BATTERIES

1.1 Outline of Thesis

The thesis consists of four chapters, which are focused on analyzing the stress evolution on an Au cathode during the electrochemical cycling of an Li-O_2 battery. Chapter I consists of a motivation and a general overview of lithium-oxygen batteries, the problems associated with this technology, and possible mitigation techniques. Chapter II consists of general electrochemistry, an overview of common electrochemical techniques, and an overview of stress measurements. Chapter III is a draft of a submitted first-author paper regarding the stress evolution in lithium-oxygen batteries. Chapter IV is another draft of a first-author paper regarding the impact that lithium salts have on the stress evolution that results when cycling a lithium-oxygen battery. Appendix A is the supplemental information that accompanies the draft presented in Chapter III. Appendix B includes both a published journal article (published in the *Journal of Power Sources*) and its supplemental information. Appendix B only includes the modeling portion of a co-authored paper written alongside Bertan Ozdogru about the effects of strain on sodium iron phosphate electrodes. Appendix C consists of a Standard Operating Procedure of the kSA MOS system that was written to inform other students about how to use the kSA MOS system to monitor the stress evolution

that occurs during cycling. Appendix D consists of a Standard Operating Procedure of the assembly of the custom electrochemical cell that was written to inform other students about how to assemble the custom cell.

1.2 Motivation behind the Commercialization of Battery Technologies

As the global energy consumption continues to increase, the commercialization of new renewable technologies is becoming increasingly more important. The *International Energy Outlook* projects that renewable energy will supply approximately 49% of the world's net electricity generation by 2050 as shown in Figure 1[1]. The current reliance on fossil fuels is contributing to an increase in carbon dioxide emissions each year. Carbon dioxide emissions have increased by approximately 12 gigatons since 1990[2]. By expanding on the use of current battery technologies, the upward trend in the carbon dioxide emissions can be mitigated and slowly decrease.

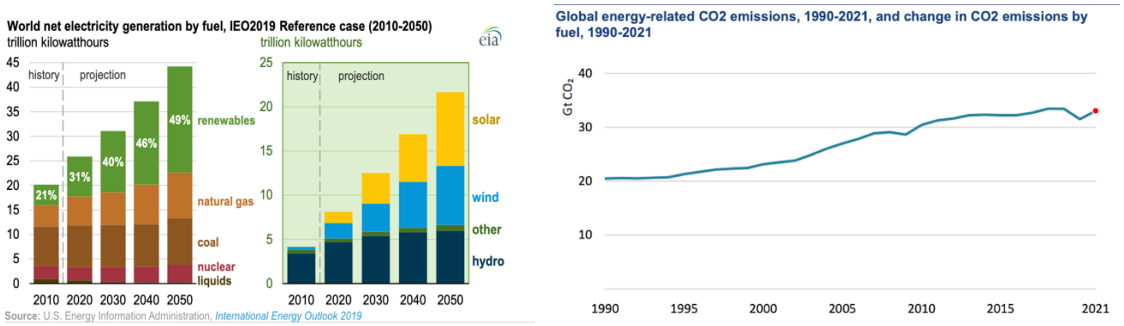

Figure 1[1]: Global net electricity generation (left) and carbon dioxide emissions (right)

Batteries can be used in a variety of sectors including transportation, energy storage, electricity generation, and portable electronics. The use of rechargeable batteries in the storage of electrical energy generated by solar and wind technologies could allow for a much more stable supply of electricity. The current supply of electrical energy from these technologies depends heavily on the climate and the generation is variable. By storing this energy more efficiently, the electrical energy generated would be more reliable and would be less susceptible to large price fluctuations that stem from the performance alone.

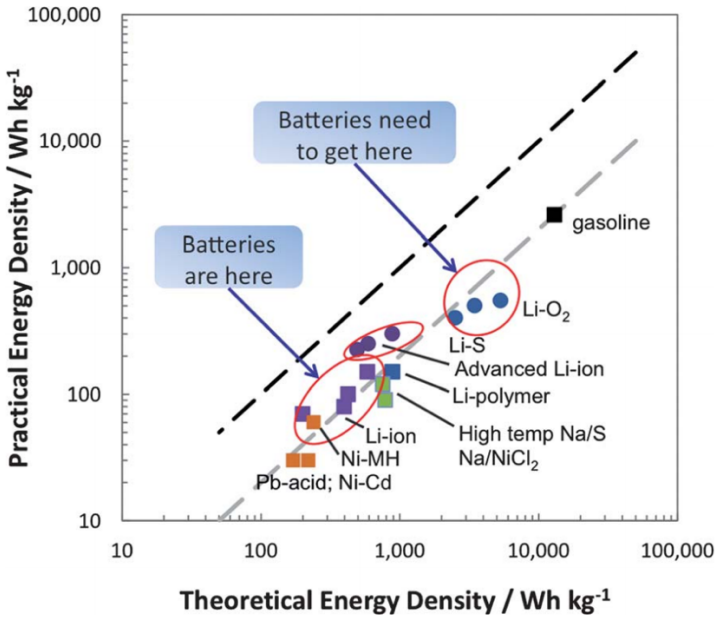

Figure 2[3]: Practical versus Theoretical Energy Density for various battery configurations

Figure 2 depicts the practical versus theoretical energy density for various battery configurations. As shown in Figure 2, the theoretical energy density for commercial lithium-ion batteries is approximately 300 Wh/kg, while the theoretical energy density for lithium-oxygen batteries is approximately 3500 Wh/kg[3]. Although the theoretical energy density for lithium-oxygen batteries is high, the practical energy density is much lower. Although research in this area is progressing, and the overall practical energy density is slowly improving, it still remains much lower than the theoretical energy density. This is the primary issue with lithium-oxygen batteries currently.

1.3 Introduction to Lithium-ion Batteries

Rechargeable lithium-ion batteries were first developed and patented by the SONY Corporation in 1985[4], and this battery consisted of a carbonaceous anode and a $LiCoO_2$ cathode. Since then, they have been widely commercialized and their usage has allowed for development of portable electronics. Lithium-ion batteries generally have a specific energy of around 100-175 Wh/kg, which is higher earlier battery configurations such as Nickel-Metal Hydride, as well as that of Nickel-Cadmium and Lead-Acid batteries which utilize toxic metals[5]. Lithium-ion batteries utilize the small ionic radius of lithium to increase the rate of diffusion across the electrolyte as well as well lower redox potentials to increase the overall specific energy density of the system[5].

1.4 Electrochemistry of Lithium-Ion Batteries

Lithium-ion batteries are electrochemical cells composed of a working electrode (cathode), a counter electrode (anode), and an electrolyte solution. In traditional electrochemical cells, the cathode is the electrode that becomes oxidized upon discharge, while the cathode becomes reduced[6]. The working electrode is the positive electrode, consisting of a host structure that lithium ions intercalate into during discharging.

The primary difference between lithium-ion and lithium-oxygen batteries is the type of mechanism that takes place. In lithium-ion batteries the electrodes are usually layered materials that host lithium ions during cycling. Typically, a metal oxide is used as the working electrode and graphite is used as the counter electrode[5–10]. During discharging, the lithium ions travel from the counter electrode to the working electrode. An oxidation reaction occurs at the counter electrode (typically graphite) and a reduction reaction occurs at the working electrode as the lithium ions are intercalated into the working electrode metal oxide host structure. The overall reaction is[7–12]:

$$\mathrm{Li_xC} + \mathrm{xe^-} + \mathrm{Li_{1-x}MO_2} \underset{\text{charging}}{\overset{\text{discharging}}{\rightleftharpoons}} \mathrm{LiMO_2} + \mathrm{C} \qquad (1)$$

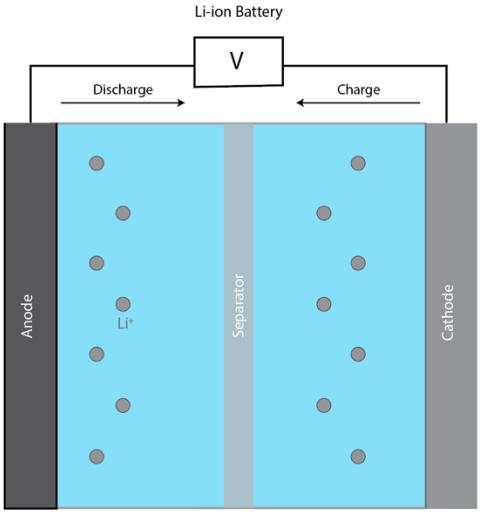

Figure 3: Schematic of a Lithium-ion Battery

1.5 Introduction to Lithium-Oxygen Batteries

Lithium-oxygen batteries will be discussed in detail. Lithium-oxygen batteries utilize a porous cathode that is exposed to oxygen as the working electrode and lithium metal as the counter electrode[13]. A porous carbon cathode is typically used due to its high active surface area and the ability of oxygen to readily diffuse through its pores. The availability of the working electrode, coupled with the high theoretical specific energy of Li-O_2 batteries, make them a promising technology. For comparison, the theoretical specific energy for commercial lithium-ion batteries is approximately 387 Wh/kg, while lithium-oxygen batteries boast a large capacity of 3505 Wh/kg[14]. Large specific capacities are needed in order to meet the energy storage requirements necessary to further eliminate the current dependence on fossil fuels.

Lithium-oxygen batteries are a relatively new battery technology. The first lithium-oxygen battery was developed by Abraham and Jiang[15] in 1996. Although this was novel, the means behind its discovery were serendipitous. Abraham et al. were investigating the electrochemistry of a polymer electrolyte that was being cycled in a lithium-graphite cell[16]. The gas evolution within the cell was being investigated using gas-phase infrared (IR) spectroscopy during discharging, but during this experiment oxygen was inadvertently introduced into the cell[16]. They noticed this when

the cell open circuit potential increased to around 3 V, and a potential plateau was seen at approximately 2.7 V. After this, Abraham and Jiang[15] developed the first Li-O_2 battery that contained a carbon cathode and a polymer electrolyte to prove that they could successfully cycle this battery at various current densities. After this, Abraham et al.[16–18] continued to investigate the electrochemistry behind lithium-oxygen batteries, focusing on the influence of both solvents and salts on the discharge products and reversibility. Read et al.[19–21] did early studies beginning in 2002 to investigate the role of the cathode.

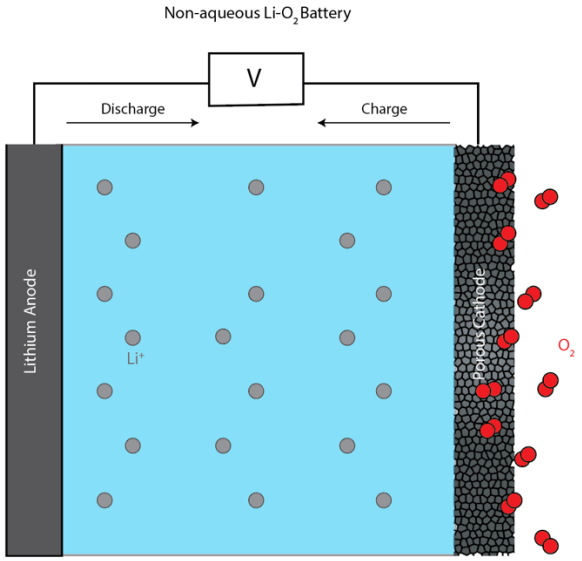

Figure 4: Schematic of a Nonaqueous Lithium-Oxygen Battery

1.5.1 Current issues existing in Lithium-Oxygen Batteries

Li-O_2 batteries suffer from several issues that occur during cycling such as electrolyte decomposition, parasitic reactants that result in products that occur during both discharging and charging, and the insulating nature of Li_2O_2. The primary bottleneck regarding the overall cycle life of Li-O_2 batteries is the cathode electrode. Although the chemistry relating to the low cycle life has been investigated, the mechanical deformations that could result during cycling have not yet been investigated.

The cycle life of the cell and its capacity are dependent on the stability of the cathode electrode. Parasitic reaction products can result due to the decomposition of carbon cathodes such as $Li_2{}^{13}CO_3$ and $^{13}CO_2$ evolution that result from the oxidation of the cathode during charging above 3.5 V[22] and lead to slow passivation of the electrode and an increased charging overpotential[49–52]. This will be discussed in more detail. The decomposition of the electrolyte is likely the second primary issue. Like the decomposition of the cathode, electrolyte decomposition also leads to parasitic reactants that ultimately lead to early cell death. The third primary issue is the slow reaction kinetics relating to the formation and decomposition of the main discharge product, Li_2O_2. These issues cause lithium-oxygen batteries to have a low capacity and a low cycle life as well due to the irreversibility occurring during cycling.

Figure 5[23] shows the low cycle life of lithium-oxygen batteries without the use of a redox mediator. This cell was cycled in 0.3 M $LiClO_4$ in DME using a carbon cathode. Two redox mediators were added to improve the performance[23]. In order to mitigate the decomposition occurring to the cathode during cycling, redox mediators are frequently used. They decrease the oxidation of carbon cathodes and reduce the overpotential occurring during charging[23–25]. This is highly irreversible as compared to commercial lithium-ion batteries that have a cycle life of over 1000 cycles[26]. Research on stabilizing the cathode electrode, the electrolyte, and improving the reaction kinetics are currently being assessed.

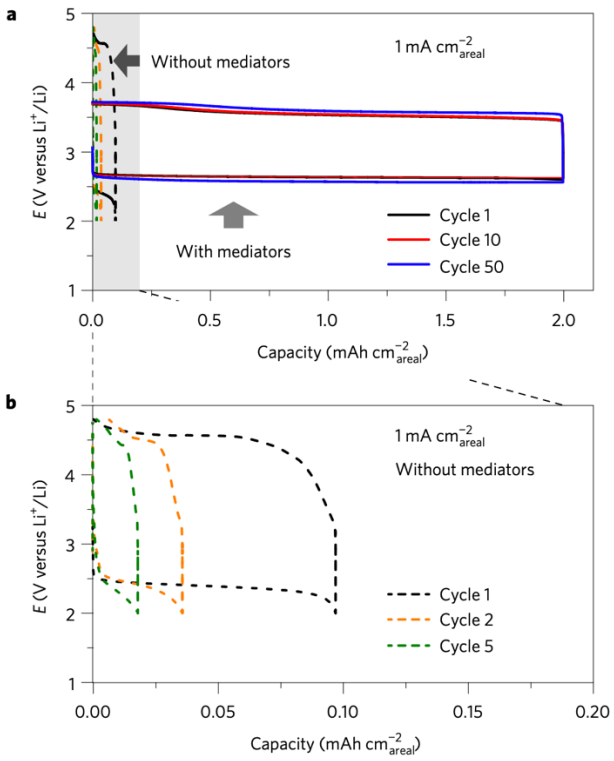

Figure 5[23]**:** The Capacity of Li-O_2 Batteries with and without redox mediators

1.5.2 Electrochemistry of Lithium-Oxygen Batteries

In lithium-oxygen batteries deposition and stripping takes place rather than intercalation. During discharging, the lithium ions travel from the counter electrode to the working electrode. An oxidation reaction occurs at the counter electrode (lithium metal) and sometimes a reduction reaction occurs at the working electrode (typically porous carbon)[13,15,16]. These lithium ions react with molecular oxygen to form lithium peroxide, Li_2O_2, which deposits onto the surface of the working electrode[15]. The formation mechanism for this lithium peroxide is not always formed electrochemically. During charging, lithium peroxide is oxidized back into lithium ions and molecular oxygen. These lithium ions travel back to the counter electrode. The overall reaction mechanism is[15]:

$$2Li^+ + 2e^- + O_2 \rightleftharpoons Li_2O_2 \qquad (2)$$

Abraham and Jiang[15] confirmed that the main discharge product was Li_2O_2 via Raman Spectroscopy; however, the mechanism behind the formation of Li_2O_2 continued to be investigated. In a later study, Abraham et al.[17] investigated this discharge mechanism further using cyclic voltammetry coupled with rotating disk electrode experiments and determined that a reaction intermediate, LiO_2, is formed first via the electrochemical reduction of molecular oxygen at a theoretical standard potential of 3.0 V[17,27].

$$Li^+ + O_2 + e^- \rightarrow LiO_2 \qquad E^\circ = 3.0\ V\ Li/Li^+, 2.65\ V\ O_2/O_2^- \quad (3)$$

It was also confirmed that the formation of Li_2O_2 could be formed two ways: chemically via a disproportionation of LiO_2 to Li_2O_2 (2), or electrochemically via a one-electron reduction of LiO_2 to Li_2O_2 occurring at a theoretical standard potential of 3.1 V[17,27]:

$$2LiO_2 \rightarrow Li_2O_2 + O_2 \quad (4)$$

$$LiO_2 + Li^+ + e^- \rightarrow Li_2O_2 \qquad E^\circ = 3.1\ V\ Li/Li^+,\ 3.27\ V\ O_2^-/Li_2O_2 \quad (5)$$

During charging, Li_2O_2 is oxidized back into lithium and molecular oxygen[17,28]:

$$Li_2O_2 \rightarrow O_2 + 2Li^+ + 2e^- \qquad E^\circ = 2.96\ V\ Li/Li^+ \quad (6)$$

Peng et al. conducted an in-situ Raman Spectroscopy study to confirm that the onset of Li_2O_2 formation occurs at 2.7 V[29]. They also confirmed that lithium superoxide is not a reaction intermediate during charging; instead, lithium peroxide is directly oxidized into lithium ions and molecular oxygen, and the oxidation of Li_2O_2 begins at 3.7 V and continues until the potential reaches approximately 4.4 V[29]. Due to the high overpotential during charging, as well as the sluggish reaction kinetics, the reversibility is currently very poor due to the high potentials needed to oxidize Li_2O_2. The overpotential needed to completely oxidize Li_2O_2 is approximately over 1 V[30].

Another possible discharge mechanism that could occur is a four-electron transfer that would completely reduce O_2 to lithium oxide (Li_2O) which is shown below in equations 7 and 8[16,31–33]. Although the reaction shown in equation 8 is desirable due to the high number of net electrons

that are transferred, the formation of lithium oxide via a four-electron transfer is not reversible nor is it kinetically favored during discharging[32]. The use of catalysts affects both the overpotential during charging and the emergence of discharge products as well[32]. Although lithium peroxide is the primary discharge product, the formation of lithium oxide via a two-electron reduction reaction, as shown in equation 7, is favored when using catalysts such as Pt, Pd, and catalyzed transition metal carbon-containing cathodes[16,32].

$$Li_2O_2 + 2e^- + 2Li^+ \rightarrow 2Li_2O \quad E^\circ = 2.72\ V\ Li/Li^+ \qquad (7)$$

$$O_2 + 4e^- + 4Li^+ \rightarrow 2Li_2O \quad E^\circ = 2.91\ V\ Li/Li^+ \qquad (8)$$

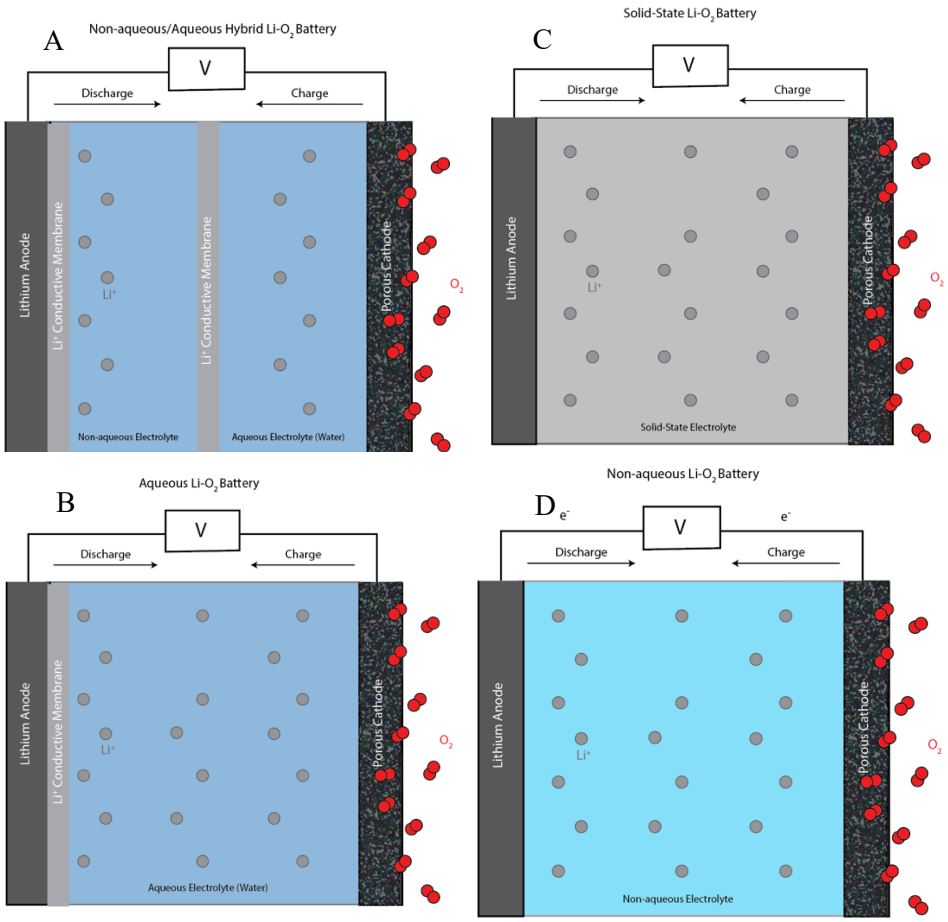

Figure 6: Schematic of Various Lithium-Oxygen Battery Systems

1.5.3 Overview of Various Lithium-Oxygen Batteries

Three other types of lithium-oxygen batteries exist that differ from the commonly studied nonaqueous electrolyte system; they are discussed below. There are four primary types of Li-O_2 cell configurations that have been studied[34]. The first is the most popular, nonaqueous Li-O_2 battery shown in Figure 6A. This was the first Li-O_2 battery that was developed and studied extensively[15,16,19,20]. Figure 6B represents an aqueous Li-O_2 battery, which was first developed by Visco et al. in 2004[35]. In aqueous Li-O_2 batteries, water serves as the electrolyte, while the primary discharge product is LiOH[34–36]. The primary electrochemical reaction occurring for aqueous Li-O_2 batteries in alkaline solutions is[14,34,36]:

$$4\mathrm{Li} + 2\mathrm{H_2O} + \mathrm{O_2} + 2e^- \rightleftharpoons 4\mathrm{LiOH} \quad (9)$$

The theoretical energy density for aqueous Li-O_2 electrolytes is 2,450 Wh/kg[36]. Although this is lower than the non-aqueous Li-O_2 system, it is still much higher than commercial Li-ion batteries and the primary discharge product, LiOH is soluble in an aqueous electrolyte[36]. This battery configuration consists of a lithium metal anode, a water-stable lithium electrode (WSLE) to protect the lithium metal from the aqueous electrolyte, and a porous cathode immersed in an aqueous electrolyte[34,36–38]. The issue that exists for this type of battery is the possibility of lithium metal coming into contact with the aqueous electrolyte, complexity and expense of constructing a water-stable lithium electrode (WSLE), and the possibility of the evaporation of water after a prolonged cycling period.

Figure 6C depicts a non-aqueous/aqueous hybrid Li-O_2 battery. It is a combination of both the aqueous and non-aqueous battery systems and houses a lithium metal anode immersed in a nonaqueous electrolyte, a solid-state electrolyte separating the nonaqueous and aqueous electrolyte, and a porous cathode immersed in an aqueous electrolyte[34,39,40]. The reaction mechanism for this hybrid battery is the same as the one for the Li-O_2 aqueous battery. The primary difference is the use of a nonaqueous electrolyte that is housed between the lithium metal anode and a solid-state

electrolyte. By using a non-aqueous electrolyte, the use of a water-stable lithium electrode is not needed[39,41]. Although the hybrid system has the advantage of using the non-aqueous electrolyte to protect the lithium anode, the solid-state electrolyte separating the two types of electrolytes is susceptible to damage due to the growth of dendrites occurring during charging and its instability in basic aqueous electrolytes[41].

The last type of Li-O_2 battery is the solid-state configuration depicted in Figure 6D. Solid-state lithium ion batteries have attracted a lot of attention due to the safety considerations associated with the use of liquid electrolytes, most of which are flammable[34]. The solid-state Li-O_2 battery is composed of a lithium metal anode, a solid-state electrolyte (lithium-ion conducting membrane), and a porous cathode[42,43]. The mechanism occurring during cycling in solid-state Li-O_2 batteries is the same as non-aqueous Li-O_2 batteries. The primary issues for solid-state electrolytes are the high cost and complex synthesis of the materials, possible damage due to the growth of dendrites occurring during charging, and high interfacial resistances that could limit the electrochemical performance.

1.5.4 Overview of Cathode Materials

An overview of cathode materials that are frequently used is given below. Since the introduction of the Li-O_2 battery, carbon has been used as the primary cathode material[15,19,20]. Typically, a carbon slurry consisting of carbon black particles and a binder dispersed in a solvent is cast on a metal mesh[44]. Carbon black materials that have been used in the past are Super P[45,46], KetjenBlack[45,46], and Vulcan XC72[47,48]. The primary bottleneck of the Li-O_2 battery is the cathode. Both the cycle life and the overall capacity are dependent on its stability.

Porous carbon materials are typically used due to their ability to facilitate oxygen diffusion throughout the cathode surface, their flexibility, high surface area, and high conductivity[30,49,50]. In low donor number solvents, Li_2O_2 thin films accumulate on the surface of the cathode, which can lead to pore blocking[44,51]. Although pore-blocking can occur, the primary reason for cell death is

the passivation of the cathode surface due to the insulating Li_2O_2 discharge product limiting the charge transport[44,52,53]. Although carbon is the most frequently used cathode material, it comes with stability issues relating to its decomposition at potentials of approximately 3.5 V[22].

Due to stability issues related with carbon, alternatives began to be sought to replace carbon cathodes. Materials such as Au[54–56], Pt[57,58], Pd[28], and metal oxides such as Co_3O_4[59,60], Mn_3O_4[39], and RuO_2[61,62] began to be used. Peng et al.[54] found that in the absence of a carbonaceous cathode resulted in a lack of CO_2 evolution and no electrolyte decomposition; however, carbon is still the primary cathode material due to its high porosity, which is needed to host Li_2O_2 deposits, high surface area and conductivity, as well as its low cost as mentioned previously. In order to mitigate the issues relating to carbon decomposition and instability during cycling, redox mediators were developed in order to decrease the oxidation of carbon cathodes and reduce the overpotential occurring during charging[23–25]. Redox mediators are also used to oxidize the larger toroidal shaped lithium peroxide molecules that are formed via the solution-based pathway. Oxidizing these larger particles is challenging and often results in large charging overpotentials. Redox mediators can be used during either discharging and charging to improve the reaction kinetics, but are frequently used during charging to improve the reversibility during cycling.

For example, during charging they can be added to the an electrolyte solution, they oxidize on the surface of the cathode at potentials around the onset of either the oxygen evolution reaction, and then effectively oxidize the lithium peroxide particles as well[13]. This improves the reversibility during cycling and decreases the charging overpotentials by reducing the potential at which Li_2O_2 oxidation takes place below 3.6 V, which aides in the stability of the carbon cathode[13,23,63]. Although some Li_2CO_3 was still generated from the decomposition of the carbon cathode after the use of a redox mediator, most of it was formed during electrolyte decomposition, and much less of it was generated compared to standard cells that used carbon without a mediator[23]. Redox mediators

are continuing to be studied in order to further reduce the decomposition of the carbon cathode and reduce the charging overpotentials[25,30,63–65].

1.5.5 Overview of Parasitic Reaction Species

One bottleneck inhibiting the commercialization of lithium-oxygen batteries are the instabilities relating to both carbon cathodes and non-aqueous electrolytes. This demonstrates the issues relating to cathode chemistry in lithium-oxygen batteries. It is well known that the use carbonate solvents results in electrolyte decomposition during discharge resulting in the biproducts lithium acetate (CH_3CO_2Li), lithium formate (HCO_2Li), lithium alkyl-carbonate ($LiRCO_3$), lithium propyl dicarbonate [$C_3H_6(CO_2Li)_2$], as well as lithium carbonate, Li_2CO_3, being the primary reaction discharge products rather than Li_2O_2 [54,66–70]. After this discovery, research into other aprotic solvents such as ethers and sulfoxides began. Gallant et al. found that Li_2CO_3 formed between the carbon cathode-Li_2O_2 interface in DME during discharge, and its accumulation lead to the passivation of the cathode surface as well as capacity fading[71].

Thotiyl et al. studied the parasitic byproducts while cycling a carbon cathode in two commonly used electrolytes, DMSO and tetraglyme[22]. Although the carbon was relatively stable at potentials lower than 3.5 V, the carbon cathode promotes electrolyte decomposition, which causes both lithium carbonate, $Li_2{}^{12}CO_3$, and lithium carboxylates, $LiRCO_3$, to be formed during discharging to 2 V and during charging up to 4.5 V[22,72]. This $Li_2{}^{12}CO_3$ formed during discharge also oxidizes at potentials around 3.5 V and begins to form again as the electrolyte begins to decompose[22]. The carbon cathode itself begins to decompose around 3.5 V to form $Li_2{}^{13}CO_3$ [22]. Carbon dioxide evolution (both $^{13}CO_2$ and $^{12}CO_2$) occurs due to the decomposition of $Li_2{}^{12}CO_3$, $Li_2{}^{13}CO_3$, and lithium carboxylates[22,72]. This lithium carbonate produced during cycling causes both passivation of the cathode, an increase in the charging overpotential, and a decrease in the capacity[22,71,72]. A representation of the instabilities of carbon cathodes and the potential ranges is shown in Figure 7[22].

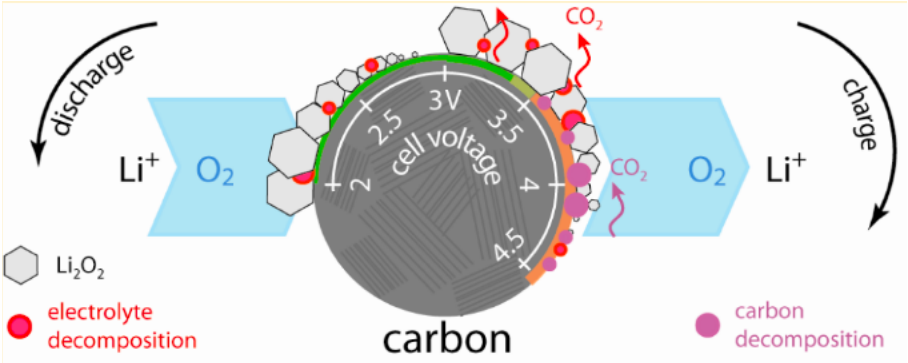

Figure 7[22]: Representation of the stability issues of carbon cathodes during cycling

Another main issue is the stability of the electrolyte solution. In Li-O_2 batteries, many oxygen radicals are generated during cycling that can react with organic substrates[13]. This class of oxygen species are known as reactive reduced oxygen species (RROS) which include O_2^-, O_2^{-2}, HO^*, HOO^*, and HOO^- [13,30,73]. The strong nucleophilic properties of superoxide, O_2^-, has led to its proposal as the primary culprit behind the decomposition of the carbonate solvents used for Li-O_2 batteries[24,72,74,75]. Although RROS react readily in carbonate solvents[70,76], the same is not true for other aprotic electrolytes. Ether solvents, for example, were found to be stable against a possible nucleophilic attack by the superoxide anion, unlike carbonates, sulfonates, and phosphate containing solvents; however they are oxidized in the presence of O_2[73,77,78]. Research regarding the sources of electrolyte decomposition is still ongoing.

Another major source of electrolyte decomposition is singlet oxygen, $^1O_2$. Wandt et al. discovered the presence of singlet oxygen during the first charge cycle at approximately 3.5 V, and linked it to many side reactions that occur while charging[79]. Although singlet oxygen was only observed during charging, beginning at approximately 3.5 V[79], Mahne et al.[80] proved that singlet oxygen could also be generated during discharging and during charging at potentials below 3.5 V. This complicates issues regarding the electrolyte stability and cycle life of the cell, since there does not appear to be a potential window that exists to avoid these stability issues.

1.5.6 Lithium Peroxide Formation Mechanism during Discharging in Nonaqueous Solvents

The main issues with lithium-oxygen batteries are the cathode instabilities and the reversibility of lithium peroxide decomposition and formation (described in sections 1.5.6 and 1.5.7). Research has been focused on how lithium peroxide forms and its varying morphology. The goal of the curvature measurements that are discussed in Chapter III is to understand the impact of the lithium peroxide deposition and stripping on the Au thin film cathode and how reversible this stress evolution is.

Lithium peroxide is an electronically insulating discharge product that exists as a solid since it is insoluble in nonaqueous aprotic solvents[52,81–83].This insulating discharge product can ultimately lead to passivation of the cathode, resulting in premature cell death. This also explains the sluggish charge kinetics and low reversibility due to the lack of charge transport that can occur through the film[81]. Lithium peroxide can form either by electrochemical reduction of lithium superoxide, LiO_2 or via disproportionation as mentioned previously. Disproportionation reactions are spontaneous redox reactions occurring when a compound with an unstable intermediate oxidation state yields two products, one with a higher and one with a lower oxidation state[84]. The discharge mechanism dictates the morphology of the Li_2O_2 product, and affects the overall cell performance[85–88]. These studies confirmed the existence of two distinct morphologies of Li_2O_2: thin-films[88] and toroidal shaped particles[85–87]. Although the results of these studies were promising, they did not understand why they were obtaining these differences in the morphology.

To elucidate the reason behind these different lithium peroxide morphologies, Johnson et al.[51] proved that the lithium superoxide reaction intermediate formed during discharging controls the discharge reaction mechanism. He confirmed this by using a series of different nonaqueous solvents with different donor numbers and cycling them at various rates[51]. When high donor number solvents are used, the lithium superoxide is dissolved in the electrolyte solution; however, when low donor number solvents are used, lithium superoxide is adsorbed onto the electrode

surface[51]. Irrespective of the donor number, molecular oxygen is reduced to form both LiO_2^* adsorbed on the surface of the cathode electrode and LiO_2 dissolves in the electrolyte solution according to the reaction in equation 10[51]:

$$LiO_2{}^* \rightleftharpoons Li^+{}_{sol} + O_2{}^-{}_{sol} + \text{ion pairs} + \text{aggregates} \qquad (10)$$

Equation 10 demonstrates the equilibrium between the LiO_2 that has been dissolved in the aprotic electrolyte (right of equilibrium) and adsorbed onto the electrode surface (left of equilibrium). The ion pairs and higher aggregates are other species that exist in the electrolyte solution[51]. In low donor number solvents, the Gibbs free energy is lower for the LiO_2^* adsorbed onto the left surface, which shifts the reaction equilibrium to the left, while for high donor number solvents, the opposite effect is observed, the Gibbs free energy is lower for the LiO_2 that is dissolved in the electrolyte solution, which shifts the reaction to the right[51,68,82].

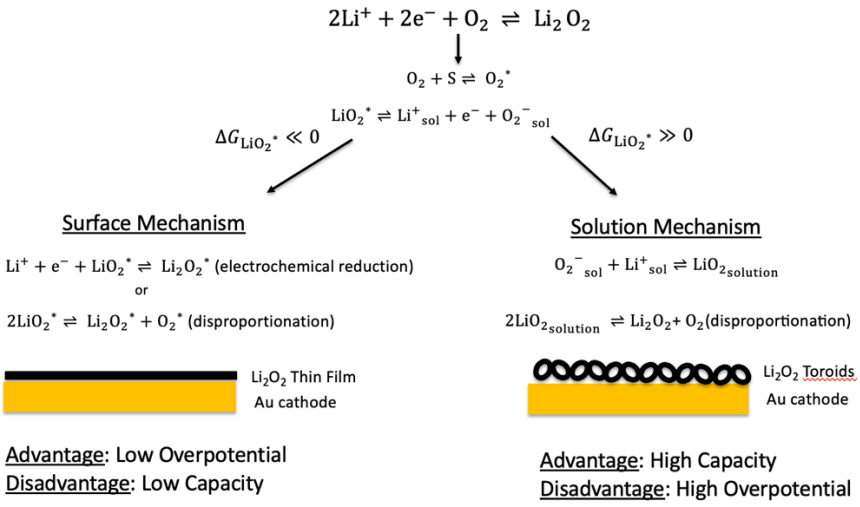

Figure 8: Representation of Li_2O_2 Formation Pathways

The differences in the mechanisms dictate the morphology of the Li_2O_2 product that forms. Johnson et al. proved that in low donor number solvents, a Li_2O_2 thin film was deposited onto the surface of the cathode, which was a consequence of the LiO_2^* that was adsorbed[51]. This insulating film lead to cell death, likely due to the loss of conductivity, once the thickness of the film reached approximately 7 nm[51]. In high donor number solvents, the morphology of the Li_2O_2 was toroidal

and the maximum thickness of the Li_2O_2 was much higher due to most of the Li_2O_2 growth occurring in the electrolyte, which resulted in much higher capacities[51].

Although the solvent donor number has been proven to affect the morphology of the Li_2O_2 that forms, it is also influenced by the cycling rate[89–93], water content[82,94,95], and ionic association strength of the lithium salt[56,96]. The impact of the lithium peroxide morphology associated with changes in the water content, solvent donor number, and the ionic association strength of the lithium salt is shown in Figure 9[13].

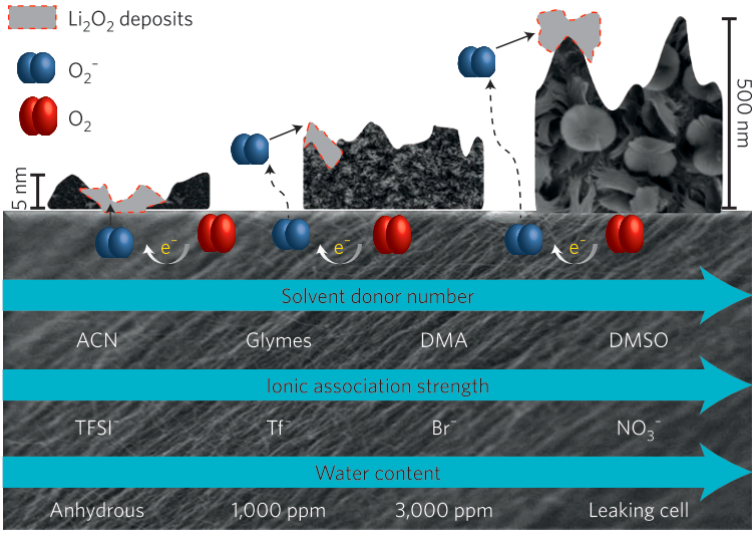

Figure 9[13]: Representation of the variables affecting the Li_2O_2 morphology during discharge

Adams et al. used SEM to confirm that a Li_2O_2 solution-based mechanism producing Li_2O_2 toroids occurred at lower current densities (shown in Figure 10A), while a Li_2O_2 surface-based mechanism producing Li_2O_2 thin films occurred at higher current densities[89] (shown in Figure 10B).

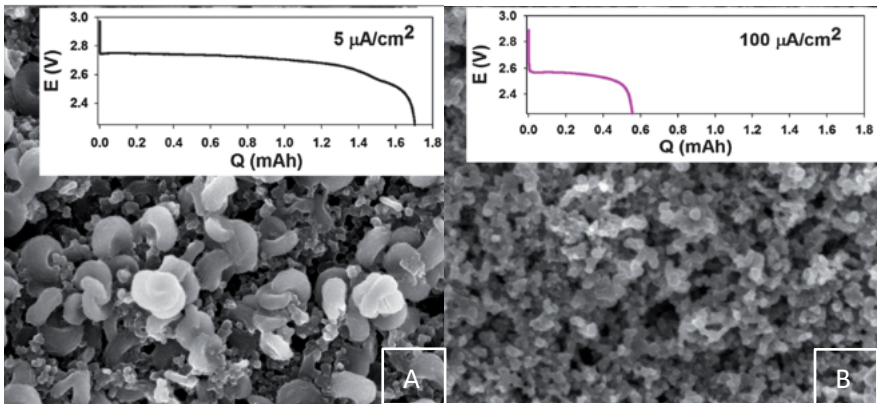

Figure 10[89]**:** Morphology of Li_2O_2 at low current density (A) and high current density (B)

They explain this by considering the rates of electron transfer. When the electron transfer rate is low, LiO_2 is dissolved in the electrolyte solution via disproportionation[89]. This most likely results due to the lack of kinetic limitations that exists for disproportionation since it is a chemical reaction rather than an electron transfer reaction[17,97]. At higher current densities, a higher electron transfer rate is observed which results in LiO_2 being adsorbed onto the working electrode surface. This higher electron transfer rate favors Li_2O_2 formation via the electrochemical reduction of LiO_2[31,89].

The water content inside the cell also affected the morphology and capacities of Li_2O_2. As the water content of either the electrolyte[95] or the with the introduction of water-saturated O_2 gas[94], a higher water content favored higher discharge capacities due to a higher amount of Li_2O_2 formation, along with toroidal-shaped Li_2O_2. Although one would expect lower electrochemical performance, the introduction of water proved to be effective in obtaining the toroidal-shaped Li_2O_2 deposits, that help prevent the surface passivation of the working electrode surface (that results from Li_2O_2 thin films).

Finally, the ionic association strength of the lithium salt also played a role in the Li_2O_2 morphology[30,56,96]. Lithium salts with high ionic association strengths such as LiBr and $LiNO_3$ favored semicircle and toroidal-shaped Li_2O_2 deposits in diglyme (a low donor number solvent), respectively[56]. The high ionic association strength of the salt causes the lithium ions to become

more coordinated with the anion, forming complexes that are strongly solvated and decreases the Lewis acidity of the lithium cation[56]. This promotes LiO_2 formation in solution, which disproportionates to form Li_2O_2 due to its low stability[30,56].

1.5.7 Proposed Mechanisms for the Decomposition of Lithium Peroxide

The decomposition of lithium peroxide has remained a mystery for years, even once the discharge mechanisms had been discovered. As mentioned previously, during charging, lithium peroxide is oxidized back into lithium and oxygen. This reaction is referred to as the oxygen evolution reaction (OER). The mechanism of Li_2O_2 during charging remained was not experimentally determined until 2011 by Peng et al.[29] who proved that LiO_2 was not an intermediate during charge as it is in discharge. The following two-electron mechanism was proposed[29,98]:

$$Li_2O_2 \rightarrow O_2 + 2Li^+ + 2e^- \quad (11)$$

After this, Ganapathy et al.[99] proved experimentally that a lithium deficient solid-solution reaction occurs which first decomposes amorphous Li_2O_2 at lower potentials, and crystalline Li_2O_2 at higher potentials via X-ray diffraction (XRD). The mechanism occurring during charging was investigated in more detail by Wang et al.[75] to reveal that this mechanism was dependent on the solvent donor number, much like the discharge mechanism. In low donor number solvents, no LiO_2 was observed, and a solid-solution mechanism was revealed that was in agreement with past experimental and modeling studies[75,99,100]:

$$Li_2O_2 \rightarrow Li_{2-x}O_2 + xLi^+ + xe^- \quad (12)$$

$$Li_{2-x}O_2 \rightarrow O_2 + (2-x)Li^+ + (2-x)e^- \quad (13)$$

The first step, (equation 12), represents the formation of a lithium deficient phase via the decomposition of amorphous Li_2O_2[75,99]. As the amount of lithium, x, reaches a critical value, this lithium deficient phase becomes unstable, and oxidizes as represented by (equation 13)[75,99]. This reaction was observed to take place at lower potentials, while the second step was determined to

take place at higher potentials[75,99]. The potential that the second mechanism begins is dependent on the solvent donor number.

In solvents with high donor numbers, two primary oxidative steps occur. The first step is similar to (equation 11), but the main difference in the mechanism between the low and high donor number solvent is the existence of soluble LiO_2 in high donor number solvents[75]:

$$Li_2O_2 \rightarrow Li_{2-x}O_2 + xLi^+ + xe^- \quad (14)$$

$$Li_{2-x}O_2 \rightarrow LiO_{2(sol)} + (1-x)Li^+ + (1-x)e^- \quad (15)$$

$$2LiO_{2(sol)} \rightarrow Li_2O_2 + O_2 \quad (16)$$

The second step (equation 15) was also observed experimentally in a solid-state Li-O_2 battery via transmission electron microscopy (TEM). As mentioned previously, LiO_2 formation could cause additional side reactions due to its strong nucleophilic properties[72,74,75,101]. The third step (equation 16) shows the disproportionation of soluble LiO_2 into Li_2O_2. This causes the potential to slowly rise in order to oxidize this newly formed Li_2O_2[75]. These charging mechanisms were determined by Wang et al.[75] via X-ray absorption (XANES) and potentiostatic intermittent titration techniques (PITT)[75]. This study elucidated how the charging mechanisms were dependent on the solvent donor number much like the discharging mechanisms.

1.5.8 Overview of Nonaqueous Solvents used in Lithium-Oxygen Batteries

The following section highlights the issues relating to some of those solvents, and why the solvent choice is important. When nonaqueous lithium-oxygen batteries were first being investigated, carbonate electrolyte solvents typically used in lithium-ion batteries were used such as propylene carbonate (PC)[19,20,102–104], dimethyl carbonate (DMC)[19,20,102], diethylene carbonate (DEC)[19,20,102], and ethylene carbonate (EC)[19,20,102]. When these electrolyte solvents were used, the performance of lithium-oxygen batteries remained low. To investigate this, Mizuno et al.[66] proved that the primary discharge products were lithium alkyl-carbonate, $LiRCO_3$, and lithium carbonate, Li_2CO_3, while the amount of Li_2O_2 generated remained low[67]. Abraham et al. began to investigate nonaqueous

solvents that were different than those typically used for lithium-ion batteries, with a focus on the Gutmann donor number[18].

The Gutmann donor number, described in section 1.5.6, measures the ability of a solvent to act as a nucleophile, or Lewis base, to effectively solvate Lewis acids and cations, such as lithium ions. Formally, it is the negative enthalpy term for the formation of an adduct between a solvent and antimony pentachloride in a dilute solution of a solvent with 1,2 dichloroethane, which has approximately a zero donor number[105]. Typical high donor number solvents used for lithium oxygen batteries include dimethylformamide (DMF)[106,107], dimethylacetamide (DMA)[107–109], dimethyl sulfoxide (DMSO)[51,54,55,110] and tetraethylene glycol dimethyl ether (TEGDME)[89,111], while low donor number solvents include acetonitrile[17,51], and glyme solvents such as dimethoxyethane (DME)[51,71,82,95,111] and bis(2-methoxyethyl) ether (diglyme)[56,96,111,112].

Table 1: Donor Numbers of Commonly Used Li-O_2 Nonaqueous Solvents

Solvent	Donor Number (kcal/mol)
Acetonitrile (AN)[31,83,105,113]	14.1
Propylene carbonate (PC)[31,83]	15.1
Ethylene carbonate (EC)[105]	16.4
Dimethoxyethane (DME)[31,83,105,113]	20.0
Dimethylsulphoxide (DMSO)[31,83,105,113]	29.8
Tetraethylene glycol dimethyl ether (TEGDME or tetraglyme)[31,83]	16.6
bis(2-methoxyethyl) ether[114] (diglyme)	18
DMF[31,83]	26.6
DMA[31,83,113]	27.8

By analyzing the donor number, one can understand how the solvent will function as a Lewis base to effectively solvate the lithium cations by forming a Li-solvent complex[18,75,115–117]. These complexes that form in high donor number solvents such as DMSO stabilized the superoxide ion, O_2^-, longer in the electrolyte solution while in low donor number solvents, the superoxide ion decomposed quickly[18]. The electrochemical performance, as well as the morphology changes that resulted due to the effect of the solvent donor number was detailed in later studies.

1.5.9 Overview of Lithium Salts used in Lithium-Oxygen Batteries

Although the choice of lithium salt has been proven to affect the discharge reaction pathway during discharging, few studies have analyzed the impact that the choice of lithium salt has on both the morphology of the Li_2O_2 and the overall capacity. In the early stages of Li-O_2 battery development, both the electrolyte salts and solvents used were very similar to ones used in commercial lithium-ion batteries[19,20]. As the donor number began to be investigated, the effects of the choice of lithium salt also began to be investigated. Although lithium-oxygen batteries are much more reversible with higher capacities in high donor number solvents, these solvents are not stable with lithium metal anodes[110]. By tuning the ionic association strength of the lithium salt, the morphology of the Li_2O_2 can be controlled in low donor number solvents[56,96]. Low donor number solvents such as glymes are less reactive with the lithium metal anode, and could improve the cycling performance if the Li_2O_2 morphology could be tuned[118,119].

1.6 Proposed Study

Previous literature studies have demonstrated the impact of cycling conditions, the electrolyte, and the use of cathode catalysts on electrochemical performance and the lithium peroxide decomposition and oxidation pathways that result. The lack of understanding of the mechanical implications resulting from the formation and the decomposition mechanisms of the lithium peroxide product during discharge has been studied minimally. The goal of the research plan is to elucidate the complex surface reactions taking place on the cathode electrode during the oxygen evolution and reduction reactions. This is driven by the hypothesis that the competing surface phenomena on the cathode can be identified by probing the interfacial mechanical deformations taking place on a nano-scale level during electrochemical cycling. This hypothesis will be verified by conducting a series of in situ mechanical measurements while cycling lithium-oxygen batteries in different electrolytes. To achieve this, a novel experimental setup has been developed that will monitor the in situ stress evolution that takes place during electrochemical cycling. The generation of surface stress can be associated with ion adsorption, film formation, and both the nucleation and

decomposition of reaction products on the cathode surface. The impact that the electrolyte salt has on the surface reaction dynamics will also be analyzed during both discharging and charging. The outcome of this project will generate newfound knowledge of the reaction processes occurring on lithium-oxygen battery cathodes and will provide a new perspective on the competing faradaic (electrochemical oxidation and reduction) along with non-faradaic (adsorption and dissolution) surface processes.

CHAPTER II

INTRODUCTION TO ELECTROCHEMICAL SYSTEMS AND STRESS

2.1 Introduction to Electrochemical Systems

A traditional electrochemical cell houses two electrodes and an electrolyte solution. The two electrodes are referred to as the anode (negative electrode), and the cathode (positive electrode). An external conductor is used to connect the two electrodes to allow electrons to move from one electrode to the other. At the anode electrode, ions are oxidized (lose electrons). At the cathode electrode, ions are reduced (gain electrons). Since two reactions are taking place (one at the anode and one at the cathode) each are typically written as half-cell reactions[6]. An electrolyte is the medium between the two electrodes that can either be a liquid or a solid. The electrolyte is electronically insulating and serves as a medium to diffuse charged ions to carry current from one electrode to the other[6]. When a current is applied to the external conductor, the charged ions diffuse through the electrolyte and a heterogeneous reaction takes place on the electrode surface[6]. This reaction is heterogeneous because it occurs on the surface of the electrode[6].

The anode electrode causes the charged ions to become oxidized (lose electrons) on the electrode surface, while the cathode electrode causes the charged ions to become reduced (gain electrons) on the electrode surface. When cycling a traditional lithium-ion battery, during discharge, the electrons travel from the counter electrode to the working electrode. An oxidation reaction takes place at the counter electrode and lithium ions travel to the working electrode and are. During charging, the

reverse reaction takes place. The electrons travel from the working to the counter electrode. An oxidation reaction occurs at the working electrode and lithium ions travel back to the counter electrode and are reduced.

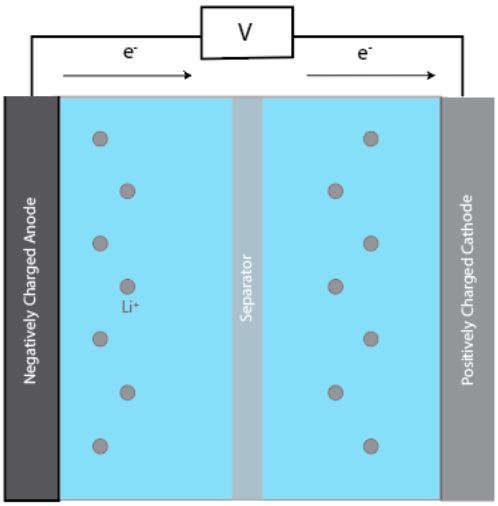

Figure 11: Representation of a Rechargeable Battery

In rechargeable batteries, electrons flow from the anode to the cathode. This can be confusing terminology, however, because the electrons are being passed from one electrode to the other which changes the sign convention of the electrodes. To prevent confusion, the terms working and counter electrode are assigned. The counter electrode begins as the negative electrode (such as lithium foil), while the working electrode begins as the positive electrode (metal oxide or porous carbon). During discharge, metal ions are oxidized at the counter electrode and are reduced on the working electrode surface. During charging, metal ions are oxidized at the working electrode and travel back to the counter electrode.

The flow of current is opposite to the direction of electron flow in order to balance the net charge. This means, that when discharging a rechargeable battery, the electrons would flow from the counter electrode to the working electrode, while the current would flow from the working electrode to the counter electrode[6]. As far as the sign convention of the current is concerned, when the cell is discharged (electrons move from the counter to working electrode) the sign of the current

is negative. When the cell is charged, the sign of the current is positive. When no current is being supplied to the cell, there are no reactions happening at either electrode and the cell is at open circuit.

2.2 Introduction to Terminology

A plethora of electrochemical systems exist, and the performance of each can be analyzed in many ways. One way to characterize an electrochemical system is to measure its current density. The current density is the amount of current that is being applied to the cell divided by the active area of the electrode (A/m^2).

$$\text{Current Density} = \frac{I}{A} \tag{17}$$

This term will frequently be used to describe electrochemical experiments that will be discussed in later chapters. Since the current density has both a specific sign and magnitude, it is a vector. The direction of the flow describes the movement of ions. Another way to characterize the electrochemical performance of a cell is to calculate its capacity. The capacity of the cell is a measure of its ability to store charge. The equation for the theoretical capacity is given in equation 17 below[6]:

$$\text{Theoretical Capacity} = \frac{mnF}{M} \tag{18}$$

In equation 18, m represents the mass of the electrode's active material (g) while M is the molecular weight (g/mol). F is the Faraday's constant (96485 Coulombs/mol), and n is the number of electrons transferred during the electrochemical reaction[6].

Electrochemical measurements can aid in the understanding of both the cell performance and the reactions happening within the cell. The two most common parameters that can be used to analyze the cell's performance are the potential and the current[120]. Although they cannot both be independent variables due to their dependence on each other, one can be controlled while analyzing the behavior of the other.

The cell potential controls the species (free ions) within the electrolyte. In an electrochemical cell, the oxidation-reduction reactions depend on the cell's potential. By monitoring the potential, the state of the reaction can be determined. For example, if the electrochemical reduction of molecular oxygen occurs at a theoretical standard potential of 3.0 V, then LiO_2 is formed at a potential of 3.0 V versus a Li/Li^+ reference electrode. This is the potential at which this reaction proceeds.

$$Li^+ + O_2 + e^- \rightarrow LiO_2 \qquad E^\circ = 3.0\ V\ Li/Li^+ \qquad (19)$$

2.3 Introduction to Electrochemical Analysis Techniques

2.3.1 Cyclic Voltammetry

During cyclic voltammetry, the potential of the working electrode is controlled for the duration of the experiment. The potential of the working electrode is linearly scanned in two directions at a specific rate measured in V/s. First, the cell is scanned in the negative direction, which discharges the cell. During the cathodic scan in a two-electrode electrochemical cell, the ions from the counter electrode are oxidized (lose electrons) and travel to the working electrode where they are reduced (gains electrons). After the scan in the cathodic scan is complete, the cell is scanned in the opposite direction (positive) at the same rate. This scan is referred to as the anodic scan and it charges the battery. The ions are oxidized at the working electrode and travel back to the counter electrode where they are reduced again. One complete cycle in cyclic voltammetry consists of one cathodic and one anodic scan. The ions would be oxidized at the working electrode and would travel to the counter electrode where they would be reduced again. The diffusion of the species in the electrolyte controls the current response in the cell. Common reasons to use cyclic voltammetry include the analysis of overpotential, the degree of reversibility of the electrochemical reaction, determination of the diffusion coefficient of the species in the electrolyte, and to analyze the interfacial phenomena occurring in the cell[121].

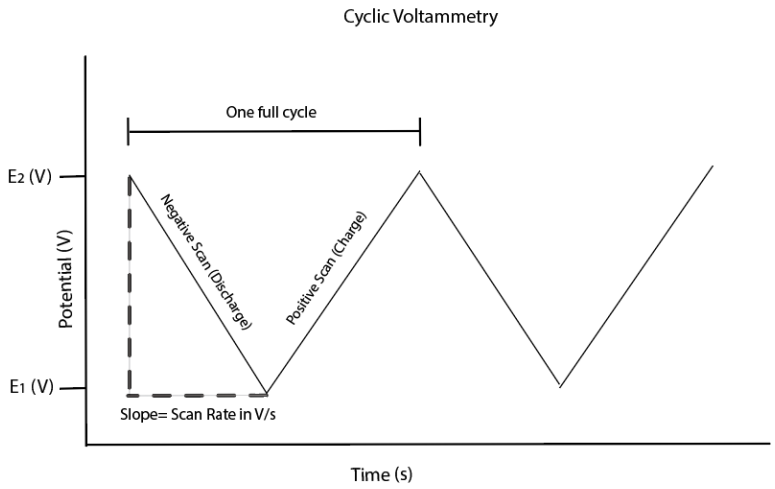

Figure 12: Schematic of the potential versus time in a cyclic voltammogram

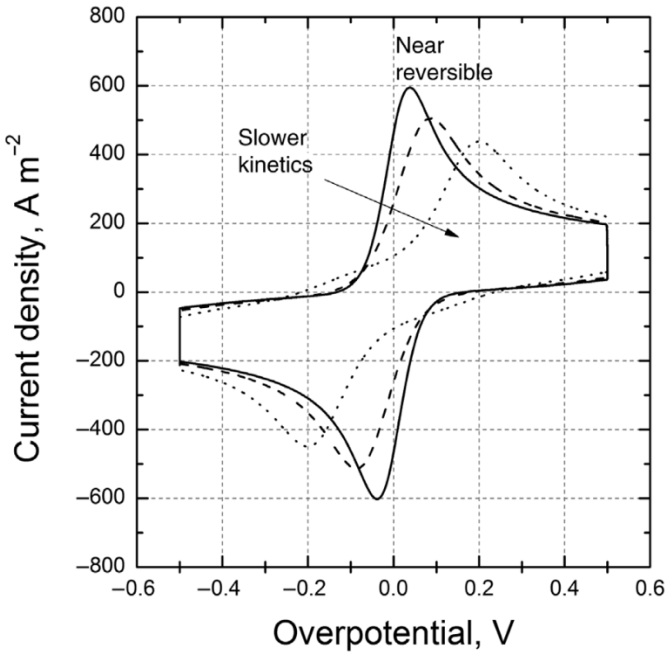

Figure 13[6]: Current density versus potential for a cyclic voltammogram

Figure 13[6] is a plot of a cyclic voltammogram. The current density is plotted against the potential. Three cyclic voltammograms are shown with slightly different shapes. The peak current is the highest current density that is obtained during each scan. This peak represents either a reduction reaction (cathodic scan) or an oxidation reaction (anodic scan) that takes place during cycling. The

higher the peak current, the faster the reaction kinetics are[6]. The scan rate also influences the peak current. The faster the scan rate, the higher the peak current in both the cathodic and anodic scan[6]. Figure 13[6] also shows that the potentials at each peak become farther from one another. In a reversible system, the cycles in a cyclic voltammogram have a peak occurring at the same potentials. As the reaction becomes less reversible, the potentials at each peak move farther apart, and in an irreversible system only one peak exists. Cyclic voltammograms are commonly used to characterize new systems in order to analyze the reaction kinetics, reversibility of the system, and the potentials at which the current increases.

2.3.2 Linear Sweep Voltammetry

Linear sweep voltammetry (LSV) is very similar to cyclic voltammetry. During cyclic voltammetry, the potential of the working electrode is linearly scanned in two directions, but in linear sweep voltammetry the potential is only scanned in one direction. The cell can be swept in the negative direction (cathodic scan) or in the positive direction (anodic scan) as shown in Figure 13.

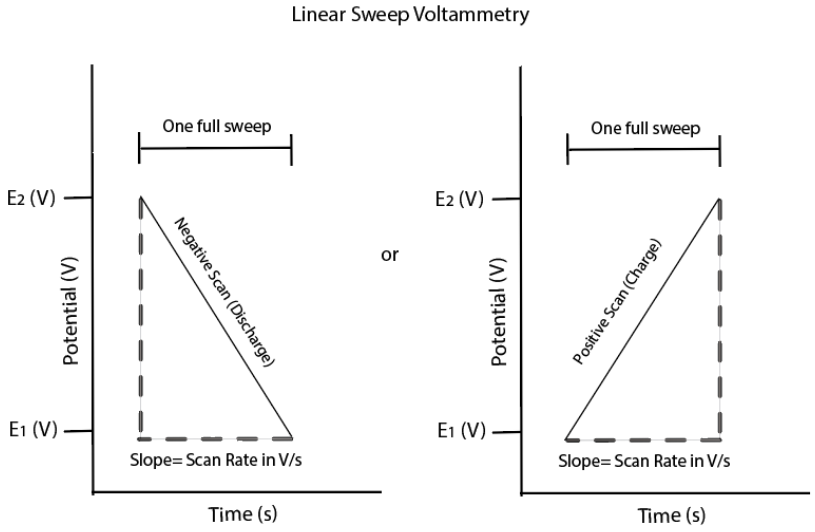

Figure 14: Schematic of the potential versus time during linear sweep voltammetry

2.3.3 Galvanostatic Cycling

During galvanostatic cycling, the current is kept constant and the potential is monitored. The current that is applied can be arbitrary or it can be applied in terms of an electrode's mass or area. During discharge, the applied current is negative and the active ions are oxidized at the counter electrode and are reduced at the working electrode. During charge, the applied current is positive and the active ions are oxidized at the working electrode and are reduced at the counter electrode. One galvanostatic cycle consists of one discharge cycle and one charge cycle.

Galvanostatic plots show how the potential in the cell changes over time. The potential will plateau when either an oxidation or a reduction reaction takes place. For example, when discharging a Li-O_2 battery, lithium ions are oxidized at the counter electrode (lithium foil) and travel through the electrolyte to the working electrode. The potential plateau occurring during discharge represents the formation of the discharge product, Li_2O_2, that deposits on the surface of the working electrode. The potential plateau occurring during charge represents the oxidation of this discharge product, Li_2O_2, at the working electrode and the migration of the oxidized lithium ions back to the counter electrode (lithium foil) where the lithium ions are reduced again. A galvanostatic cycling plot is shown in Figure 15.

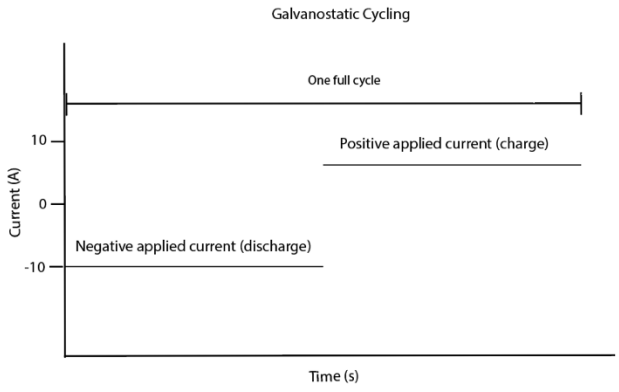

Figure 15: Schematic of the current evolution over time during galvanostatic cycling

The galvanostatic plot is also plotted with respect to the cell's capacity. The capacity of the cell is a measure of its ability to store charge as described previously. The specific capacity can also be easily determined by using galvanostatic cycling. The capacity can be measured in terms of the active electrode area or the mass of the electrode. The equation for the areal capacity is shown in equation 20:

$$\text{Areal Capacity } \left(\frac{\text{Ah}}{\text{m}^2}\right): \frac{\text{It}_{\text{cycle}}}{\text{A}} \tag{20}$$

Typically, these capacities are separated for charging and discharging reactions. t_{cycle} is the duration of either the discharge or the charge cycle (hours), I is the current being applied to the cell (A), and A is the active area of the working electrode surface (m^2).

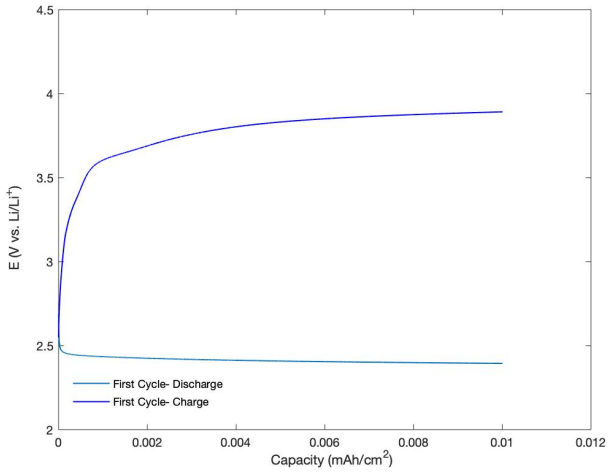

Figure 16: One full galvanostatic cycle of a gold cathode vs a lithium anode in a 1 M $LiNO_3$ in DMSO electrolyte solution at an applied current of 10 µA/cm^2

2.3.4 Electrochemical Impedance Spectroscopy

Electrochemical Impedance Spectroscopy (EIS) uses the impedance in the cell to better understand the relationship between the current and the voltage in an electrochemical system. The impedance is a measure of a system's resistance to current flow[6]. Ohm's law is used to relate the resistance to the voltage and the current as shown below in equation 20[6]:

$$V = IR \tag{21}$$

When performing EIS, the voltage is typically oscillated over a specified frequency range and the output signal is measured to obtain the impedance of the system. This can complicate the impedance calculation due to the phase shift between the input oscillating voltage and the current response, but this will be discussed later. The impedance of the system can be used to fit an equivalent circuit diagram. These diagrams can become very complicated, but a simple Randle's circuit can model the electrical response of an electrochemical system[6]. The Randle's circuit, shown in Figure 17, consists of two resistors and a capacitor[6]. The resistor in parallel with the capacitor represents the charge-transfer resistance, R_f, while the capacitor in the circuit represents double-layer charging, C. The sum of these two currents represent the total current evolution of the system. The resistor in series with the circuit represents the electrolyte resistance, R_Ω [6].

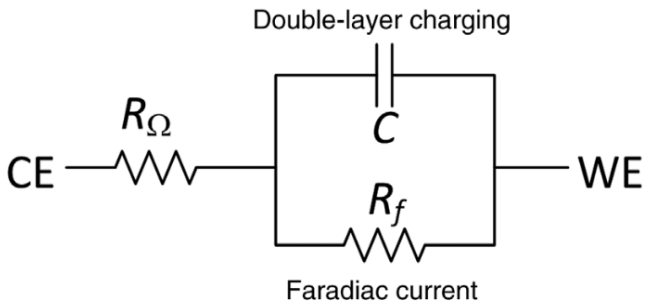

Figure 17[6]: Randle's circuit to model the electrical response of electrochemical systems

In Figure 17, CE represents the counter electrode and WE represents the working electrode. The two variables in the circuit represent the two ways that current can flow to the electrode surface. Double-layer charging, C, does not involve electron transfer and is a non-faradaic current, while the charge-transfer resistance, R_f, represents the current evolution that is due to electrons being transferred at the electrode surface (reduction/oxidation reactions)[6].

The impedance of a resistor is simple to calculate. To obtain the impedance for the resistor, the equation is[6]:

$$Z = R \tag{22}$$

Where the impedance is Z and the resistance is R. The correlation between the current and the voltage for a capacitor is more difficult to calculate. The time-dependent relationship is given below[6]:

$$I(t) = C\frac{dV(t)}{dt} \tag{23}$$

Since the input voltage is oscillating, it can be described by the sum of both a cosine and sine wave as shown below in equation 24[6]:

$$V(t) = \Delta V[\cos(\omega t) + j\sin(\omega t)] \tag{24}$$

This equation can be plugged into equation 23 to obtain the time-dependent current response. The relationship between the impedance, the voltage, and the current is as follows[6]:

$$Z(\omega) = \frac{V(t)}{I(t)} = r(\cos\varphi + j\sin\varphi) = -\frac{1}{\omega C}j \tag{25}$$

As shown in equation 25, the impedance has both a real and an imaginary component and is not time dependent. Generally, Nyquist plots are used to analyze the impedance experimentally because they have both a real and an imaginary axis. A schematic of a Nyquist plot is shown in Figure 18.

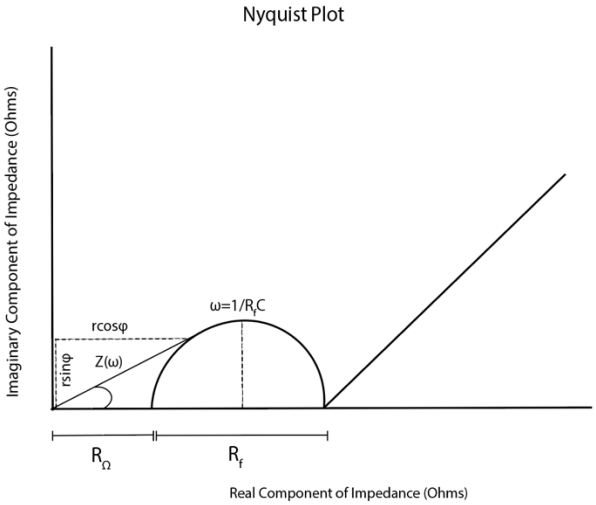

Figure 18: Representation of an Electrochemical Impedance Spectroscopy plot

In Figure 18, R_Ω is a measure of the resistance of current flow through the electrolyte. R_f is the charge-transfer resistance that represents the current evolution that is due to oxidation/reduction reactions occurring on the electrode surface. As mentioned previously, the double-layer charging capacitance, C, does not involve electron transfer and is a non-faradaic current. This capacitance can be calculated experimentally using the following equation[6]:

$$\omega = \frac{1}{R_f C} \tag{26}$$

2.4 Introduction to Stress

Materials are exposed to both structural and interfacial deformations during a variety of chemical processes that cause stress generation[122]. This stress generation can lower the lifetime of materials and impact their structural integrity. This motivates research to investigate the mechanisms that cause stress generation, and how to design materials with this in mind. Research has been conducted in the areas of electrodeposition[123,124], corrosion[125–127], electrocatalysis[128], electrodeposition[129], Li-ion batteries[130,131], and solid-oxide fuel cells[132] to identify the mechanisms behind stress generation for each of these applications. In order to better understand how the stress is generated and evolves during these chemical processes, in-situ techniques have been developed to measure changes in the

stress with respect to a variety of variables such as time, applied potential, and growth rate of the deposited film [133–137].

Stress evolution in materials can be determined using both X-ray Diffraction (XRD) and by measuring the curvature[125]. X-ray Diffraction can only be used on crystalline materials and it is a very sensitive technique[138]. Since curvature measurement techniques can be used to monitor the stress evolution in both crystalline and non-crystalline materials, it is used very frequently. In order to calculate the stress evolution in materials using curvature measurement techniques, the Stoney's equation can be used. The Stoney's equation directly relates the curvature to the stress evolution in materials, and it can be used in a variety of curvature measurement techniques. One requirement to use Stoney's equation is the use of an inert, stiff substrate when performing the curvature measurements. Stress evolution induces bending in materials, which leads to curvature evolution. The relationship between this curvature and the stress generation is given below in the Stoney's equation [139,140]:

$$F = \int_0^{h_f} \sigma dh_f = \frac{E h_s{}^2 \kappa}{6(1-\nu)} \tag{27}$$

Where F represents the in-plane force per unit width of the film, E_S is the substrate's Young's Modulus, ν is Poissons ratio of the substrate, and h_S is the substrate thickness. The substrate curvature is represented by κ. The application of Stoney's equation requires the following conditions[125,141]:

- The thickness of the deposited film, h_s has to be much greater than the thickness of the substrate f by an order of 10^3
- The thickness of the substrate is minimal compared to its lateral directions
- The length of the substrate must be greater than the width of the substrate
- The film and the substrate are both linearly elastic, homogeneous and isotropic
- The strain and rotations of the film are both infinitesimal
- The edge effects near the outermost edges of the substrate are assumed to be negligible

2.5 Techniques to monitor curvature

There are several techniques developed to monitor in-situ curvature evolution in substrates during electrochemical cycling such as a single-beam deflectometry[142], a single-beam scanning deflectometry[137,143], a mult-beam optical sensor (kSA MOS)[123,144], phase-shifting curvature interferometry[145], and dilatometry[146]. In single-beam deflectometry, a single laser beam is reflected off of the sample surface and travels through a beam splitter to a position sensitive detector (PSD), which monitors the position of the laser beam on the sample surface[142]. In single-beam scanning deflectometry, a single laser beam is reflected off of an oscillating mirror and scans along the length of the sample surface[143]. The deviation in the position of the scanning length on the sample is detected using a position sensitive detector (PSD). It provides more precise measurements than single-beam deflectometry without scanning capability because the curvature is monitored over a wide range of the sample surface. Unlike the deflectometry techniques, phase-shifting curvature interferometry measures the curvature by interfering the two reflected beams from the sample surface. The phase-shifting curvature interferometry method measures the path length difference by introducing phase shift between the reflected beams from the sample surface and path length difference is correlated with the curvature in the substrate[145]. A dilatometer technique probes the changes in the length of the electrode while scanning the potential and stress is calculated with respect to change in length[146]. The multi-beam optical sensor is discussed in detail in Chapter III.

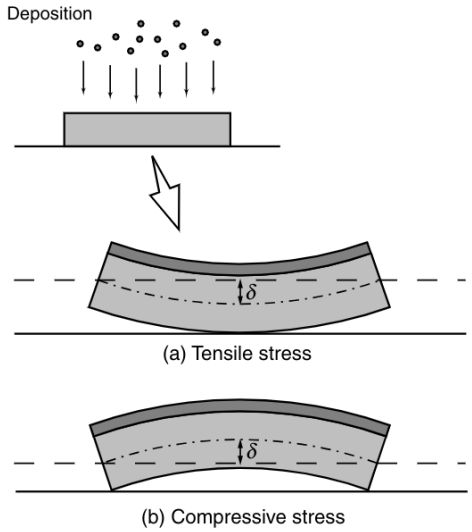

Figure 19[147]**:** Depiction of compressive versus tensile stress in materials

Figure 19 shows how the accumulation of stress affects a material during electrodeposition[147]. Deposition induces curvature in both the substrate and the thin film. As tensile stress evolves, the thin film elongates which can cause fracturing in the film. The magnitude of the stress indicates how much curvature is induced in the film with respect to its original position. As compressive stress evolves, the thin film begins to buckle inward and shrink, which can also cause particle fracturing[148]. The sign of compressive stress is negative, while the sign of tensile stress is positive[149].

Although stress can be measured on a variety of materials, the focus will remain on the stress evolution occurring in thin films. Stress evolution in thin films can have a variety of origins, but they mostly originate from changes within the grains located within the thin film or changes that take place at the grain boundaries[136]. Possible origins of the stress that takes place within the grains include lattice mismatches[150,151], thermal expansions[152], and the introduction of vacancies or interstitials[136]. This stress occurs from changes that take place within the film structure. One example is the intercalation of atoms within the thin film such as the lithiation of a material[144]. The intercalation of atoms introduces interstitials within the film.

Another type of stress that could occur is stress associated with changes that take place at the grain boundary. This stress originates from changes on the surface of the film, rather than within the surface of the film. Possible origins for stress evolution occurring at the grain boundary includes island coalescence and the accumulation of atoms on the surface of the film[136]. One example of this type of stress would be electrodeposition. Electrodeposition is the process of depositing a film of atoms along the surface of another substrate. This does not change the interior structure of the substrate, but it does change the grains on the surface of the film.

2.6 Investigations into the Origin of Stress Evolution

2.6.1 Island Coalescence

One origin of stress generation is known as island coalescence. Island coalescence occurs when individual nuclei come together to form larger nuclei (or islands)[153,154]. At the onset of island coalescence, a large tensile stress is observed. This tensile stress occurs due to the formation of grain boundaries between the neighboring nuclei on the surface of the thin film. Hoffman suggested that as these neighboring nuclei came together, the interfacial energy of each was reduced[154]. Before island coalescence begins to occur, the individual nuclei begin to nucleate onto the surface of the thin film. Before these nuclei begin to come together, a period known as pre-coalescence occurs[136,153]. Pre-coalescence typically induced compressive stress on the thin film. The individual nuclei have a higher density as compared to its density at equilibrium. This increase in density leads to an accumulation of compressive stress in each individual nuclei[136].

2.6.2 The Deposition of Nuclei at Grain Boundaries

As mentioned previously, during island coalescence, grain boundaries are formed between the neighboring nuclei which induced tensile stress. Although tensile stress is observed during island coalescence, compressive stress can also be induced by grain boundary formation[136]. During island coalescence, the nuclei come together to form islands, and these islands come together to form a

film. After the initial film formation, incremental stress on the film begins to evolve[136,153]. This incremental stress is the stress formed in each incremental layer of the film that is formed during island coalescence[136,153].

After island coalescence, the incremental stress can slowly become more compressive after a uniform film has been formed from the individual nuclei. The incremental stress evolution is dependent on the growth rate of the film, the rate of diffusion during deposition, and the size of the nuclei[136,153]. As mentioned previously, at the onset of island coalescence, the stress-thickness transitions from compressive (during pre-coalescence) to tensile. Three different observations have been observed after this occurs: increasing tensile stress during deposition, tensile stress evolution followed by a relatively constant stress-thickness, and a transition from tensile stress to compressive stress-thickness evolution[153].

These observations are dependent on the growth rate of the film, the rate of diffusion during deposition, and the size of the nuclei as mentioned previously[136,153]. When the product of the growth rate of the film and the grain size of the nuclei is larger than the rate of diffusion, the stress-thickness is predicted to become increasing tensile during deposition[136]. When the product of the growth rate of the film and the grain size of the nuclei is smaller than the rate of diffusion, the stress-thickness is predicted to transition from tensile to compressive after island coalescence[136]. The velocity of grain boundary formation can also impact the stress-thickness. The velocity of grain boundary formation describes the velocity that grain boundaries are formed during island coalescence. This velocity can stagnate and approach a steady state value for films with large thicknesses[153]. In this case, the stress is tensile during island coalescence and comes to a steady state stress-thickness value[153].

Figure 20 shows the third observation, where the tensile stress transitions to compressive stress evolution after island coalescence[136]. The thickness of the film affects the stress-thickness

evolution during the deposition on silver onto a silicon dioxide substrate[136]. In the figure, $\bar{\sigma}$ represents the average stress-thickness (N/m), $\sigma(h_f)$ is the incremental stress, and h_f is the thickness of the film (nm). In Figure 20(d), the average stress at any point is the slope of the line drawn from the initial stress-thickness value (given at 0), to the stress-thickness value at a specific film thickness, h_f[136]. The incremental stress is represented as the slope of the tangent line drawn from the stress-thickness value at a specific film thickness, h_f[136]. The figure shows that the average stress changes with film thickness, and that the incremental stress is not equal to the stress-thickness. The stress is assumed to stay the same in lower layers of the film, but changes with the addition of newly formed layers. In this specific case, when the film thickness is approximately 50 nm, as shown, the incremental stress-thickness is compressive while the average stress is tensile.

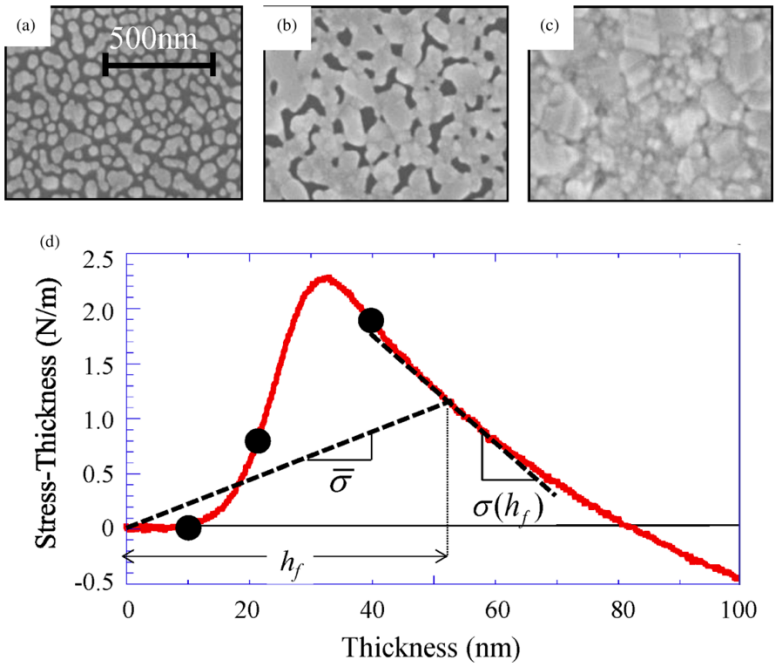

Figure 20[136]**:** Depiction of stress-thickness evolution with respect to the thickness of the film

Figure 20(a-c), shows TEM images of the silver nuclei to show the morphological changes as it is deposited onto the silicon dioxide substrate. The spacing between the individual nuclei in Figure 20(a) is apparent when the film is 10 nm, and the average stress is minimal. This is likely right

before the onset of island coalescence. Figure 20(b) shows very little spacing between the individual nuclei when the film is 22 nm. They have merged together to form new grain boundaries between the neighboring nuclei, which occurs during island coalescence. Both the average stress and the incremental stress are tensile, and the magnitude of the stress-thickness begins to increase rapidly. Figure 20(c) shows no spacing between the nuclei at a film thickness of 40 nm. It appears that new nuclei have nucleated on top of the previously formed film. This stage occurs after island coalescence. This is the point where the average stress is tensile, while the incremental stress is compressive. As mentioned previously, this transition into the compressive stress-thickness regime is likely a result of the product of growth rate of the film and the grain size of the nuclei being smaller than the rate of diffusion[136].

CHAPTER III

IN SITU STRESS MEASUREMENTS ON A THIN FILM Au CATHODE DURING THE FIRST DISCHARGE OF LI-O2 BATTERIES

Abstract

The formation and growth of the Li_2O_2 discharge product impacts the reversibility of the oxygen evolution and reduction reactions in Li-O_2 batteries which may lead to a shorter cycle life. A clear understanding of the surface reactions and the growth mechanism of Li_2O_2 requires probing dynamic changes on the surface of the cathodes in situ during the discharge of a Li-O_2 battery. To investigate this, an experimental system has been established by adopting a multi-beam optical sensor (MOS) and developing a custom-made battery cell. First, the accuracy and reliability of the system was demonstrated by analyzing the stress accumulation on the Au anode during Li plating/stripping, and the results were consistent with an earlier single-beam scanning deflectometry report. Then, the Li-O_2 battery was discharged by applying either linear sweep voltammetry or by applying constant current under an O_2 environment. Stress generation during the first discharge demonstrates characteristic dependance on the type of solvent (DMSO vs diglyme). Control experiments in Argon-saturated electrolytes indicate surface stress generation due to adsorption of solvated ions. The stress generation on Au cathode is attributed to the formation of Li_2O_2 reaction products on the Au surface as well as the adsorption of the ions.

Key words: lithium peroxide, curvature, surface stress, Li-O_2 battery, thin film

3.1 Introduction

Rechargeable non-aqueous Li-O_2 batteries have attracted much attention due to their high theoretical (3500 Wh/kg) and practical (1000 Wh/kg) specific energy, which is almost 3-5 times greater than the conventional Li-ion batteries, which makes them a promising candidate in the use of both electric vehicles and energy storage technologies[13]. However, Li-O_2 batteries are still far from commercialization due to their severe problems during cycling. The performance of Li-O_2 batteries is compromised by both their poor cycle life and low practical capacity due to interfacial instabilities on the surface of the electrodes. Although there has been significant progress on elucidating the relationship between the surface chemistry on the overall performance of Li-O_2 batteries, the governing mechanisms controlling the complex interfacial reactions on the cathode surface have not been fully understood. Elucidating the relationship between the mechanical deformations that result during cycling, as well as the morphological changes of the Li_2O_2 particles is essential for controlling the growth of discharge products in Li-O_2 batteries.

The oxygen evolution reaction (OER) and the oxygen reduction reaction (ORR) at the cathode surface are the major reactions that occur during the electrochemical cycling of Li-O_2 batteries (equation 28). During the discharge cycle, the oxygen reduction reaction leads to the generation of lithium peroxide, Li_2O_2. In the subsequent charge cycle, Li ions and oxygen gas are generated at the cathode surface upon the oxidative decomposition of the generated Li_2O_2 species.

$$2Li^+ + 2e^- + O_2 \rightleftharpoons Li_2O_2 \quad (28)$$

$$Li^+ + e^- + O_2 \rightleftharpoons LiO_{2(\text{ads or sol})} \quad (29)$$

$$2LiO_{2(\text{sol})} \rightleftharpoons Li_2O_2 + O_2 \quad (30)$$

$$LiO_{2(\text{ads})} + Li^+ + e^- + \rightleftharpoons Li_2O_2 \quad (31)$$

The formation mechanisms of the discharge product have a profound impact on the reversibility of the ORR/OER reactions and cycle life of Li-O_2 batteries[31]. There are two primary mechanisms

proposed to describe the growth of Li_2O_2 on the cathode surface: a surface-based mechanism and a solution-based mechanism. The roots behind these reaction pathways were found to be highly dependent on the electrolyte solvent donor number (DN) and the ionic association strength of the lithium salt[56]. In both cases, the first step is the formation of the intermediate reaction product of LiO_2 (equation 29)[31,59,89]. The next step depends on the solubility of the LiO_2 in the electrolyte. In high DN solvents, toroid-shape Li_2O_2 forms in the electrolyte via a disproportionation reaction in the solution, which provides high discharge capacities (equation 30)[31,51].

In low DN solvents, adsorbed LiO_2 species undergoes a either a second electron transfer or disproportionation to form insulating Li_2O_2 thin films via a surface growth mechanism, which causes a short cycle life and poor round trip efficiency, yet yields a low charge overpotential[31,51] (equation 30). The presence of the LiO_2 reaction intermediate has been identified by many studies such as Raman spectroscopy[155,91], UV-Vis spectroscopy[156,157], XRD[158,159], OEMS[158,160], XPS[161,162], XANES[75,163], X-ray transmission microscopy[164,165] and electron paramagnetic resonance[166]. These studies have strong capabilities to identify the chemistry and morphology of the reaction products; however, there is still a lack of knowledge regarding the nucleation and morphology of Li_2O_2 during discharge.

In-operando stress measurements have been applied to various electrochemical and electrocatalytic application areas in order to probe the dynamic changes on the surface of the materials. The stress evolution has been measured in metal oxides during anodic oxidation[167–169] and volumetric changes in Li-ion batteries during lithiation[130,170] are investigated by measuring strain induced in-plane stress. Curvature measurements have also employed to study the adsorption of reaction intermediates during the electrodeposition of Pd[171], corrosion of metals[127,172], oxidation of CO[173,174] and the oxygen reduction reaction[175,176]. These measurements provide insight into the relationship between bonding configurations at the surface of the electrodes and the chemistry of the materials (electrodes and/or electrolytes)[173].

The design and the validation of an experimental setup to probe the in-situ stress evolution on the cathodes for Li-O_2 batteries is reported below. The discharge reactions on the surface of the cathodes in Li-O_2 batteries involve complex steps of adsorption of species, electron transfer, and dissolution of reaction intermediates and the formation of insulating film products. Also, it requires material interaction in three different phases (gas, solid, and liquid). These are challenging factors to utilize stress measurements for Li-O_2 batteries. A multi-beam optical sensor (MOS) was used to monitor the curvature evaluation in the electrode. A custom electrochemical cell which allows optical access for stress measurements and enables saturation of the electrolyte with oxygen gas. The accuracy of this experimental setup was verified by performing surface stress measurements during lithium plating/stripping on Au electrodes in Li-ion batteries, which was previously reported by single-beam scanning deflectometry technique[137]. Then, Au thin films were used as cathode in a Li-O_2 battery configuration, and the cell was discharged in both a 1 M $LiNO_3$ in diglyme and a 1 M $LiNO_3$ in DMSO electrolyte via linear sweep voltammetry as well as galvanostatic discharging. In the diglyme solvent, a tensile stress generation was observed on the electrode surface at potentials lower than 2.45 V, which is associated with the onset of the oxygen reduction reaction occurring in 1 M $LiNO_3$ in diglyme[96]. In the $LiNO_3$ in DMSO electrolyte, a compressive stress generation was observed on the electrode surface at approximately 2.6 V, which is correlated to the formation of Li_2O_2 [56].

3.2 Experimental

3.2.1 Electrochemical Cycling

0.2 mm-thick borosilicate glass coverslips (3.9 mm width x 22 mm length diced cantilever) coated with a 5 nm Cr adhesion layer and a 50 nm layer of Au were purchased from Angstrom Engineering. The anode used was Li foil (99.9% metal basis, Alfa Aesar). The Au was used as an anode electrode for Li-ion batteries and as a cathode for the Li-O_2 battery configuration. The cell was used in a two-electrode cell configuration and the potentials were referenced with respect to a lithium metal

counter electrode. For Li-ion battery testing, the electrolyte was 1 M $LiClO_4$ in PC. The electrolyte solution was prepared inside a glovebox in an Argon environment (<3 ppm O_2 and H_2O environment). The lithium perchlorate salt ($LiClO_4$, 99.9%, battery grade, Sigma Aldrich) was mixed in propylene carbonate (PC, 99.9%, H_2O < 10 ppm).

First, the Au anode was placed inside the custom electrochemical cell outside the glovebox. Then, the cell was placed inside the glovebox to place the lithium foil and fill with electrolyte solution. After assembling the cell inside of the glovebox, the cell was taken out and placed on the optical table. The beam array along the length of the cantilever was then aligned, the servo mirror was calibrated, and a reference was taken prior to performing in-situ stress measurements. Cyclic voltammetry over a potential range of 0.3 to 2 V at a scan rate of 1 mV/s.

In the Li-O_2 battery experiments, the electrolyte was 1 M $LiNO_3$ in Diglyme or 1 M $LiNO_3$ in DMSO. The electrolyte solution was prepared inside a glovebox in an Argon environment (<3 ppm O_2 and H_2O environment). The lithium nitrate salt ($LiNO_3$, 99%, ReagentPlus, Sigma Aldrich) was mixed in either diethylene glycol dimethyl ether (Diglyme, anhydrous, 99.5%, Sigma Aldrich) or in a dimethylsulfoxide (DMSO, anhydrous, 99.9%, Sigma Aldrich) solvent to prepare the electrolyte solution in the Argon-filled glove box. The Au cathode was placed inside the custom cell outside of the glovebox. Then, the lithium foil was placed into the cell inside the glovebox. The cell was then filled with the electrolyte solution. The two PTFE barbed adapters were screwed into the cell inside of the glovebox to ensure that the cell was sealed in an argon environment and plastic tubing was secured onto the PTFE adapters with tube clamps.

For the oxygen-saturated electrolytes, the custom cell was taken out of the glove box and the electrolyte was purged with ultra-high purity oxygen prior to electrochemical cycling using fluorinated ethylene propylene (FEP) tubing. The electrolyte was directly saturated with oxygen for 45 minutes at atmospheric pressure and a flow rate of approximately 45 mL/min. This electrolyte saturation technique was previously employed by in situ Raman studies for lithium-

oxygen batteries[29,55]. After oxygen saturation, the tube clamps attached to the gas inlet/outlet were sealed. Then, the cell was placed on optical table. The beam array along the length of the cantilever was then aligned, the servo mirror was calibrated, and a reference was taken prior to performing in-situ stress measurements. The Au cathode was discharged via linear sweep voltammetry at 1 mV/s or galvanostatic discharging by applying a constant current at 10 μA/cm^2 for an hour.

3.2.2 Curvature Measurement Technique

The generation of stress in the film induces bending, which causes curvature of the substrate. A short summary of the curvature measurement techniques used for various electrochemical applications is detailed in Chapter II. The Stoney equation was used to calculate the stress-thickness product from measured curvature of the substrates[139,177]:

$$F = \int_0^{h_f} \sigma(z)dz = \frac{E_s {h_s}^2 \kappa}{6(1-\nu)} \tag{32}$$

Where h_f is the thickness of the film, F is the in-plane force per unit width of the film, E_S represents the substrate's Young's modulus, h_S is the thickness of the substrate, ν is the Poisson's ratio, and the substrate curvature is represented by κ. The kSA Multi-beam Optical Sensor (MOS*)* system was used to measure the wafer curvature in this study. The description of the MOS system is described in the Appendix A and Appendix C. Changes in the distance between the laser beam array with time is recorded by the MOS system. The correlation between the distance between the beams and the wafer curvature that results is given by the following equation[178]:

$$\Delta\kappa = \frac{d(t) - d_i}{d_i} \frac{\cos(\alpha_i)}{2l n} \tag{33}$$

Where the distance between the beams at time t is given by d(t), the initial distance between the beams is given by d_i, the distance between the substrate and the CCD camera is given by l, the refractive index of the solution is given by n, and the incident angle is given by α_i[178]. The refractive

index was measured by an RBD-6000 Series Refractometer and it is 1.4264, 1.4164, and 1.4095 for the 1 M $LiClO_4$ in PC electrolyte, the 1 M $LiNO_3$ in Diglyme, and the 1 M $LiNO_3$ in DMSO respectively.

3.2.3 Electrochemical Custom Cell Design

The curvature measurements require optical access to the back of the cantilever and Li-O_2 batteries require saturation of the electrolyte with oxygen gas. A custom electrochemical cell was designed that allows in situ curvature measurements to be conducted on Li-O_2 batteries. Information regarding the assembly of the cell can be found in Appendix D. The cell is a two-electrode system composed of a polychlorotrifluoroethylene (PCTFE) main body that can be used to cycle both Li-ion and Li-O_2 batteries. The cell features a quartz window used for optical access of beams to the back side of the substrate. The cell is composed of two quartz windows on both sides.

The quartz window placed in front of the Au cantilever has a 4° angle, in order to avoid any reflections between quartz window and the surface of the cantilever. The quartz window is placed between the O-ring on the main body of the cell and the O-ring on the front and back plate. Two stainless-steel current collectors used to hold both the working and counter electrodes in a vertical orientation. A front/back steel plate is used to seal the cell and mount it to an aluminum breadboard. The 316 stainless steel current collectors have two screws, and the electrodes are placed between the metal plates via screwing them on both sides. Both current collectors have an

EPDM (ethylene propylene diene monomer rubber) O-ring between their top side and main body of the cell. The front/back plate also has an EPDM O-ring, along with the main body of the cell.

The custom cell was assembled inside the glove box filled with Argon gas. The gas inlet was used to fill the cell with electrolyte. The typical electrolyte level is represented in Figure 21, where it rises just below the bottom of the stainless-steel current collector. A polytetrafluoroethylene

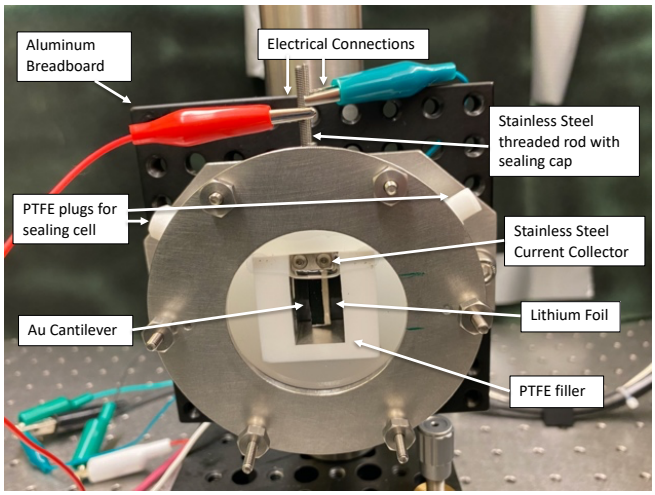

Figure 21: Picture of the custom electrochemical cell designed for in situ curvature monitoring while cycling Li-ion or Li-O_2 batteries.

(PTFE) filler is used to decrease the amount of electrolyte inside the cell to 10 mL. Two stainless-steel threaded rods are screwed into the two stainless steel current collectors to provide the electrical connection, and stainless-steel caps are screwed onto the two threaded rods and placed on the surface on the main body of the cell to ensure it is sealed. The cell was sealed by using either the closed PTFE plugs (for the Li-ion configuration), or the PTFE barbed adapters (for the Li-O_2 configuration). These were screwed into the cell after filling it with electrolyte solution. After the cell was filled with electrolyte, it was taken out of the glovebox and placed on the optical table. In order to accurately measure the volume of electrolyte needed, a picture of the cantilever inside the cell is taken and the length to pixel ratio was used to determine the active area of the Au cantilever that was immersed in the electrolyte solution.

3.3 Results and Discussion

3.3.1 Stress evolution on an Au Anode in a Li-ion Battery

In order to verify the in situ stress measurement setup, in situ stress measurements were performed using an Au cantilever as the anode. The Au cantilever was cycled under similar conditions with a previously published study by Tavassol et al. that used a scanning beam deflectometry system to monitor the stress evolution[137]. A cantilever with a thin Au film was discharged/charged via cyclic voltammetry at 1 mV/s between 0.3–2.0 V against a Li counter electrode in 1 M $LiClO_4$ in PC. Figure 22 shows the current evolution and stress development in the Au anode during the third electrochemical cycling. The cathodic scan refers to the potential sweep from a higher to a lower potential, and the anodic scan takes place when the applied voltage increases linearly with time.

Figure 22A shows characteristic features in the current response during the anodic and cathodic scans between 2.0 to 0.3 V vs $Li/Li^{0/+}$. A broad cathodic peak is observed at around 0.85 V and it was associated with the Li deposition and alloying with the Au surface[179–181]. Another cathodic peak is recorded at around 0.45 V, which is associated with the decomposition of the perchlorate ion from the lithium salt[137]. As the voltage is further decreased to 0.3 V, a sharp decrease in the current response is seen at 0.3 V; this peak is near the onset of bulk lithiation, which was determined to begin at approximately 0.2 V[137,179]. During the anodic scan, the current response sharply increases between 0.3 and 0.4 V. Another sharp increase with the emergence of an anodic current peak located at around 1.0 V is attributed to the stripping of lithium peak from the surface of the Au[179,181].

The associated stress evolution in the Au electrode during anodic and cathodic scan is shown in Figure 22B. The change in the force becomes more compressive as the lithium ions are deposited onto the surface of the Au during the cathodic scan. At the end of the cathodic scan, the stress-thickness product was almost equal to -12 N/m, which is very similar to previous literature

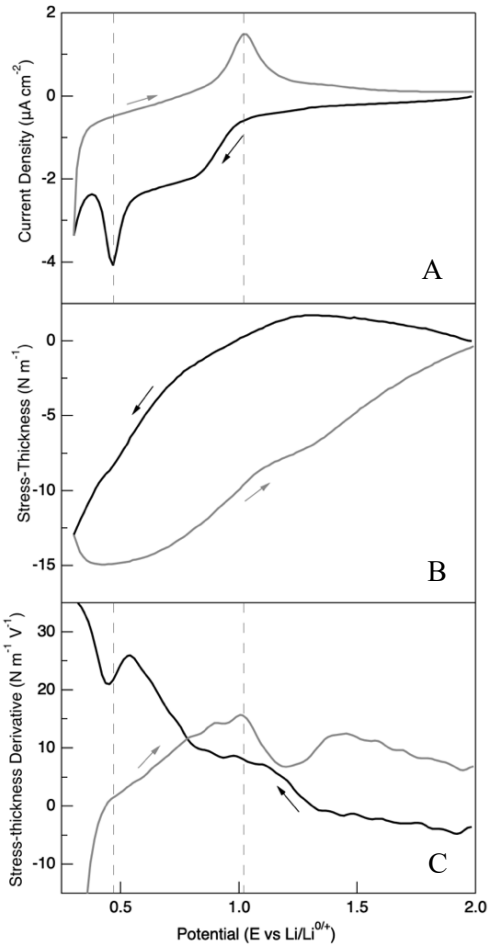

Figure 22: The current density, stress generation, and the first derivative of the stress during the third cycle on Au anode in 1 M $LiClO_4$ in PC at 1mV/s (under Argon environment).

reports[137]. Compressive stress evolution during underpotential deposition has also been reported in other studies upon deposition of Pb[182], Tl[183], Cu[142,184], and Ni[185] onto Au surfaces. The sign of the stress changed from compressive to tensile with the change in the direction of the scan from cathodic to anodic at 0.3 V. At the end of cycle, the stress-thickness product almost returns to its initial value, demonstrating the highly reversible mechanical behavior during the plating and

stripping of lithium on the Au electrode. Similar reversible mechanical behavior is also observed in the second, fourth and fifth cycles (Appendix A Figures A2-A4). Previous QCM measurements have also reported a reversible mass change on Au anodes after lithium plating/stripping [186].

To better understand the localized rate changes in the stress-thickness product, the first derivative of the stress-thickness product with respect to the applied potential is plotted in the Figure 22C. During the cathodic scan, a stress derivative peak is recorded at around 0.45 V, which aligns well with the current peak at the similar potential. During the anodic scan, a major stress derivative peak is recorded at around 1.0 V, which aligns with the anodic current peak around the same potential with a $\pm$0.01 V error margin. The redox reaction of the underpotential deposition of lithium onto the surface of the Au takes place at around 0.75 V during the cathodic scan, while the stripping of Li from Au-Li surface alloy takes place at around 1.0 V during the anodic scan[179,180,187]. Therefore, the stress derivatives at these voltages correlate well with the Li plating and stripping from the electrode surface. The first derivative of the stress-thickness with respect to the applied potential at around 0.45 V is due to the decomposition of the perchlorate ion from the lithium salt[137]. The overall behavior of the stress generation during lithium plating on the Au electrode and stripping from the Au-Li alloy is very similar to previous reports in the literature[137]. Overall, these measurements demonstrate a similar mechanical response with the previous study conducted by Tavassol et al. that used a single-beam scanning deflectometry system[137].

3.3.2 Stress evolution during the formation of Li_2O_2

A cantilever with an Au film was used as the cathode electrode to probe the surface dynamics associated with the oxygen reduction reaction (ORR) during discharge of Li-O_2 batteries. 1 M $LiNO_3$ in diglyme was used as the electrolyte. The Li-O_2 battery was discharged by either applying linear sweep voltammetry (LSV) or constant current against Li metal counter electrode. Figure 23A-C shows the electrochemical and mechanical responses of the electrode prior to and during linear sweep voltammetry with respect to time. Prior to linear sweep voltammetry, the open circuit

potential of the cell was around 2.89 V. The cell voltage decreased at a rate of 1 mV/s until 2.0 V was reached during linear sweep voltammetry.

The current response and force development during liner sweep voltammetry is also plotted against applied voltage in Figure 23D and 23E, respectively. Both the current and force values were minimal until the voltage reached around 2.45 V, which is attributed to the potential where the oxygen reduction reaction takes place[96]. At this point, the current density started to decrease almost linearly with the applied voltage between 2.45 to 2.0 V. Previous electrochemical studies that used Au thin films also reported a similar current response at around 2.45 V during the formation of Li_2O_2 discharge products in the 1 M $LiNO_3$ in diglyme electrolyte[56,96]. The electrode also undergoes tensile stress generation at the onset of the current decay at around 2.45 V around 0.4 N/m from 2.45 to 2.1 V. At the end of the discharge cycle, the stress-thickness product reaches 0.35 N/m. Previous QCM measurements also recorded an increase in the mass accumulation on the Au thin film around similar potentials during discharge in the 1 M $LiNO_3$ in diglyme electrolyte[56]. To further investigate the force development during Li_2O_2 formation, the Li-O_2 battery was discharged by applying a constant current of -10 μAcm^{-2} for one hour. Unlike linear sweep voltammetry, galvanostatic discharging applies a constant flux of ions onto the surface of the electrode. Figure 23F and 23G show the potential and force development plotted against the capacity during galvanostatic discharge. Upon applying current, the potential dropped rapidly from the open circuit potential down to 2.45 V. During discharge, a single potential plateau is observed

at approximately 2.45 V which corresponds to the formation of Li_2O_2 due to the oxygen reduction reaction (ORR)[56,96].

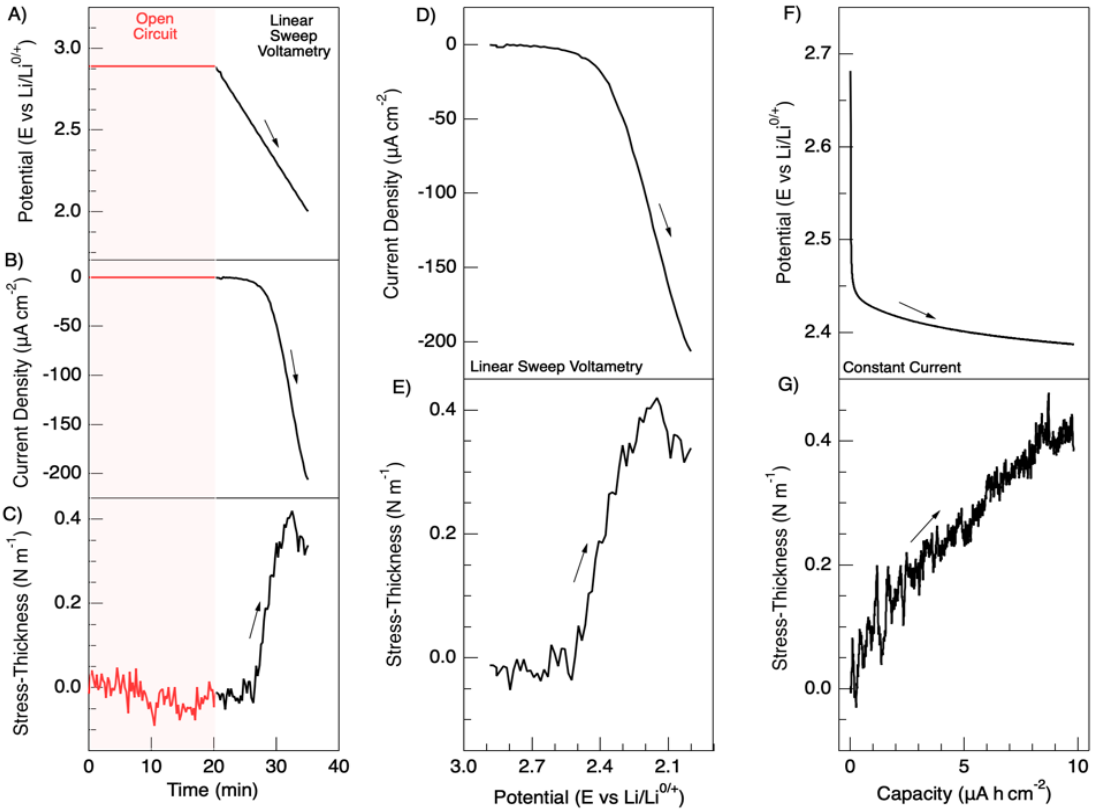

Figure 23: The stress-thickness product development prior to (red line) and during (black line) the oxygen reduction reaction on the Au cathode cycled in 1 M $LiNO_3$ in Diglyme. The cathode was discharged either by linear sweep voltammetry (A-E) starting from the open circuit potential down to 2.0 V by decreasing it by 1 mV/s or via galvanostatic cycling (F-G) at a constant current of -10 μAcm^{-2} for one hour. (A, B and C) show the potential, current density and stress-thickness plotted against time. (D and E) demonstrates the current density and stress-thickness product plotted against the potential during linear sweep voltammetry only. (F and G) shows the potential and stress-thickness product plotted against discharge capacity.

The force was set to zero at the beginning of the discharge cycle. Similar to linear sweep voltammetry, the electrode undergoes a tensile stress generation during the formation of Li_2O_2 during the first discharge. There is an almost a linear relation between the stress-thickness product and the discharge capacity until the force reaches 0.4 N/m.

3.3.3 Surface stress measurements on an Au cathode in oxygen vs argon-saturated electrolytes

Control experiments were conducted to elucidate the impact of the formation of Li_2O_2 on the Au cathode. Figure 25 shows the current evolution and stress generation on the Au cathode discharged in either an argon or an oxygen-saturated electrolyte. The maximum current density was almost four times higher in the oxygen-saturated $LiNO_3$ in Diglyme electrolyte compared to the one cycled in the argon environment. The stress-thickness product continuously increased into the tensile regime while the voltage reduced to 2.0 V in the argon-saturated electrolyte, whereas the stress-thickness reached a plateau beginning at approximately 2.4 V (approximately the potential regime at which Li_2O_2 is formed) and it reached a maximum of 0.4 N/m in the oxygen-saturated diglyme electrolyte (Figure 24A).

The stress evolution in the diglyme solvent is higher than the stress recorded in the $LiNO_3$ in DMSO electrolyte. The tensile stress evolution in the cell under an argon environment may be associated with the adsorption of ions onto the gold surface. Monte Carlo simulations suggest the adsorption of solvated Li ions in diglyme solvent in the outer Helmholtz plane in the cell in an argon environment[188]. Aurbach et al. also speculated about the possible impact of the adsorption on the mechanical behavior of the Pt cathode cycled in a tetraethylene glycol dimethyl ether (TEGDME) solvent[189]. The same stress measurements were also conducted in a $LiNO_3$ in DMSO electrolyte. The DMSO solvent has a higher solvent donor number compared to that of diglyme[13,51,190]. The stress evolution due to the formation of Li_2O_2 formed via the solution pathway is being studied in both electrolytes, but one pathway is driven by the solvent donor number while the other is driven by the high ionic association strength of the salt. A single current peak is observed around 2.5 V in the oxygen-saturated $LiNO_3$ in DMSO electrolyte and it was associated with the formation of lithium peroxide[56]. An increase in the tensile stress was recorded in the early period of the first discharge cycle and stress became more compressive from 2.6 V until 2.4 V. In the cell cycled in an argon environment containing $LiNO_3$ in DMSO, a negligible amount of current and stress

evolution was recorded in the first discharge cycle during linear sweep voltammetry. Overall, the stress measurements conducted in two different solvents demonstrates the impact of the electrolyte solvent on the stress generation on the surface of the Au cathode during the first discharge cycle.

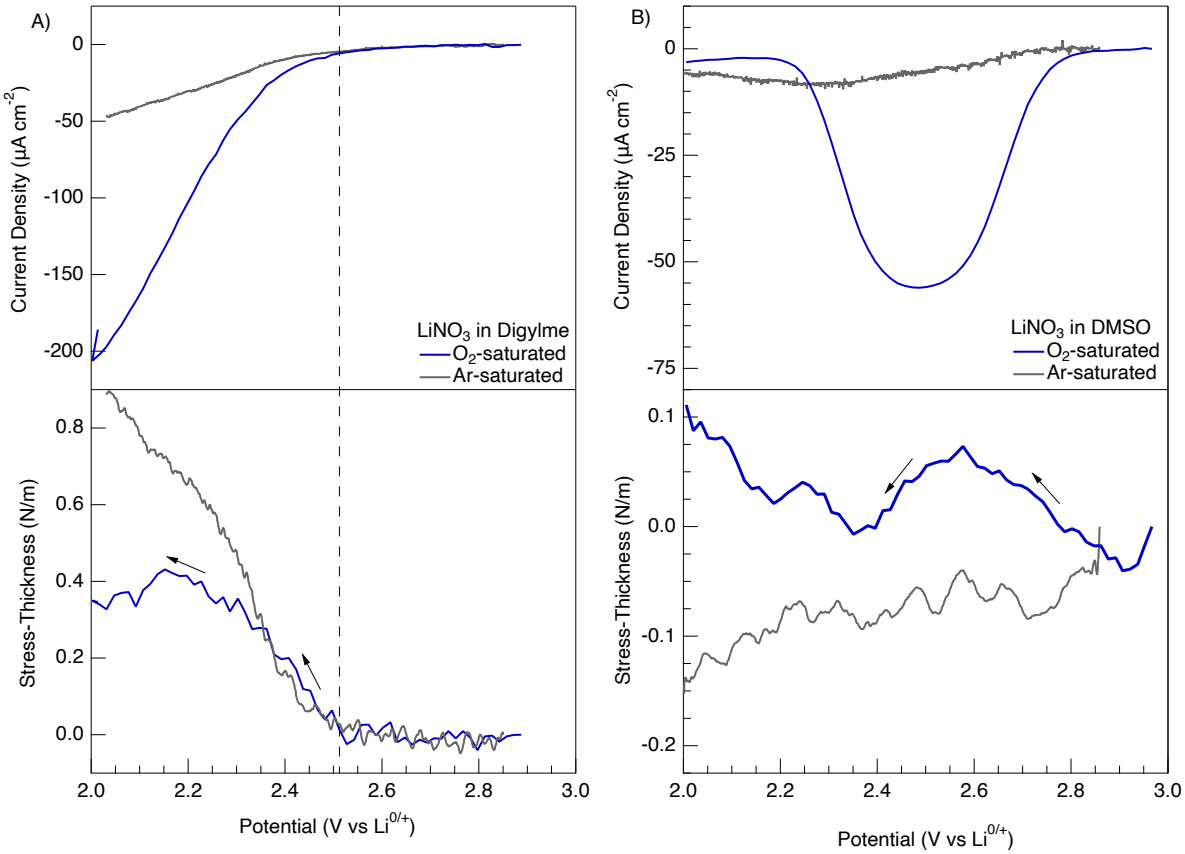

Figure 24: The current response and stress generation on Au cathode during linear sweep voltammetry at 1 mV/s rate until 2.0 V A) in oxygen-saturated (blue) or argon-saturated (grey) $LiNO_3$ in Diglyme electrolyte B) in an oxygen-saturated (blue) or argon-saturated (grey) $LiNO_3$ in DMSO electrolyte

3.4. Discussion

In the first part of the study, the stress evolution on an Au anode was monitored during lithium stripping/plating in a Li-ion battery using a custom electrochemical cell and the MOS system. Similar stress measurements have been performed in many electrochemical/electrocatalytic applications by using various curvature measurement methods, but often they were not validated by other research groups. Stress measurements are complex and many groups have used a variety of curvature measurement techniques. Stress measurements can be influenced by the morphology

of the electrode, residual stress in the electrode, operating conditions during cycling, and the geometry of the custom cells used for the measurements. The high degree of consistency between the single-beam scanning deflectometry results of Tavassol et al. with the MOS results demonstrates the accuracy and reliability of both of these high-resolution curvature measurements[137].

In the second part of the study, the stress generation on an Au cathode while discharging a Li-O_2 battery in a 1 M $LiNO_3$ in Diglyme electrolyte solution was investigated. Figure (24A-E) showed a tensile stress generation occurring as the current density decreases to approximately 2.45 V during linear sweep voltammetry. Figure (24F-G) showed that the electrode undergoes a similar tensile stress generation when the potential reached 2.45 V when galvanostatically discharged. This potential is associated with the oxygen reduction reaction (ORR) occurring in the $LiNO_3$ in diglyme electrolyte. Previous QCM studies observed an increase in the mass accumulation occurring on the electrode surface starting from the potential that the oxygen reduction reaction begins to occur when the electrode was cycled in 1 M $LiNO_3$ in Diglyme[56,96]. Scanning electron microscopy (SEM) images in these studies demonstrated the formation of toroidal-shaped Li_2O_2, as well as semicircular particles composed of round plates stacked on the surface of the Au cathode after discharging. It is important to note that these SEM images were taken after the Li-O_2 battery was discharged until the voltage decayed to 2.0 V during galvanostatic discharge, which took approximately 15 hours[56]. In this study, the early periods of the first discharge were recorded by limiting the discharge time to 1 hour.

Ex situ SEM analysis at various depths of discharge during the first discharge in the TEGDME electrolyte cycle showed that in the early stages of the first discharge, a small amount of Li_2O_2 particles nucleate onto the cathode surface[93]. The particles grow in the later stages of the first discharge while the voltage profile is still around the plateau region. The toroidal-shaped Li_2O_2 clusters were observed towards the end of the first discharge cycle, and this coincides with the

distinct voltage decay from its plateau. As mentioned previously, in the stress measurements that conducted, constant current was only applied for one hour. This suggests that the nucleation of the Li_2O_2 particles in the initial period of the first discharge induces tensile stress generation on the electrode surface in the diglyme solvent.

Chason and Stafford intensively investigated stress profiles during the growth of thin film metals via electrodeposition or vapor deposition methods[133,135,153,191]. For example, during the bulk deposition of Co onto the Au surface, the formation of nuclei coalescence during the early period of deposition generates tensile stress on the electrode[192]. Their studies also demonstrated the impact of the key parameters such as growth rate, grain size and morphology on the generation of stress during film depositing. There are some fundamental differences between the electrodeposition of metals and growing Li_2O_2 particles in Li-O_2 batteries. In the case of the metal deposition, electrodeposited metals are not soluble in the electrolyte, and the surface reaction involves a single electron transfer. The morphological evolution of the Li_2O_2 during the first discharge cycle shows similarities with the electrodeposition of metals. Overall, growth mechanisms involve nucleation as the first step, then nucleation and growth, and finally saturation of the surface. The correlation between the morphology of anodic oxide films and stress build-up during film formation has also been studied [122,127,168]. Unlike metal electrodeposition, the anodic oxide films were formed in an aqueous electrolyte solution, where they are slightly soluble. The final morphology of the oxide films were impacted by the interfacial stress built-up near electrode/electrolyte interface, by the electrolyte composition (salt and solvent choice), as well as the film growth rate[122,127,168].

It should be noted that the generation of discharge product in the Li-O_2 batteries involves complex reaction steps in a electrode/electrolyte interface. There are many factors that may contribute to the formation of Li_2O_2 such as the adsorption energy of the LiO_2 reaction intermediates which dictates the reaction pathway, the donor number of the solvent and the ionic association strength of the lithium salt, and the electrochemical stability of the organic electrolytes,

the kinetics driving the OER/ORR reactions, and the stability of the cathode. Stress measurements in the oxygen-saturated vs the argon-saturated electrolytes in Figure 24 suggests the possible role of the ion adsorption on the surface stress generation. The stress dependence on the solvent species (DMSO vs Diglyme solvents depicted in Figure 24) also indicates the solvent-dependent reaction processes that take place on the electrode surface. By establishing an in-situ stress measurement system, the impact of these factors on the formation and growth mechanisms of Li_2O_2 particles is better understood.

3.5 Conclusions

In summary, a custom electrochemical cell was coupled with the multiple-beam optical sensor to monitor in-situ stress measurements on the Li-O_2 batteries. The experimental system was verified by monitoring the stress generation in an Au thin film anode in a Li-ion battery during lithium plating/stripping. The potential-dependent electrochemical stress generation on the Au anode was similar to the previous single-beam scanning beam deflectometry report. After the system was verified in the Li-ion battery configuration, the stress generation on an Au thin film cathode was monitored in a Li-O_2 battery configuration. The cell was discharged via either linear sweep voltammetry or by applying a constant current. The electrode experienced tensile stress generation during the oxygen reduction reaction (ORR) when cycled below 2.45 V in the Diglyme solvent. Then, the electrochemical behavior using two different solvents was compared. A 1 M $LiNO_3$ in Diglyme electrolyte was compared with 1 M $LiNO_3$ in DMSO. The 1 M $LiNO_3$ in Diglyme electrolyte exhibited tensile stress during discharging. This stress was correlated to the formation of Li_2O_2 and it increased almost linearly with the discharging time after the current to decay. The 1 M $LiNO_3$ in DMSO electrolyte exhibited an increase in the tensile stress in the early period of the first discharge cycle, then it became more compressive around 2.6 V until 2.4 V. This potential regime is associated with the formation of Li_2O_2[56].

Experiments were also conducted in both oxygen and argon-saturated electrolytes to differentiate the stress evolution of the products evolved during the oxygen evolution/reductions reactions from those evolved in an argon environment. In the $LiNO_3$ in Diglyme electrolyte, the stress evolved was higher for the argon-saturated system. This was likely due to the adsorption of lithium cations onto the surface of the Au. This is different from the $LiNO_3$ in DMSO electrolyte that exhibited a lower stress evolution in the argon-saturated electrolyte as compared to the oxygen-saturated system. This demonstrates that the adsorption of lithium cations is different for these solvents, likely due to the difference in donor numbers.

CHAPTER IV

THE IMPACT OF THE LITHIUM SALT/SOLVENT CHOICE ON THE STRESS EVOLUTION DURING CYCLING IN LITHIUM OXYGEN BATTERIES

Abstract

The formation and oxidation processes of lithium peroxide, Li_2O_2, controls the cycle efficiency and the capacity retention in Li-O_2 batteries. The ability of the electrolyte species to promote desirable surface reactions is necessary to achieve a longer cycle life in Li-O_2 batteries. However, the impact of the electrolyte salts on the interfacial dynamics is not well known. To fill this gap, the role of the electrolyte salts on the charge and discharge reactions were investigated on an Au thin film cathode. LiTFSI and $LiNO_3$ salts were dissolved in a DMSO solvent. An in situ curvature measurement technique was employed to probe the dynamic changes on the electrode surface during cycling. During discharging, the type of salt and the presence of oxygen controls the characteristic mechanical deformations occurring on the electrode surface. During charging, the results suggest that the compressive stress at lower voltages is required to oxidize the lithium peroxide product. The accumulation of an insulating thin film of Li_2O_2 likely results in cathode passivation, and the source of the stress is associated with the adsorption of charged species. The outcome of the study demonstrates the importance of the ion adsorption kinetics occurring during charging. Also, the study indicates the salt-dependent complex reaction processes that occur during discharge when the Li_2O_2 forms via the solution-based reaction pathway.

Key words: lithium peroxide, curvature, surface stress, Li-O_2 battery, thin film, adsorption.

4.1 Introduction

Chapter III showed the stress evolution during the electrochemical cycling in lithium-oxygen batteries for the first time. The stress evolution in lithium-oxygen batteries can impact the performance during cycling, as well as the stability of the cathode material. The stress evolution will be compared in two different salts using the same solvent. The salts that will be used are $LiNO_3$ and LiTFSI, which have a high ionic association strength and a low ionic association strength, respectively. The morphology of the lithium peroxide will be taken into account, as well as the mass accumulation of the lithium peroxide product on the surface of the Au cantilever.

Stress measurements were performed in this study and Dr. Malachi Noked's research group will perform SEM, XRD, and QCM measurements on the Au cantilever samples in order to correlate the stress evolution to the morphology of the lithium peroxide product as well as the mass accumulation that occurs during cycling as well. The mass accumulation with respect to the potential can be directly correlated to the dependence of the stress evolution on the potential.

4.2 Experimental

0.2 mm-thick borosilicate glass coverslips (3.9 mm width x 22 mm length diced cantilever) coated with a 5 nm Cr adhesion layer and a 50 nm layer of Au were purchased from Angstrom Engineering. The anode used was Li foil (99.9% metal basis, Alfa Aesar). These Au cantilevers were used as the cathode. The cell was used in a two-electrode cell configuration and the potentials were referenced with respect to a lithium metal counter electrode. The electrolyte solution was prepared inside of an Argon filled glovebox (<3 ppm O_2 and H_2O environment).

The electrolytes used were 1 M $LiNO_3$ in DMSO and 1 M LiTFSI in DMSO. The electrolyte solution was prepared inside a glovebox in an Argon environment (<3 ppm O_2 and H_2O environment). The lithium nitrate salt ($LiNO_3$, 99%, ReagentPlus, Sigma Aldrich) and bis(trifluoromethane)sulfonimide lithium salt (LiTFSI, 99.95%, trace metals basis, Sigma Aldrich)

salts were mixed with dimethylsulfoxide (DMSO, anhydrous, 99.9%, Sigma Aldrich) to prepare the electrolyte solution in the Argon-filled glove box. The Au cathode was placed inside the custom cell outside of the glovebox. Then, the lithium foil was placed into the cell inside the glovebox and the cell was filled with the electrolyte solution. The two PTFE barbed adapters were screwed into the cell inside of the glovebox to ensure that the cell was sealed in an argon environment and then were connected to plastic tubing that was secured with tube clamps.

For the oxygen-saturated electrolytes, the custom cell was taken out of the glove box and the electrolyte was purged with ultra-high purity oxygen prior to electrochemical cycling using fluorinated ethylene propylene (FEP) tubing. The electrolyte was directly saturated with oxygen for 45 minutes at atmospheric pressure and a flow rate of approximately 45 mL/min. This electrolyte saturation technique was previously employed by in situ Raman studies for lithium-oxygen batteries[29,55]. After oxygen saturation, the tube clamps attached to the gas inlet/outlet were sealed. Then, the cell was placed on optical table. The beam array along the length of the cantilever was then aligned, the servo mirror was calibrated, and a reference was taken prior to performing in-situ stress measurements. The Au cathode was cycled via cyclic voltammetry at 1 mV/s.

4.2.1 Curvature Measurement Technique

The generation of stress in the film induces bending, which causes curvature of the substrate. A short summary of the curvature measurement techniques for various electrochemical applications was discussed in Chapter II. The Stoney equation is used to calculate the stress-thickness product from measured curvature of the substrates[139,177]:

$$F = \int_0^{h_f} \sigma(z)dz = \frac{E_s {h_s}^2 \kappa}{6(1-\nu)} \tag{34}$$

Where h_f is the thickness of the film, F is the in-plane force per unit width of the film, E_S represents the substrate's Young's modulus, h_S is the thickness of the substrate, ν is the Poisson's ratio, and

the substrate curvature is represented by κ. The kSA Multi-beam Optical Sensor (MOS) system was used to measure the wafer curvature in this study. The description of the MOS system is described in the Appendix A and C. Changes in the distance between the laser beam array with time is recorded by the MOS system. The correlation between the distance between the beams and the wafer curvature that results is given by the following equation[178]:

$$\Delta\kappa = \frac{d(t) - d_i}{d_i}\frac{\cos(\alpha_i)}{2ln} \quad (35)$$

Where the distance between the beams at time t is given by d(t), the initial distance between the beams is given by d_i, the distance between the substrate and the CCD camera is given by l, the refractive index of the solution is given by n, and the incident angle is given by α_i[178]. The refractive index was measured by an RBD-6000 Series Refractometer and it is 1.4095 and 1.4617 for the 1 M $LiNO_3$ in DMSO and 1 M LiTFSI in DMSO electrolytes, respectively. Additional information regarding the curvature measurement technique can be found in Appendix A and Appendix C.

4.3 Results

4.3.1 Stress Development during Discharging

Figure 25 shows the change in the force progression over time with the corresponding changes in the current response during the discharge cycles containing either LiTFSI or $LiNO_3$ in DMSO. In both electrolytes, a large compressive stress development is observed at high voltages and the stress changes its direction at around 3.5 V for the $LiNO_3$ in DMSO electrolyte and at 2.8 V for the LiTFSI in DMSO electrolyte. The corresponding current response during this compressive stress period is very close to zero, indicating that the compressive stress development should be related

with either a non-Faradaic process or a mechanical relaxation period occurring after the charge cycles. This will be discussed after the stress behavior during charge has been analyzed.

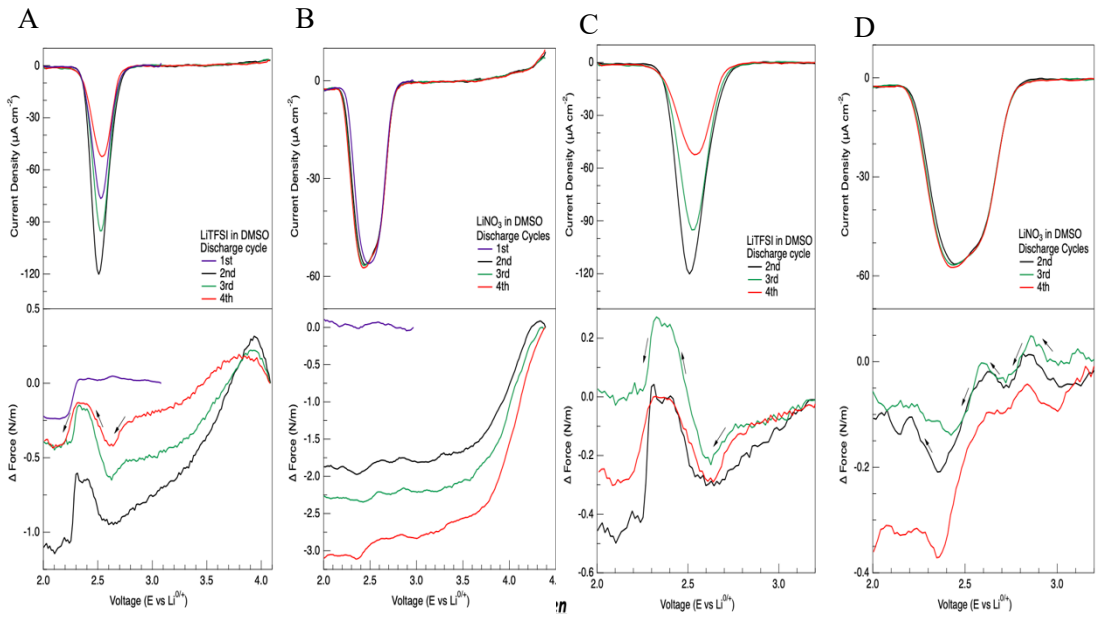

Figure 25: The current response and the force development during discharge cycles 1-4 on the Au cathode cycled in an oxygen-saturated electrolyte of 1 M LiTFSI in DMSO (A and C) and 1 M $LiNO_3$ in DMSO (B and D). Cyclic Voltammetry was conducted from 2-4.1 V for LiTFSI in DMSO (A and C) at 1 mV/s and from 2-4.4 V for 1 M $LiNO_3$ in DMSO (B and D) at the same scan rate. The force was set to zero at the onset of each discharge cycle for Figures A and B. Figures C and D show the current response and the force development from 2-3.2 V for cycles 2-4 for LiTFSI and $LiNO_3$, respectively. The force was set to zero at 3.2 V in Figures C and D to show the complex behaviors in this potential regime.

At the lower potentials, a single current peak is observed at around 2.5 V in both electrolytes. The corresponding voltage of the single current peak indicates the formation of lithium peroxide species on the electrode surface. The lithium peroxide might be formed via a surface-based or a solution-based mechanism. Due to the low ionic association strength of LiTFSI, it is expected to favor the surface-based mechanism, while the high association strength of $LiNO_3$ favors the solution-based mechanism. The magnitude of the current density is progressively decreasing with the cycle number in the LiTFSI-containing electrolyte. This indicates its low efficiency in forming lithium peroxide during discharging and suggests the formation of a thin film of lithium peroxide on the

electrode surface. The magnitude of the current density is very repeatable in $LiNO_3$-containing electrolyte. The associated stress generation during the lower voltage regime during discharging is shown in Figure 25C and D. The stress values were set to zero at 3.2 V to show the stress behavior more clearly. In the LiTFSI-containing electrolyte, the stress changes its direction and becomes tensile (positive stress) at around 2.6 V, followed by a compressive stress generation at around 2.3 V. In the $LiNO_3$-containing electrolyte, the direction of the stress generation changes multiple times, which demonstrates its more complex behavior.

To better understand the governing forces controlling the stress generation in both electrolytes, control experiments were conducted in argon-saturated electrolytes. Figure 26 compares the current evolution and the stress generation in oxygen vs argon-saturated electrolytes during the third discharge cycle. As expected, there were no peaks observed in the current evolution in the argon-saturated electrolytes which demonstrates that the lithium peroxide product was not formed. For the two different salt containing electrolytes, a tensile stress generation was recorded around 2.6 V in the argon-saturated electrolytes which is associated with the adsorption of charged electrolyte species on the surface of the electrode. As more ions were adsorbed at the lower potential, the concentration of adsorbed species changes on the Helmholtz layer on the surface of the electrode. Previous Raman spectroscopy studies show the changes in both the coordinated $TFSI^-$ anion and DMSO molecules on the surface of the Au electrode. At higher concentrations, more $TFSI^-$ species were found on the surface of the electrode and this layer was almost free of DMSO molecules[193]. Due to this, the change in the sign of stress in the argon-saturated electrolyte is likely associated with changes in the adsorbed species on the electrode surface at lower potentials. To track the potential-dependent stress evolution during discharging, the first derivative of the stress was calculated with respect to the applied potential (shown in Figure 27). In the argon-saturated electrolytes, a single stress derivative peak was observed in both the LiTFSI and $LiNO_3$-containing electrolytes. This indicates that in the absence of oxygen, the surface phenomena is

similar in both salts, so we associate this with the adsorption of charged species. On the other hand, more complex surface behaviors were recorded in the oxygen-saturated electrolytes.

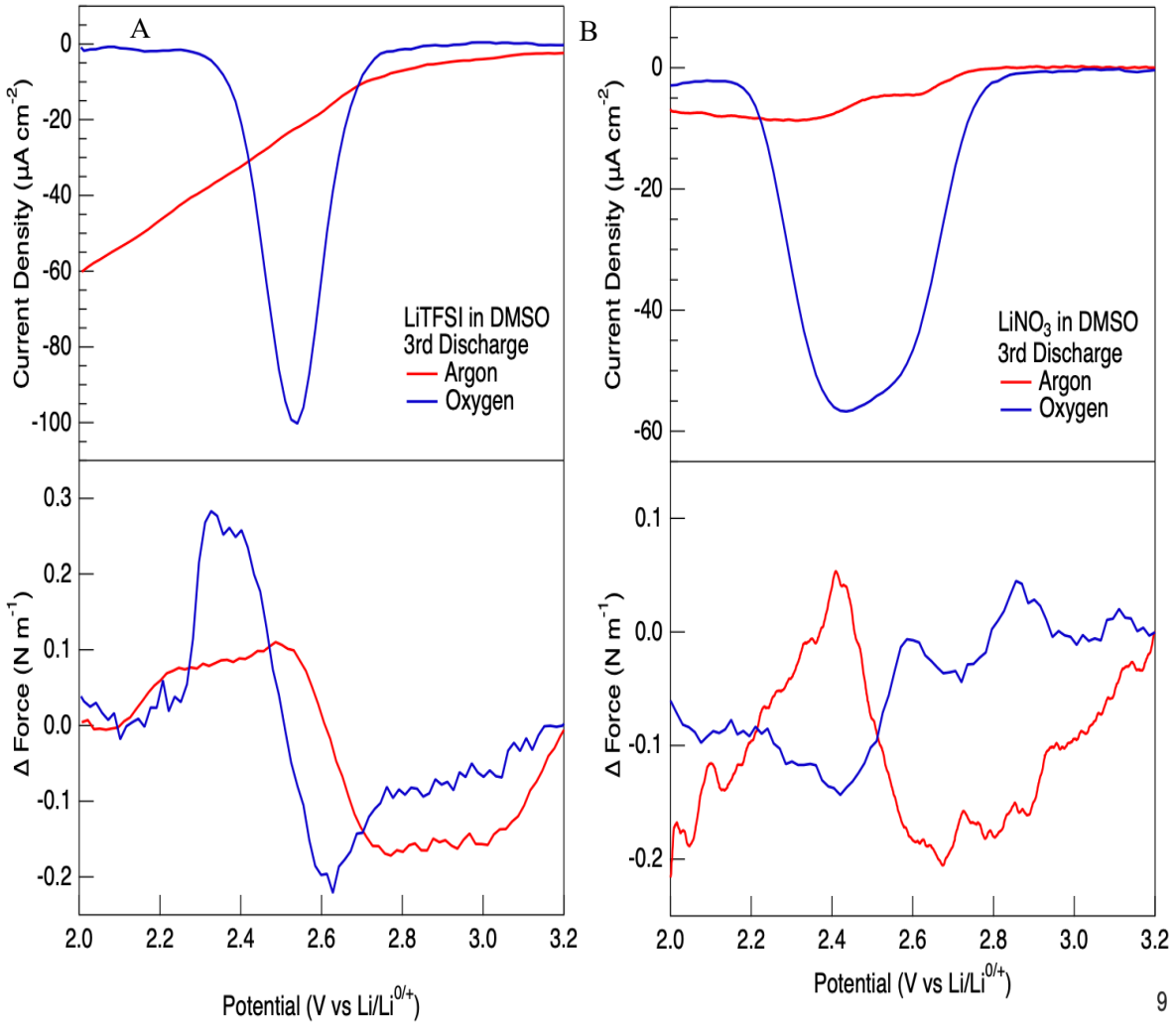

Figure 26: The current response and the force development during the third discharge cycle on the Au cathode cycled in an argon-saturated electrolyte (red line) and an oxygen-saturated electrolyte (blue) of 1 M LiTFSI in DMSO (A) and 1 M $LiNO_3$ in DMSO (B). Cyclic Voltammetry was conducted from 2-4.1 V for LiTFSI in DMSO (A) at 1 mV/s and from 2-4.4 V for 1 M $LiNO_3$ in DMSO (B) at the same scan rate. The force was set to zero at 3.2 V to show the complex behaviors in this potential regime.

In the oxygen-saturated LiTFSI in DMSO electrolyte, the stress derivative becomes negative at the onset of the current decay around 2.8 V. Then, it reaches a local minima around 2.5 V which coincides with the current minima occurring at the same voltage. Once the current becomes almost zero around 2.3 V, the stress derivative changes its direction again. This demonstrates the current

controlled surface stress behavior on the Au electrode in the LiTFSI in DMSO oxygen-saturated electrolyte. For $LiNO_3$ in DMSO oxygen-saturated electrolyte, the stress derivative becomes negative at around 3.1 V, reaches a local minima around 2.9 V, then changes its direction again around 2.8 V.

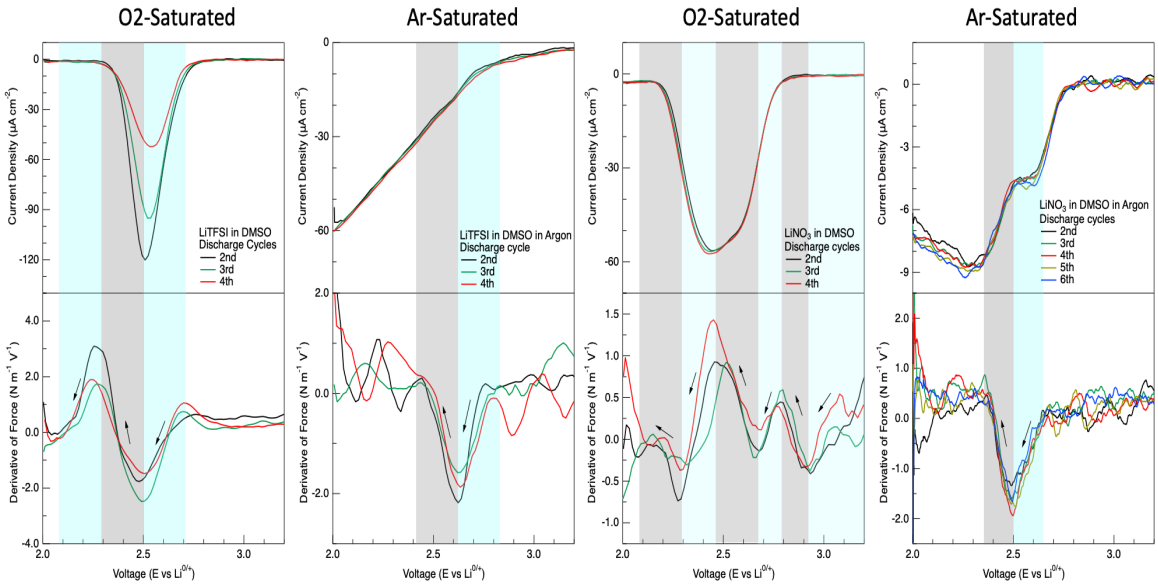

Figure 27: The current response and the first derivative of the force with respect to the applied potential during the 2-4 discharge cycles on the Au cathode cycled in an oxygen-saturated electrolyte (A and C) and an argon-saturated electrolyte (B and D) of 1 M LiTFSI in DMSO (A and B) and 1 M $LiNO_3$ in DMSO (C and D). Cyclic Voltammetry was conducted from 2-4.1 V at 1 mV/s for LiTFSI in DMSO (A and B) and from 2-4.4 V for 1 M $LiNO_3$ in DMSO (C and D).

During this period, the corresponding current evolution is almost zero, indicating that these changes are non-faradaic reactions. Similar to the LiTFSI in DMSO oxygen-saturated electrolyte, the stress derivative becomes more negative at the onset of the current decay around 2.8 V in the $LiNO_3$ oxygen-saturated electrolyte. During the current decay, the stress derivative changes its direction from a negative change in the stress derivative to a positive change. Once the current reaches the its minimum value, the stress derivative reaches its local maxima. This is the opposite to what is observed for LiTFSI in DMSO oxygen-saturated electrolyte.

As discussed in the introduction (Chapter I, section 1.5.6) lithium peroxide can form via a solution or a surface-based mechanism. In either case, oxygen needs to be reduced on the electrode surface to form a negatively charged oxygen species, which requires a one-electron transfer reaction that takes place on the electrode surface. Also, the positively charged lithium ions need to be transferred onto the electrode surface to enable the oxygen reduction reaction. Then, an electrochemical reaction between the positively charged lithium ions and the negatively charged oxygen species lead to the formation of lithium superoxide, LiO_2. These initial reactions are similar in both the surface and solution-based mechanisms.

If the lithium superoxide further oxidizes to form lithium peroxide on the electrode surface, the morphology of the lithium peroxide will be a thin film. The second possibility is the formation of lithium peroxide via a chemical reaction involving the chemical decomposition of lithium superoxide. This also generates oxygen gas as a side product. This solution-based reaction takes place when lithium superoxide dissolves in the electrolyte and decomposes to form lithium superoxide, which forms a toroidal lithium peroxide species. Figure 26 shows that in the early stages of the current decay in the oxygen-saturated electrolytes (between 2.8 – 2.6 V), the stress evolution transitions into a compressive regime. This could be associated with the generation of charged oxygen species. Later, the stress evolves into the tensile regime in both salts. However, the generation of tensile stress continues in the LiTFSI in DMSO oxygen-saturated electrolyte until current becomes almost zero at around 2.3 V. The stress becomes more tensile between 2.7 to 2.6 V in the $LiNO_3$ oxygen-saturated electrolyte. Then, the stress becomes compressive again until it transitions back into the tensile regime at 2.44 V which coincides with the current decay. These additional steps in the $LiNO_3$ oxygen-saturated electrolyte suggests competing reactions between the dissolution of the reaction intermediate and the formation of new reaction intermediates on the surface of the electrode. Also, the magnitude of the stress is much smaller in the $LiNO_3$ oxygen-

saturated electrolyte, indicating that the Au surface is less strained due to the formation of less surface-driven thin film formation.

4.3.2 Stress Development during Charging

Figure 28 represents the charging behavior of the oxygen-saturated $LiNO_3$ and LiTFSI in DMSO electrolytes. A single current peak is observed at around 3.9 V in the $LiNO_3$ oxygen-saturated electrolyte, indicating the oxidation of the lithium peroxide. The current increase is almost negligible in the LiTFSI-containing electrolyte, which suggests that an insulating thin film of

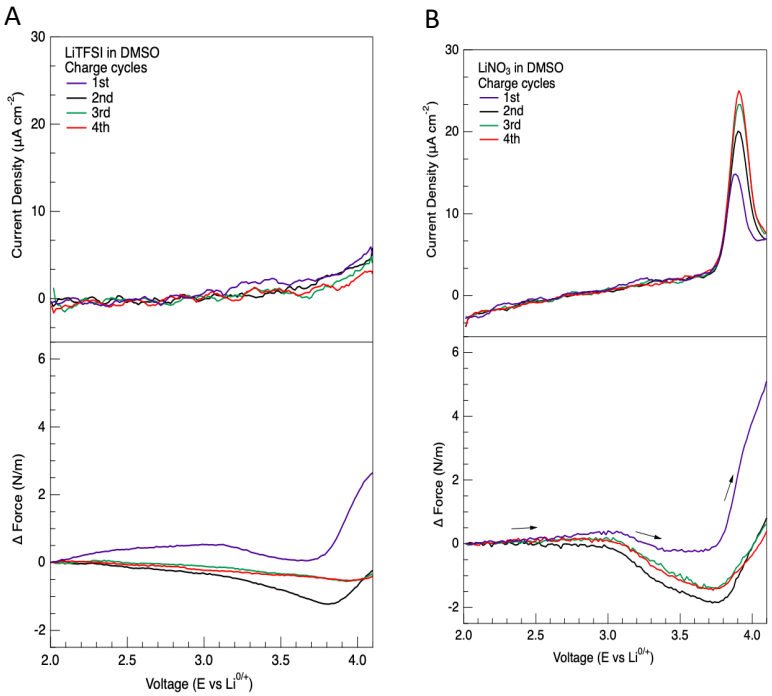

Figure 28: The current response and force development during charge cycles 1-4 on the Au cathode cycled in an oxygen-saturated 1 M LiTFSI in DMSO (A) and 1 M $LiNO_3$ in DMSO (B) electrolyte. Cyclic Voltammetry was conducted from 2-4.1 V at 1 mV/s for LiTFSI in DMSO (A) and from 2-4.4 V for 1 M $LiNO_3$ in DMSO (B). The force was set to zero at the onset of each charge cycle for Figures A and B.

lithium peroxide is formed during discharge and there is no significant oxidation reaction during charge. The stress generation in the electrode during charging shows irreversible behavior with the cycle number in the LiTFSI in the oxygen-saturated electrolyte. In the first cycle, there is a compressive stress generation at around 3.2 V, followed by tensile stress generation around 3.7 V.

In the third and fourth cycles, there is almost no stress generation during the charging, yet the stress generation is more reversible with cycle number in the $LiNO_3$ oxygen-saturated electrolyte. The stress becomes compressive at around 3.0 V and then stress becomes more tensile at 3.8 V.

In order to better understand the charge mechanism, stress measurements were also conducted using argon-saturated electrolytes (Figure 29). There is a linear increase in the current response in the argon-saturated LiTFSI in DMSO electrolyte.

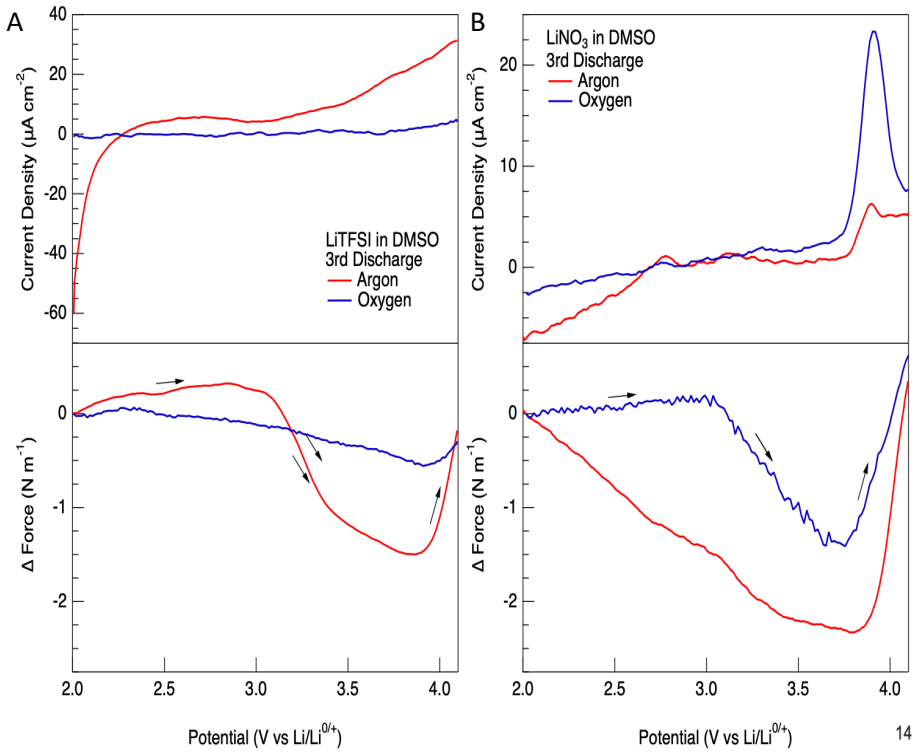

Figure 29: The current response and the force development during charge cycles 1-4 on the Au cathode cycled in 1 M LiTFSI in DMSO (A) and 1 M $LiNO_3$ in DMSO (B). Cyclic Voltammetry was conducted from 2-4.1 V at 1 mV/s for LiTFSI in DMSO (A) and from 2-4.4 V for 1 M $LiNO_3$ in DMSO (B) at the same scan rate. The force was set to zero at the onset of each charge cycle for Figures A and B.

This indicates that when the electrode was discharged in the oxygen-saturated LiTFSI in DMSO electrolyte, the discharge products were mostly thin film lithium peroxide. The stress development in the argon-saturated LiTFSI in DMSO electrolyte is highly reversible with cycle number. There is a compressive stress development at around 3.2 V, followed by a tensile stress generation around

3.8 V. In the case of the $LiNO_3$ salt system, the stress is compressive again until 3.8 V where it becomes tensile at higher voltages. Previously, Aurbach et al. suggested the adsorption of the NO_2 and formation of negatively charged NO_2^- species on the surface of the electrode during charge cycles[96]. The stress generation in the argon-saturated electrolyte indicates the adsorption of salt species on the surface of the electrode. The charge mechanism depends on the electrolyte salt as well as the morphology of the lithium peroxide formed during the oxygen reduction reaction. If the discharge product is a thin film, it insulates the surface of the electrode and can prevent the oxygen evolution reaction from taking place during charge cycle. If the discharge product is toroidal, it becomes difficult to oxidize the lithium peroxide without a redox mediator.

Our study demonstrates that when the discharge product is a thin film in the LiTFSI oxygen-saturated electrolyte, the charge process is hindered by disabling the adsorption process of the salt species, which is critical to the decomposition of lithium peroxide. When the lithium peroxide morphology is toroidal in the $LiNO_3$ salt, the $LiNO_3$ salt acts as a redox mediator, which makes it easier to oxidize the lithium peroxide. In the $LiNO_3$ electrolyte, this can be accomplished by a shuttling redox reaction of the NO_2 / NO_2^- on the electrode surface. Based on experiments conducted in the oxygen versus argon-saturated electrolytes, the large compressive stress is associated with the adsorption of the salt species and tensile stress generates when the lithium peroxide is oxidized.

4.4. Conclusions

Both the electrochemical and the mechanical behavior of the salt species on the Au cathode were investigated. Experiments were conducted in both oxygen and argon-saturated electrolytes to differentiate the stress evolution of the products evolved during the oxygen evolution/reductions reactions from those evolved in an argon environment. During the discharge reaction, both the $LiNO_3$ and LiTFSI salts exhibited a compressive stress generation at the onset of the potential that Li_2O_2 formation was expected. The $LiNO_3$ salt had multiple peaks in the stress evolution during

discharging, which suggests that multiple surface reactions were taking place on the Au cathode surface. The solution-based discharge mechanism results is more complex due to the migration of the LiO_2 intermediate from the Au surface into the electrolyte solution. The solution-based mechanism is likely the dominant reaction pathway for the formation of Li_2O_2 in the $LiNO_3$ salt.

During charging, irreversible mechanical behaviors and very minimal current responses were recorded for the LiTFSI salt. This high degree of reversibility likely indicates the formation of passivating thin films of Li_2O_2 that have accumulated on the surface due to a surface-based discharge mechanism. Due to the low current response, the oxidation reaction leading to Li_2O_2 decomposition likely did not occur. This would lead to the passivation of the cathode, which is seen in the minimal stress evolution response in the third and fourth charging cycles. The argon-saturated electrolytes demonstrated tensile stress generation The stress was compressive when using the $LiNO_3$ salt until 3.8 V, where it become largely tensile. The contrast between the $LiNO_3$ and LiTFSI salts during both charge and discharge were identified by probing the surface mechanisms via curvature measurements. The outcome of this paper presents a novel perspective about the catalytic activity of the salt species and the formation mechanisms of the lithium peroxide discharge product in Li-O_2 batteries.

CHAPTER V

FUTURE WORK

5.1 Future Work

As mentioned previously, the primary bottleneck hindering the commercialization of Li-O_2 batteries is the cathode electrode. Both the cycle life of the cell and the capacity are both dependent on the stability of the cathode. Due to the issues relating to cathode stability discussed in Chapter I, the stress measurements could also be conducted using different cathode materials such as Pt and Pd. These cathode materials act as catalysts that can improve the reaction kinetics occurring during the oxygen evolution reaction[194]. Both the stress response and the electrochemical data can be compared to that of the Au that was used in previous experiments.

Another primary issue that is observed in Li-O_2 batteries are the sluggish reaction kinetics occurring during both the oxygen reduction and the oxygen evolution reactions. The slow reaction kinetics can lead to irreversible cycling behavior and a rapid capacity fade. Factors that affect the reaction kinetics are the electrolyte, the cathode material, and the cycling conditions. The morphology of the Li_2O_2 that is deposited also affects the reaction kinetics occurring during both OER and ORR. By analyzing the stress evolution during cycling, the changes in the electrochemical behavior can be correlated to the surface reactions occurring on the cathode. As seen previously

with the 1 M LiTFSI in DMSO, irreversible behavior can be easily seen in the observed stress evolution over time.

Although analyzing the stress evolution in Li-O_2 batteries was conducted for the first time, it would also be interesting to analyze the stress evolution occurring in Na-O_2 batteries. Na-O_2 batteries differ from Li-O_2 batteries in two primary ways. The first is the much lower overpotential that has been observed between the discharge and charging cycles, and the second is the driving electrochemical reaction that occurs[195]. The primary discharge product in Na-O_2 batteries is sodium superoxide, NaO_2. The formation of NaO_2 is favored over the formation of Na_2O_2 [195,196].This is different from the Li-O_2 battery which forms LiO_2 as a reaction intermediate that is unstable. Determining the differences in the stress evolution between these two metal-oxygen batteries would be interesting and could give more insight into the stress evolution that the NaO_2 product has on the cathode as compared to Li_2O_2.

REFERENCES

(1) Administration, U. S. E. I. *International Energy Outlook 2019*; 2020.

(2) International Energy Agency. Global Energy Review 2021.

(3) Thackeray, M. M.; Wolverton, C.; Isaacs, E. D. Electrical Energy Storage for Transportation - Approaching the Limits of, and Going beyond, Lithium-Ion Batteries. *Energy Environ. Sci.* **2012**, *5* (7), 7854–7863. https://doi.org/10.1039/c2ee21892e.

(4) Akira Yoshino, Kenichi Sanechika, T. N. Japanese Patent 1989293, 1985.

(5) Dunn, B.; Kamath, H.; Tarascon, J. M. Electrical Energy Storage for the Grid: A Battery of Choices. *Science (80-.).* **2011**, *334* (6058), 928–935. https://doi.org/10.1126/science.1212741.

(6) Harb, T. F. F. and J. N. *Electrochemical Engineering*, First.; John Wiley and Sons Ltd, 2018.

(7) Islam, M. S.; Davies, R. A.; Gale, J. D. LiNi0.5Mn0. 5O2 Lithium Battery Material. *Chem. Mater.* **2003**, *15* (c), 4280–4286.

(8) Goodenough, J. B.; Kim, Y. Challenges for Rechargeable Li Batteries. *Chem. Mater.* **2010**, *22* (3), 587–603. https://doi.org/10.1021/cm901452z.

(9) Zaghib, K.; Guerfi, A.; Hovington, P.; Vijh, A.; Trudeau, M.; Mauger, A.; Goodenough, J. B.; Julien, C. M. Review and Analysis of Nanostructured Olivine-Based Lithium Recheargeable Batteries: Status and Trends. *J. Power Sources* **2013**, *232*, 357–369. https://doi.org/10.1016/j.jpowsour.2012.12.095.

(10) Huang, Y. H.; Goodenough, J. B. High-Rate LiFePO4 Lithium Rechargeable Battery Promoted by Electrochemically Active Polymers. *Chem. Mater.* **2008**, *20* (23), 7237–7241. https://doi.org/10.1021/cm8012304.

(11) Yu, Y.; Guo, J.; Xiang, M.; Su, C.; Liu, X.; Bai, H.; Bai, W.; Duan, K. Enhancing the Durable Performance of LiMn2O4 at High-Rate and Elevated Temperature by Nickel-Magnesium Dual Doping. *Sci. Rep.* **2019**, *9* (1), 1–9. https://doi.org/10.1038/s41598-019-53494-7.

(12) Manthiram, A. A Reflection on Lithium-Ion Battery Cathode Chemistry. *Nat. Commun.* **2020**, *11* (1), 1–9. https://doi.org/10.1038/s41467-020-15355-0.

(13) Aurbach, D.; McCloskey, B. D.; Nazar, L. F.; Bruce, P. G. Advances in Understanding Mechanisms Underpinning Lithium-Air Batteries. *Nat. Energy* **2016**, *1* (9), 1–11. https://doi.org/10.1038/nenergy.2016.128.

(14) Bruce, P. G.; Freunberger, S. A.; Hardwick, L. J.; Tarascon, J. M. Li-O2 and Li-S Batteries with High Energy Storage. *Nat. Mater.* **2012**, *11* (1), 19–29. https://doi.org/10.1038/nmat3191.

(15) Abraham, K. M.; Jiang, Z. ELECTROCHEMICAL SCIENCE AND TECHNOLOGY A Polymer Electrolyte-Based Rechargeable Lithium / Oxygen Battery. *J. Electrochem. Soc.* **1996**, *143* (1), 1–5.

(16) Abraham, K. M. ECS Meeting Abstracts A Two-Dimensional Modeling of a Lithium-Polymer Battery. **2006**.

(17) Laoire, C. O.; Mukerjee, S.; Abraham, K. M.; Plichta, E. J.; Hendrickson, M. A. Elucidating the Mechanism of Oxygen Reduction for Lithium-Air Battery Applications. *J. Phys. Chem. C* **2009**, *113* (46), 20127–20134. https://doi.org/10.1021/jp908090s.

(18) Laoire, C. O.; Mukerjee, S.; Abraham, K. M.; Plichta, E. J.; Hendrickson, M. A. Influence of Nonaqueous Solvents on the Electrochemistry of Oxygen in the Rechargeable Lithium-Air Battery. *J. Phys. Chem. C* **2010**, *114* (19), 9178–9186. https://doi.org/10.1021/jp102019y.

(19) Read, J. Characterization of the Lithium/Oxygen Organic Electrolyte Battery. *J. Electrochem. Soc.* **2002**, *149* (9), A1190. https://doi.org/10.1149/1.1498256.

(20) Read, J.; Mutolo, K.; Ervin, M.; Behl, W.; Wolfenstine, J.; Driedger, A.; Foster, D. Oxygen Transport Properties of Organic Electrolytes and Performance of Lithium/Oxygen Battery. *J. Electrochem. Soc.* **2003**, *150* (10), A1351. https://doi.org/10.1149/1.1606454.

(21) Read, J. Ether-Based Electrolytes for the Lithium/Oxygen Organic Electrolyte Battery. *J. Electrochem. Soc.* **2006**, *153* (1), A96. https://doi.org/10.1149/1.2131827.

(22) Ottakam Thotiyl, M. M.; Freunberger, S. A.; Peng, Z.; Bruce, P. G. The Carbon Electrode in Nonaqueous Li-O2 Cells. *J. Am. Chem. Soc.* **2013**, *135* (1), 494–500. https://doi.org/10.1021/ja310258x.

(23) Gao, X.; Chen, Y.; Johnson, L. R.; Jovanov, Z. P.; Bruce, P. G. A Rechargeable Lithium–Oxygen Battery with Dual Mediators Stabilizing the Carbon Cathode. *Nat. Energy* **2017**, *2* (July), 1–7. https://doi.org/10.1038/nenergy.2017.118.

(24) Kwak, W. J.; Rosy; Sharon, D.; Xia, C.; Kim, H.; Johnson, L. R.; Bruce, P. G.; Nazar, L. F.; Sun, Y. K.; Frimer, A. A.; Noked, M.; Freunberger, S. A.; Aurbach, D. Lithium-Oxygen Batteries and Related Systems: Potential, Status, and Future. *ACS Appl. Mater. Interfaces* **2020**. https://doi.org/10.1021/acs.chemrev.9b00609.

(25) Bergner, B. J.; Busche, M. R.; Pinedo, R.; Berkes, B. B.; Schröder, D.; Janek, J. How to Improve Capacity and Cycling Stability for Next Generation Li-O2 Batteries: Approach with a Solid Electrolyte and Elevated Redox Mediator Concentrations. *ACS Appl. Mater. Interfaces* **2016**, *8* (12), 7756–7765. https://doi.org/10.1021/acsami.5b10979.

(26) Han, X.; Ouyang, M.; Lu, L.; Li, J. Cycle Life of Commercial Lithium-Ion Batteries with Lithium Titanium Oxide Anodes in Electric Vehicles. *Energies* **2014**, *7* (8), 4895–4909. https://doi.org/10.3390/en7084895.

(27) Bard, Allen, Faulkner, L. *Electrochemical Methods: Fundamentals and Applications*, Second.; Wiley, 2001.

(28) Lu, Y. C.; Gasteiger, H. A.; Parent, M. C.; Chiloyan, V.; Shao-Horn, Y. The Influence of Catalysts on Discharge and Charge Voltages of Rechargeable Li-Oxygen Batteries. *Electrochem. Solid-State Lett.* **2010**, *13* (6), 3–4. https://doi.org/10.1149/1.3363047.

(29) Peng, Z.; Freunberger, S. A.; Hardwick, L. J.; Chen, Y.; Giordani, V.; Bardé, F.; Novák, P.; Graham, D.; Tarascon, J. M.; Bruce, P. G. Oxygen Reactions in a Non-Aqueous Li+ Electrolyte. *Angew. Chemie - Int. Ed.* **2011**, *50* (28), 6351–6355. https://doi.org/10.1002/anie.201100879.

(30) Kwak, W.-J.; Rosy; Sharon, D.; Xia, C.; Kim, H.; Johnson, L. R.; Bruce, P. G.; Nazar, L. F.; Sun, Y.-K.; Frimer, A. A.; Noked, M.; Freunberger, S. A.; Aurbach, D. Lithium–Oxygen Batteries and Related Systems: Potential, Status, and Future. *Chem. Rev.* **2020**, *120* (14), 6626–6683. https://doi.org/10.1021/acs.chemrev.9b00609.

(31) Lyu, Z.; Zhou, Y.; Dai, W.; Cui, X.; Lai, M.; Wang, L.; Huo, F.; Huang, W.; Hu, Z.; Chen, W. Recent Advances in Understanding of the Mechanism and Control of Li2O2 Formation in Aprotic Li-O2 Batteries. *Chem. Soc. Rev.* **2017**, *46* (19), 6046–6072. https://doi.org/10.1039/c7cs00255f.

(32) Black, R.; Adams, B.; Nazar, L. F. Non-Aqueous and Hybrid Li-O 2 Batteries. *Adv. Energy Mater.* **2012**, *2* (7), 801–815. https://doi.org/10.1002/aenm.201200001.

(33) Zhang, S. S.; Foster, D.; Read, J. Discharge Characteristic of a Non-Aqueous Electrolyte Li/O2 Battery. *J. Power Sources* **2010**, *195* (4), 1235–1240. https://doi.org/10.1016/j.jpowsour.2009.08.088.

(34) Tan, P.; Jiang, H. R.; Zhu, X. B.; An, L.; Jung, C. Y.; Wu, M. C.; Shi, L.; Shyy, W.; Zhao, T. S. Advances and Challenges in Lithium-Air Batteries. *Appl. Energy* **2017**, *204*, 780–806. https://doi.org/10.1016/j.apenergy.2017.07.054.

(35) Visco, S.; Nimon, E.; Katz, B.; Chu, M.-Y.; De Jonghe, L. Lithium/Air Semi-Fuel Cells: High Energy Density Batteries Based on Lithium Metal Electrodes. In *12th international meeting on lithium batteries*; 2004.

(36) Zhang, T.; Imanishi, N.; Takeda, Y.; Yamamoto, O. Aqueous Lithium/Air Rechargeable Batteries. *Chem. Lett.* **2011**, *40* (7), 668–673. https://doi.org/10.1246/cl.2011.668.

(37) Zhang, T.; Imanishi, N.; Shimonishi, Y.; Hirano, A.; Takeda, Y.; Yamamoto, O.; Sammes, N. A Novel High Energy Density Rechargeable Lithium/Air Battery. *Chem. Commun.* **2010**, *46* (10), 1661–1663. https://doi.org/10.1039/b920012f.

(38) Zhang, T.; Liu, S.; Imanishi, N.; Hirano, A.; Takeda, Y.; Yamamoto, O. Water-Stable Lithium Electrode and Its Application in Aqueous Lithium/Air Secondary Batteries. *Electrochemistry* **2010**, *16* (3).

(39) Wang, Y.; Zhou, H. A Lithium-Air Battery with a Potential to Continuously Reduce O2 from Air for Delivering Energy. *J. Power Sources* **2010**, *195* (1), 358–361. https://doi.org/10.1016/j.jpowsour.2009.06.109.

(40) Visco, S.; Katz, B.; Nimon, Y.; De Jonghe, L. Protected Active Metal Electrode and Battery Cell Structures with Non-Aqueous Interlayer Architecture. 7,282,295, 2007.

(41) He, P.; Wang, Y.; Zhou, H. A Li-Air Fuel Cell with Recycle Aqueous Electrolyte for Improved Stability. *Electrochem. commun.* **2010**, *12* (12), 1686–1689. https://doi.org/10.1016/j.elecom.2010.09.025.

(42) Kumar, B.; Kumar, J. Cathodes for Solid-State Lithium–Oxygen Cells: Roles of Nasicon Glass-Ceramics. *J. Electrochem. Soc.* **2010**, *157* (5), A611. https://doi.org/10.1149/1.3356988.

(43) Sun, Y. Lithium Ion Conducting Membranes for Lithium-Air Batteries. *Nano Energy* **2013**, *2* (5), 801–816. https://doi.org/10.1016/j.nanoen.2013.02.003.

(44) Luntz, A. C.; Mccloskey, B. D. Nonaqueous Li−Air Batteries: A Status Report. **2014**.

(45) Zhang, Y.; Zhang, H.; Li, J.; Wang, M.; Nie, H.; Zhang, F. The Use of Mixed Carbon Materials with Improved Oxygen Transport in a Lithium-Air Battery. *J. Power Sources* **2013**, *240*, 390–396. https://doi.org/10.1016/j.jpowsour.2013.04.018.

(46) Park, C. K.; Park, S. B.; Lee, S. Y.; Lee, H.; Jang, H.; Cho, W. I. Electrochemical Performances of Lithium-Air Cell with Carbon Materials. *Bull. Korean Chem. Soc.* **2010**, *31* (11), 3221–3224. https://doi.org/10.5012/bkcs.2010.31.11.3221.

(47) Şener, T.; Kayhan, E.; Sevim, M.; Metin, Ö. Monodisperse CoFe2O4 Nanoparticles Supported on Vulcan XC-72: High Performance Electrode Materials for Lithium-Air and Lithium-Ion Batteries. *J. Power Sources* **2015**, *288*, 36–41. https://doi.org/10.1016/j.jpowsour.2015.04.120.

(48) Lu, Y. C.; Gasteiger, H. A.; Parent, M. C.; Chiloyan, V.; Shao-Horn, Y. The Influence of Catalysts on Discharge and Charge Voltages of Rechargeable Li-Oxygen Batteries. *Electrochem. Solid-State Lett.* **2010**, *13* (6). https://doi.org/10.1149/1.3363047.

(49) Ma, Z.; Yuan, X.; Li, L.; Ma, Z. F.; Wilkinson, D. P.; Zhang, L.; Zhang, J. A Review of Cathode Materials and Structures for Rechargeable Lithium-Air Batteries. *Energy Environ. Sci.* **2015**, *8* (8), 2144–2198. https://doi.org/10.1039/c5ee00838g.

(50) Cui, Y.; Wen, Z.; Liang, X.; Lu, Y.; Jin, J.; Wu, M.; Wu, X. A Tubular Polypyrrole Based Air Electrode with Improved O2 Diffusivity for Li-O2 Batteries. *Energy Environ. Sci.* **2012**, *5* (7), 7893–7897. https://doi.org/10.1039/c2ee21638h.

(51) Johnson, L.; Li, C.; Liu, Z.; Chen, Y.; Freunberger, S. A.; Ashok, P. C.; Praveen, B. B.; Dholakia, K.; Tarascon, J. M.; Bruce, P. G. The Role of LiO2 Solubility in O2 Reduction in Aprotic Solvents and Its Consequences for Li-O 2 Batteries. *Nat. Chem.* **2014**, *6* (12), 1091–1099. https://doi.org/10.1038/nchem.2101.

(52) Viswanathan, V.; Thygesen, K. S.; Hummelshj, J. S.; Nrskov, J. K.; Girishkumar, G.; McCloskey, B. D.; Luntz, A. C. Electrical Conductivity in Li 2O 2 and Its Role in Determining Capacity Limitations in Non-Aqueous Li-O 2 Batteries. *J. Chem. Phys.* **2011**, *135* (21). https://doi.org/10.1063/1.3663385.

(53) Albertus, P.; Girishkumar, G.; McCloskey, B.; Sánchez-Carrera, R. S.; Kozinsky, B.; Christensen, J.; Luntz, A. C. Identifying Capacity Limitations in the Li/Oxygen Battery Using Experiments and Modeling. *J. Electrochem. Soc.* **2011**, *158* (3), A343. https://doi.org/10.1149/1.3527055.

(54) Peng, Z.; Freunberger, S. A.; Chen, Y.; Bruce, P. G. A Reversible and Higher-Rate Li-O2 Battery. *Science (80-.).* **2012**, *337* (6094), 563–566. https://doi.org/10.1126/science.1223985.

(55) Gittleson, F. S.; Ryu, W. H.; Taylor, A. D. Operando Observation of the Gold-Electrolyte Interface in Li-O2 Batteries. *ACS Appl. Mater. Interfaces* **2014**, *6* (21), 19017–19025. https://doi.org/10.1021/am504900k.

(56) Sharon, D.; Hirsberg, D.; Salama, M.; Afri, M.; Frimer, A. A.; Noked, M.; Kwak, W.; Sun, Y. K.; Aurbach, D. Mechanistic Role of Li+ Dissociation Level in Aprotic Li-O2 Battery. *ACS Appl. Mater. Interfaces* **2016**, *8* (8), 5300–5307. https://doi.org/10.1021/acsami.5b11483.

(57) Stamenkovic, V.; Mun, B. S.; Mayrhofer, K. J. J.; Ross, P. N.; Markovic, N. M.; Rossmeisl, J.; Greeley, J.; Nørskov, J. K. Changing the Activity of Electrocatalysts for Oxygen Reduction by Tuning the Surface Electronic Structure. *Angew. Chemie - Int. Ed.* **2006**, *45* (18), 2897–2901. https://doi.org/10.1002/anie.200504386.

(58) Greeley, J.; Stephens, I. E. L.; Bondarenko, A. S.; Johansson, T. P.; Hansen, H. A.; Jaramillo, T. F.; Rossmeisl, J.; Chorkendorff, I.; Nørskov, J. K. Alloys of Platinum and Early Transition Metals as Oxygen Reduction Electrocatalysts. *Nat. Chem.* **2009**, *1* (7), 552–556. https://doi.org/10.1038/nchem.367.

(59) Lyu, Z.; Yang, L.; Luan, Y.; Renshaw Wang, X.; Wang, L.; Hu, Z.; Lu, J.; Xiao, S.; Zhang, F.; Wang, X.; Huo, F.; Huang, W.; Hu, Z.; Chen, W. Effect of Oxygen Adsorbability on the Control of Li2O2 Growth in Li-O2 Batteries: Implications for Cathode Catalyst Design. *Nano Energy* **2017**, *36* (April), 68–75. https://doi.org/10.1016/j.nanoen.2017.04.022.

(60) Zhu, J.; Ren, X.; Liu, J.; Zhang, W.; Wen, Z. Unraveling the Catalytic Mechanism of Co<inf>3</Inf>O<inf>4</Inf> for the Oxygen Evolution Reaction in a Li-O<inf>2</Inf> Battery. *ACS Catal.* **2015**, *5* (1), 73–81. https://doi.org/10.1021/cs5014442.

(61) Hou, C.; Han, J.; Liu, P.; Yang, C.; Huang, G.; Fujita, T.; Hirata, A.; Chen, M. Operando Observations of RuO2 Catalyzed Li2O2 Formation and Decomposition in a Li-O2 Micro-Battery. *Nano Energy* **2018**, *47* (January), 427–433. https://doi.org/10.1016/j.nanoen.2018.02.057.

(62) Shi, L.; Zhao, T.; Xu, A.; Wei, Z. Unraveling the Catalytic Mechanism of Rutile RuO2 for the Oxygen Reduction Reaction and Oxygen Evolution Reaction in Li-O2 Batteries. *ACS Catal.* **2016**, *6* (9), 6285–6293. https://doi.org/10.1021/acscatal.6b01778.

(63) Lim, H. D.; Lee, B.; Zheng, Y.; Hong, J.; Kim, J.; Gwon, H.; Ko, Y.; Lee, M.; Cho, K.; Kang, K. Rational Design of Redox Mediators for Advanced Li-O2 Batteries. *Nat. Energy* **2016**, *1* (6). https://doi.org/10.1038/nenergy.2016.66.

(64) Kwak, W. J.; Hirshberg, D.; Sharon, D.; Afri, M.; Frimer, A. A.; Jung, H. G.; Aurbach, D.; Sun, Y. K. Li-O2 Cells with LiBr as an Electrolyte and a Redox Mediator. *Energy Environ. Sci.* **2016**, *9* (7), 2334–2345. https://doi.org/10.1039/c6ee00700g.

(65) Nakanishi, A.; Thomas, M. L.; Kwon, H. M.; Kobayashi, Y.; Tatara, R.; Ueno, K.; Dokko, K.; Watanabe, M. Electrolyte Composition in Li/O2 Batteries with LiI Redox Mediators: Solvation Effects on Redox Potentials and Implications for Redox Shuttling. *J. Phys. Chem. C* **2018**, *122* (3), 1522–1534. https://doi.org/10.1021/acs.jpcc.7b11859.

(66) Mizuno, F.; Nakanishi, S.; Kotani, Y.; Yokoishi, S.; Iba, H. Rechargeable Li-Air Batteries with Carbonate-Based Liquid Electrolytes. *Electrochemistry* **2010**, *78* (5), 403–405.

(67) Xiao, J.; Hu, J.; Wang, D.; Hu, D.; Xu, W.; Graff, G. L.; Nie, Z.; Liu, J.; Zhang, J. G. Investigation of the Rechargeability of Li-O2 Batteries in Non-Aqueous Electrolyte. *J. Power Sources* **2011**, *196* (13), 5674–5678. https://doi.org/10.1016/j.jpowsour.2011.02.060.

(68) Xu, J. J.; Chang, Z. W.; Wang, Y.; Liu, D. P.; Zhang, Y.; Zhang, X. B. Cathode Surface-Induced, Solvation-Mediated, Micrometer-Sized Li2O2 Cycling for Li–O2 Batteries. *Adv. Mater.* **2016**, *28* (43), 9620–9628. https://doi.org/10.1002/adma.201603454.

(69) McCloskey, B. D.; Bethune, D. S.; Shelby, R. M.; Girishkumar, G.; Luntz, A. C. Solvents Critical Role in Nonaqueous Lithium-Oxygen Battery Electrochemistry. *J. Phys. Chem. Lett.* **2011**, *2* (10), 1161–1166. https://doi.org/10.1021/jz200352v.

(70) Freunberger, S. A.; Chen, Y.; Peng, Z.; Griffin, J. M.; Hardwick, L. J.; Bardé, F.; Novák, P.; Bruce, P. G. Reactions in the Rechargeable Lithium-O2 Battery with Alkyl Carbonate Electrolytes. *J. Am. Chem. Soc.* **2011**, *133* (20), 8040–8047. https://doi.org/10.1021/ja2021747.

(71) Gallant, B. M.; Mitchell, R. R.; Kwabi, D. G.; Zhou, J.; Zuin, L.; Thompson, C. V. Chemical and Morphological Changes of Li-O2 Battery Electrodes upon Cycling. **2012**.

(72) McCloskey, B. D.; Speidel, A.; Scheffler, R.; Miller, D. C.; Viswanathan, V.; Hummelshøj, J. S.; Nørskov, J. K.; Luntz, A. C. Twin Problems of Interfacial Carbonate Formation in Nonaqueous Li-O 2 Batteries. *J. Phys. Chem. Lett.* **2012**, *3* (8), 997–1001. https://doi.org/10.1021/jz300243r.

(73) Bryantsev, V. S.; Giordani, V.; Walker, W.; Blanco, M.; Zecevic, S.; Sasaki, K.; Uddin, J.; Addison, D.; Chase, G. V. Predicting Solvent Stability in Aprotic Electrolyte Li-Air Batteries: Nucleophilic Substitution by the Superoxide Anion Radical (O2•-). *J. Phys. Chem. A* **2011**, *115* (44), 12399–12409. https://doi.org/10.1021/jp2073914.

(74) Freunberger, S. A.; Chen, Y.; Drewett, N. E.; Hardwick, L. J.; Bardé, F.; Bruce, P. G. The Lithium-Oxygen Battery with Ether-Based Electrolytes. *Angew. Chemie - Int. Ed.* **2011**, *50* (37), 8609–8613. https://doi.org/10.1002/anie.201102357.

(75) Wang, Y.; Lai, N. C.; Lu, Y. R.; Zhou, Y.; Dong, C. L.; Lu, Y. C. A Solvent-Controlled Oxidation Mechanism of Li2O2 in Lithium-Oxygen Batteries. *Joule* **2018**, *2* (11), 2364–2380. https://doi.org/10.1016/j.joule.2018.07.021.

(76) Bryantsev, V. S.; Blanco, M. Decomposition of Organic Carbonate-Based Electrolytes. **2011**, 379–383.

(77) Bryantsev, V. S.; Faglioni, F. Predicting Autoxidation Stability of Ether- and Amide-Based Electrolyte Solvents for Li-Air Batteries. *J. Phys. Chem. A* **2012**, *116* (26), 7128–7138. https://doi.org/10.1021/jp301537w.

(78) Lu, Y. C.; Gallant, B. M.; Kwabi, D. G.; Harding, J. R.; Mitchell, R. R.; Whittingham, M. S.; Shao-Horn, Y. Lithium-Oxygen Batteries: Bridging Mechanistic Understanding and Battery Performance. *Energy Environ. Sci.* **2013**, *6* (3), 750–768. https://doi.org/10.1039/c3ee23966g.

(79) Wandt, J.; Jakes, P.; Granwehr, J.; Gasteiger, H. A.; Eichel, R. A. Singlet Oxygen Formation during the Charging Process of an Aprotic Lithium-Oxygen Battery. *Angew. Chemie - Int. Ed.* **2016**, *55* (24), 6892–6895. https://doi.org/10.1002/anie.201602142.

(80) Mahne, N.; Schafzahl, B.; Leypold, C.; Leypold, M.; Grumm, S.; Leitgeb, A.; Strohmeier, G. A.; Wilkening, M.; Fontaine, O.; Kramer, D.; Slugovc, C.; Borisov, S. M.; Freunberger, S. A. Singlet Oxygen Generation as a Major Cause for Parasitic Reactions during Cycling of Aprotic Lithium-Oxygen Batteries. *Nat. Energy* **2017**, *2* (5), 1–9. https://doi.org/10.1038/nenergy.2017.36.

(81) McCloskey, B. D.; Scheffler, R.; Speidel, A.; Girishkumar, G.; Luntz, A. C. On the Mechanism of Nonaqueous Li-O2 Electrochemistry on C and Its Kinetic Overpotentials: Some Implications for Li-Air Batteries. *J. Phys. Chem. C* **2012**, *116* (45), 23897–23905. https://doi.org/10.1021/jp306680f.

(82) Aetukuri, N. B.; McCloskey, B. D.; Garciá, J. M.; Krupp, L. E.; Viswanathan, V.; Luntz, A. C. Solvating Additives Drive Solution-Mediated Electrochemistry and Enhance Toroid Growth in Non-Aqueous Li-O2 Batteries. *Nat. Chem.* **2015**, *7* (1), 50–56. https://doi.org/10.1038/nchem.2132.

(83) Lim, H. D.; Lee, B.; Bae, Y.; Park, H.; Ko, Y.; Kim, H.; Kim, J.; Kang, K. Reaction Chemistry in Rechargeable Li-O2 Batteries. *Chem. Soc. Rev.* **2017**, *46* (10), 2873–2888. https://doi.org/10.1039/c6cs00929h.

(84) Recommendations, I. Disproportionation. *IUPAC Compend. Chem. Terminol.* **2008**. https://doi.org/10.1351/goldbook.d01799.

(85) Mitchell, R. R.; Gallant, B. M.; Thompson, C. V.; Shao-Horn, Y. All-Carbon-Nanofiber Electrodes for High-Energy Rechargeable Li-O 2 Batteries. *Energy Environ. Sci.* **2011**, *4* (8), 2952–2958. https://doi.org/10.1039/c1ee01496j.

(86) Black, R.; Oh, S. H.; Lee, J. H.; Yim, T.; Adams, B.; Nazar, L. F. Screening for Superoxide Reactivity in Li-O 2 Batteries: Effect on Li 2O 2/LiOH Crystallization. *J. Am. Chem. Soc.* **2012**, *134* (6), 2902–2905. https://doi.org/10.1021/ja2111543.

(87) Oh, S. H.; Black, R.; Pomerantseva, E.; Lee, J. H.; Nazar, L. F. Synthesis of a Metallic Mesoporous Pyrochlore as a Catalyst for Lithium-O 2 Batteries. *Nat. Chem.* **2012**, *4* (12), 1004–1010. https://doi.org/10.1038/nchem.1499.

(88) McCloskey, B. D.; Bethune, D. S.; Shelby, R. M.; Mori, T.; Scheffler, R.; Speidel, A.; Sherwood, M.; Luntz, A. C. Limitations in Rechargeability of Li-o 2 Batteries and Possible Origins. *J. Phys. Chem. Lett.* **2012**, *3* (20), 3043–3047. https://doi.org/10.1021/jz301359t.

(89) Adams, B. D.; Radtke, C.; Black, R.; Trudeau, M. L.; Zaghib, K.; Nazar, L. F. Current Density Dependence of Peroxide Formation in the Li-O2 Battery and Its Effect on Charge. *Energy Environ. Sci.* **2013**, *6* (6), 1772–1778. https://doi.org/10.1039/c3ee40697k.

(90) Horstmann, B.; Gallant, B.; Mitchell, R.; Bessler, W. G.; Shao-Horn, Y.; Bazant, M. Z. Rate-Dependent Morphology of Li 2 O 2 Growth in Li−O2 Batteries Supporting Information. *J. Phys. Chem. Lett.* **2013**, *4*, 4217–4222.

(91) Zhai, D.; Wang, H. H.; Lau, K. C.; Gao, J.; Redfern, P. C.; Kang, F.; Li, B.; Indacochea, E.; Das, U.; Sun, H. H.; Sun, H. J.; Amine, K.; Curtiss, L. A. Raman Evidence for Late Stage Disproportionation in a Li-O2 Battery. *J. Phys. Chem. Lett.* **2014**, *5* (15), 2705–2710. https://doi.org/10.1021/jz501323n.

(92) Griffith, L. D.; Sleightholme, A. E. S.; Mansfield, J. F.; Siegel, D. J.; Monroe, C. W. Correlating Li/O2 Cell Capacity and Product Morphology with Discharge Current. *ACS Appl. Mater. Interfaces* **2015**, *7* (14), 7670–7678. https://doi.org/10.1021/acsami.5b00574.

(93) Lau, S.; Archer, L. A. Nucleation and Growth of Lithium Peroxide in the Li-O2 Battery. *Nano Lett.* **2015**, *15* (9), 5995–6002. https://doi.org/10.1021/acs.nanolett.5b02149.

(94) Schwenke, K. U.; Metzger, M.; Restle, T.; Piana, M.; Gasteiger, H. A. The Influence of Water and Protons on Li2O2 Crystal Growth in Aprotic Li-O 2 Cells. *J. Electrochem. Soc.* **2015**, *162* (4), A573–A584. https://doi.org/10.1149/2.0201504jes.

(95) Kwabi, D. G.; Batcho, T. P.; Feng, S.; Giordano, L.; Thompson, C. V.; Shao-Horn, Y. The Effect of Water on Discharge Product Growth and Chemistry in Li-O2 Batteries. *Phys. Chem. Chem. Phys.* **2016**, *18* (36), 24944–24953. https://doi.org/10.1039/c6cp03695c.

(96) Sharon, D.; Hirsberg, D.; Afri, M.; Chesneau, F.; Lavi, R.; Frimer, A. A.; Sun, Y. K.; Aurbach, D. Catalytic Behavior of Lithium Nitrate in Li-O2 Cells. *ACS Appl. Mater. Interfaces* **2015**, *7* (30), 16590–16600. https://doi.org/10.1021/acsami.5b04145.

(97) Sharon, D.; Etacheri, V.; Garsuch, A.; Afri, M.; Frimer, A. A.; Aurbach, D. On the Challenge of Electrolyte Solutions for Li-Air Batteries: Monitoring Oxygen Reduction and Related Reactions in Polyether Solutions by Spectroscopy and EQCM. *J. Phys. Chem. Lett.* **2013**, *4* (1), 127–131. https://doi.org/10.1021/jz3017842.

(98) Trahan, M. J.; Mukerjee, S.; Plichta, E. J.; Hendrickson, M. A.; Abraham, K. M. Studies of Li-Air Cells Utilizing Dimethyl Sulfoxide-Based Electrolyte. *J. Electrochem. Soc.* **2013**, *160* (2), A259–A267. https://doi.org/10.1149/2.048302jes.

(99) Ganapathy, S.; Adams, B. D.; Stenou, G.; Anastasaki, M. S.; Goubitz, K.; Miao, X. F.; Nazar, L. F.; Wagemaker, M. Nature of Li2O2 Oxidation in a Li-O2 Battery Revealed by Operando X-Ray Diffraction. *J. Am. Chem. Soc.* **2014**, *136* (46), 16335–16344. https://doi.org/10.1021/ja508794r.

(100) Kang, S.; Mo, Y.; Ong, S. P.; Ceder, G. A Facile Mechanism for Recharging Li2O2 in Li-O 2 Batteries. *Chem. Mater.* **2013**, *25* (16), 3328–3336. https://doi.org/10.1021/cm401720n.

(101) Luo, L.; Liu, B.; Song, S.; Xu, W.; Zhang, J. G.; Wang, C. Revealing the Reaction Mechanisms of Li-O2 Batteries Using Environmental Transmission Electron Microscopy. *Nat. Nanotechnol.* **2017**, *12* (6), 535–539. https://doi.org/10.1038/nnano.2017.27.

(102) Xu, W.; Xiao, J.; Zhang, J.; Wang, D.; Zhang, J.-G. Optimization of Nonaqueous Electrolytes for Primary Lithium/Air Batteries Operated in Ambient Environment. *J. Electrochem. Soc.* **2009**, *156* (10), A773. https://doi.org/10.1149/1.3168564.

(103) Tran, C.; Yang, X. Q.; Qu, D. Investigation of the Gas-Diffusion-Electrode Used as Lithium/Air Cathode in Non-Aqueous Electrolyte and the Importance of Carbon Material Porosity. *J. Power Sources* **2010**, *195* (7), 2057–2063. https://doi.org/10.1016/j.jpowsour.2009.10.012.

(104) Ogasawara, T.; Débart, A.; Holzapfel, M.; Novák, P.; Bruce, P. G. Rechargeable Li2O2 Electrode for Lithium Batteries. *J. Am. Chem. Soc.* **2006**, *128* (4), 1390–1393. https://doi.org/10.1021/ja056811q.

(105) Gutmann, V. Solvent Effects on the Reactivities of Organometallic Compounds. *Coord. Chem. Rev.* **1976**, *18* (2), 225–255. https://doi.org/10.1016/S0010-8545(00)82045-7.

(106) Chen, Y.; Freunberger, S. A.; Peng, Z.; Bardé, F.; Bruce, P. G. Li-O 2 Battery with a Dimethylformamide Electrolyte. *J. Am. Chem. Soc.* **2012**, *134* (18), 7952–7957. https://doi.org/10.1021/ja302178w.

(107) Zakharchenko, T. K.; Kozmenkova, A. Y.; Isaev, V. V.; Itkis, D. M.; Yashina, L. V. Positive Electrode Passivation by Side Discharge Products in Li-O2Batteries. *Langmuir* **2020**, *36* (30), 8716–8722. https://doi.org/10.1021/acs.langmuir.0c00853.

(108) Yu, Y.; Huang, G.; Du, J. Y.; Wang, J. Z.; Wang, Y.; Wu, Z. J.; Zhang, X. B. A Renaissance of: N, N -Dimethylacetamide-Based Electrolytes to Promote the Cycling Stability of Li-O2batteries. *Energy Environ. Sci.* **2020**, *13* (9), 3075–3081. https://doi.org/10.1039/d0ee01897j.

(109) Uddin, J.; Bryantsev, V. S.; Giordani, V.; Walker, W.; Chase, G. V.; Addison, D. Lithium Nitrate as Regenerable SEI Stabilizing Agent for Rechargeable Li/O2 Batteries. *J. Phys. Chem. Lett.* **2013**, *4* (21), 3760–3765. https://doi.org/10.1021/jz402025n.

(110) Schroeder, M. A.; Pearse, A. J.; Kozen, A. C.; Chen, X.; Gregorczyk, K.; Han, X.; Cao, A.; Hu, L.; Lee, S. B.; Rubloff, G. W.; Noked, M. Investigation of the Cathode-Catalyst-Electrolyte Interface in Aprotic Li-O2 Batteries. *Chem. Mater.* **2015**, *27* (15), 5305–5313. https://doi.org/10.1021/acs.chemmater.5b01605.

(111) Tang, M.; Chang, J. C.; Kumar, S. R.; Lue, S. J. Glyme-Based Electrolyte Formulation Analysis in Aprotic Lithium-Oxygen Battery and Its Cyclic Stability. *Energy* **2019**, *187*, 115926. https://doi.org/10.1016/j.energy.2019.115926.

(112) Rosy; Akabayov, S.; Leskes, M.; Noked, M. Bifunctional Role of LiNO3 in Li-O2 Batteries: Deconvoluting Surface and Catalytic Effects. *ACS Appl. Mater. Interfaces* **2018**, *10* (35), 29622–29629. https://doi.org/10.1021/acsami.8b10054.

(113) Khetan, A.; Luntz, A.; Viswanathan, V. Trade-Offs in Capacity and Rechargeability in Nonaqueous Li-O2 Batteries: Solution-Driven Growth versus Nucleophilic Stability. *J. Phys. Chem. Lett.* **2015**, *6* (7), 1254–1259. https://doi.org/10.1021/acs.jpclett.5b00324.

(114) Lutz, L.; Yin, W.; Grimaud, A.; Alves Dalla Corte, D.; Tang, M.; Johnson, L.; Azaceta, E.; Sarou-Kanian, V.; Naylor, A. J.; Hamad, S.; Anta, J. A.; Salager, E.; Tena-Zaera, R.; Bruce, P. G.; Tarascon, J. M. High Capacity Na-O2 Batteries: Key Parameters for Solution-Mediated Discharge. *J. Phys. Chem. C* **2016**, *120* (36), 20068–20076. https://doi.org/10.1021/acs.jpcc.6b07659.

(115) Liu, B.; Xu, W.; Yan, P.; Kim, S. T.; Engelhard, M. H.; Sun, X.; Mei, D.; Cho, J.; Wang, C. M.; Zhang, J. G. Stabilization of Li Metal Anode in DMSO-Based Electrolytes via Optimization of Salt–Solvent Coordination for Li–O2 Batteries. *Adv. Energy Mater.* **2017**, *7* (14). https://doi.org/10.1002/aenm.201602605.

(116) Leverick, G.; Tatara, R.; Feng, S.; Crabb, E.; France-Lanord, A.; Tułodziecki, M.; Lopez, J.; Stephens, R. M.; Grossman, J. C.; Shao-Horn, Y. Solvent- A Nd Anion-Dependent Li+-O2- Coupling Strength and Implications on the Thermodynamics and Kinetics of Li-O2 Batteries. *J. Phys. Chem. C* **2020**, *124* (9), 4953–4967. https://doi.org/10.1021/acs.jpcc.9b09968.

(117) Abraham, K. M. Electrolyte-Directed Reactions of the Oxygen Electrode in Lithium-Air Batteries. *J. Electrochem. Soc.* **2015**, *162* (2), A3021–A3031. https://doi.org/10.1149/2.0041502jes.

(118) Sharon, D.; Afri, M.; Noked, M.; Garsuch, A.; Frimer, A. A.; Aurbach, D. Oxidation of Dimethyl Sulfoxide Solutions by Electrochemical Reduction of Oxygen. **2013**.

(119) Kwabi, D. G.; Batcho, T. P.; Amanchukwu, C. V.; Ortiz-Vitoriano, N.; Hammond, P.; Thompson, C. V.; Shao-Horn, Y. Chemical Instability of Dimethyl Sulfoxide in Lithium-Air Batteries. *J. Phys. Chem. Lett.* **2014**, *5* (16), 2850–2856. https://doi.org/10.1021/jz5013824.

(120) Harvey, D. Analytical Chemistry 2.0: Chapter 11 Electrochemical Methods. **1999**, 667–781.

(121) Rusling, J. F.; Suib, S. L. Characterizing Materials with Cyclic Voltammetry. *Adv. Mater.* **1994**, *6* (12), 922–930. https://doi.org/10.1002/adma.19940061204.

(122) Capraz, O. O.; Shrotriya, P.; Hebert, K. R. Measurement of Stress Changes during Growth and Dissolution of Anodic Oxide Films on Aluminum. *J. Electrochem. Soc.* **2014**. https://doi.org/10.1149/2.057405jes.

(123) Rao, Z.; Hearne, S. J.; Chason, E. The Effects of Plating Current, Grain Size, and Electrolyte on Stress Evolution in Electrodeposited Ni. *J. Electrochem. Soc.* **2019**, *166* (1), D3212–D3218. https://doi.org/10.1149/2.0261901jes.

(124) Chason, E.; Shin, J. W.; Chen, C. H.; Engwall, A. M.; Miller, C. M.; Hearne, S. J.; Freund, L. B. Growth of Patterned Island Arrays to Identify Origins of Thin Film Stress. *J. Appl. Phys.* **2014**, *115* (12). https://doi.org/10.1063/1.4870051.

(125) Çapraz, Ö. The Role of Stress in Self-Ordered Porous Anodic Oxide Formation and Corrosion of Aluminum. **2014**.

(126) Çapraz, Ö. Ö.; Shrotriya, P.; Skeldon, P.; Thompson, G. E.; Hebert, K. R. Role of Oxide Stress in the Initial Growth of Self-Organized Porous Aluminum Oxide. *Electrochim. Acta* **2015**, *167*, 404–411. https://doi.org/10.1016/j.electacta.2015.03.017.

(127) Çapraz, Ö. Ö.; Ide, S.; Shrotriya, P.; Hebert, K. R. Tensile Stress and Plastic Deformation in Aluminum Induced by Aqueous Corrosion. *Acta Mater.* **2016**, *115*, 434–441. https://doi.org/10.1016/j.actamat.2016.05.028.

(128) Ha, Y.; Zeng, Z.; Cohen, Y.; Greeley, J.; Gewirth, A. A. Electrochemical Surface Stress Development during CO and NO Oxidation on Pt. *J. Phys. Chem. C* **2016**, *120* (16), 8674–8683. https://doi.org/10.1021/acs.jpcc.6b00697.

(129) Rao, Z.; Jin, H.; Engwall, A.; Chason, E.; Kim, K. S. Determination of Stresses in Incrementally Deposited Films from Wafer-Curvature Measurements. *J. Appl. Mech. Trans. ASME* **2020**, *87* (10), 1–6. https://doi.org/10.1115/1.4047572.

(130) Çapraz, Ö. Ö.; Bassett, K. L.; Gewirth, A. A.; Sottos, N. R. Electrochemical Stiffness Changes in Lithium Manganese Oxide Electrodes. *Adv. Energy Mater.* **2017**, *7* (7), 1601778. https://doi.org/10.1002/aenm.201601778.

(131) Tavassol, H.; Jones, E. M. C.; Sottos, N. R.; Gewirth, A. A. Electrochemical Stiffness in Lithium-Ion Batteries. *Nat. Mater.* **2016**, *15* (11), 1182–1188. https://doi.org/10.1038/nmat4708.

(132) Sheldon, B. W.; Nicholas, J. D.; Mandowara, S. Tensile Stress Evolution during the Early-Stage Constrained Sintering of Gadolinium-Doped Ceria Films. *J. Am. Ceram. Soc.* **2011**, *94* (1), 209–216. https://doi.org/10.1111/j.1551-2916.2010.04035.x.

(133) Chason, E.; Engwall, A. M.; Miller, C. M.; Chen, C. H.; Bhandari, A.; Soni, S. K.; Hearne, S. J.; Freund, L. B.; Sheldon, B. W. Stress Evolution during Growth of 1-D Island Arrays: Kinetics and Length Scaling. *Scr. Mater.* **2015**, *97*, 33–36. https://doi.org/10.1016/j.scriptamat.2014.10.012.

(134) Abadias, G.; Chason, E.; Keckes, J.; Sebastiani, M.; Thompson, G. B.; Barthel, E.; Doll, G. L.; Murray, C. E.; Stoessel, C. H.; Martinu, L. Review Article: Stress in Thin Films and Coatings: Current Status, Challenges, and Prospects. *J. Vac. Sci. Technol. A Vacuum, Surfaces, Film.* **2018**, *36* (2), 020801. https://doi.org/10.1116/1.5011790.

(135) Chason, E.; Sheldon, B. W.; Freund, L. B.; Floro, J. A.; Hearne, S. J. Origin of Compressive Residual Stress in Polycrystalline Thin Films. *Phys. Rev. Lett.* **2002**, *88* (15), 4. https://doi.org/10.1103/PhysRevLett.88.156103.

(136) Chason, E.; Guduru, P. R. Tutorial: Understanding Residual Stress in Polycrystalline Thin Films through Real-Time Measurements and Physical Models. *J. Appl. Phys.* **2016**, *119* (19). https://doi.org/10.1063/1.4949263.

(137) Tavassol, H.; Chan, M. K. Y.; Catarello, M. G.; Greeley, J.; Cahill, D. G.; Gewirth, A. A. Surface Coverage and SEI Induced Electrochemical Surface Stress Changes during Li Deposition in a Model System for Li-Ion Battery Anodes. *J. Electrochem. Soc.* **2013**, *160* (6), A888–A896. https://doi.org/10.1149/2.068306jes.

(138) Welzel, U.; Ligot, J.; Lamparter, P.; Vermeulen, A. C.; Mittemeijer, E. J. Stress Analysis of Polycrystalline Thin Films and Surface Regions by X-Ray Diffraction. *J. Appl. Crystallogr.* **2005**, *38* (1), 1–29. https://doi.org/10.1107/S0021889804029516.

(139) Stoney, G. G. The Tension o f Metallic Films Deposited by Electrolysis. **1909**, 172–175.

(140) Klein, C. A. How Accurate Are Stoney ' s Equation and. **2018**, *5487* (June 2000).

(141) Feng, X.; Huang, Y.; Rosakis, A. J. On the Stoney Formula for a Thin Film/Substrate System with Nonuniform Substrate Thickness. *J. Appl. Mech. Trans. ASME* **2007**, *74* (6), 1276–1281. https://doi.org/10.1115/1.2745392.

(142) Kongstein, O. E.; Bertocci, U.; Stafford, G. R. In Situ Stress Measurements during Copper Electrodeposition on (111)-Textured Au. *J. Electrochem. Soc.* **2005**, *152* (3), C116. https://doi.org/10.1149/1.1854093.

(143) Zhang, X.; Cahill, D. G. Measurements of Interface Stress of Silicon Dioxide in Contact with Water-Phenol Mixtures by Bending of Microcantilevers. *Langmuir* **2006**, *22* (21), 9062–9066. https://doi.org/10.1021/la061032o.

(144) Sethuraman, V. A.; Chon, M. J.; Shimshak, M.; Srinivasan, V.; Guduru, P. R. In Situ Measurements of Stress Evolution in Silicon Thin Films during Electrochemical Lithiation and Delithiation. *J. Power Sources* **2010**, *195* (15), 5062–5066. https://doi.org/10.1016/j.jpowsour.2010.02.013.

(145) Çapraz, Ö. Ö.; Hebert, K. R.; Shrotriya, P. In Situ Stress Measurement During Aluminum Anodizing Using Phase-Shifting Curvature Interferometry. *J. Electrochem. Soc.* **2013**, *160* (11), D501–D506. https://doi.org/10.1149/2.025311jes.

(146) Kramer, D.; Viswanath, R. N.; Weissmüller, J. Surface-Stress Induced Macroscopic Bending of Nanoporous Gold Cantilevers. *Nano Lett.* **2004**, *4* (5), 793–796. https://doi.org/10.1021/nl049927d.

(147) Kitamura, T.; Hirakata, H.; Itsuji, T. Effect of Residual Stress on Delamination from Interface Edge between Nano-Films. *Eng. Fract. Mech.* **2003**, *70* (15), 2089–2101. https://doi.org/10.1016/S0013-7944(02)00254-0.

(148) Greeley, J.; Warburton, R. E.; Castro, F. C.; Deshpande, S.; Madsen, K. E.; Bassett, K. L.; Dos Reis, R.; Gewirth, A. A.; Dravid, V. P. Oriented LiMn2O4 Particle Fracture from Delithiation-Driven Surface Stress. *ACS Appl. Mater. Interfaces* **2020**, *12* (43), 49182–49191. https://doi.org/10.1021/acsami.0c13305.

(149) Christensen, J.; Newman, J. Stress Generation and Fracture in Lithium Insertion Materials. *J. Solid State Electrochem.* **2006**, *10* (5), 293–319. https://doi.org/10.1007/s10008-006-0095-1.

(150) Çapraz, Ö. Ö.; Bassett, K. L.; Gewirth, A. A.; Sottos, N. R. Electrochemical Stiffness Changes in Lithium Manganese Oxide Electrodes. *Adv. Energy Mater.* **2017**, *7* (7). https://doi.org/10.1002/aenm.201601778.

(151) Sander, D.; Schmidthals, C.; Enders, A.; Kirschner, J. Stress and Structure of Ni Monolayers on W(110): The Importance of Lattice Mismatch. *Phys. Rev. B - Condens. Matter Mater. Phys.* **1998**, *57* (3), 1406–1409. https://doi.org/10.1103/PhysRevB.57.1406.

(152) Hearne, S.; Chason, E.; Han, J.; Floro, J. A.; Figiel, J.; Hunter, J.; Amano, H.; Tsong, I. S. T. Stress Evolution during Metalorganic Chemical Vapor Deposition of GaN. *Appl. Phys. Lett.* **1999**, *74* (3), 356–358. https://doi.org/10.1063/1.123070.

(153) Chason, E. A Kinetic Analysis of Residual Stress Evolution in Polycrystalline Thin Films. *Thin Solid Films* **2012**, *526*, 1–14. https://doi.org/10.1016/j.tsf.2012.11.001.

(154) Hoffman, R. W. Mechanical Properties of Non-Metallic Thin Films. *Phys. Nonmet. thin Film.* **1976**.

(155) Yu, Q.; Ye, S. In Situ Study of Oxygen Reduction in Dimethyl Sulfoxide (DMSO) Solution: A Fundamental Study for Development of the Lithium-Oxygen Battery. *J. Phys. Chem. C* **2015**, *119* (22), 12236–12250. https://doi.org/10.1021/acs.jpcc.5b03370.

(156) Ren, J.; Huang, Z.; Kalambate, P. K.; Shen, Y.; Huang, Y. Rotating-Disk Electrode Analysis of the Oxidation Behavior of Dissolved Li2O2 in Li-O2 Batteries. *RSC Adv.* **2018**, *8* (50), 28496–28502. https://doi.org/10.1039/c8ra03416h.

(157) Qiao, Y.; Ye, S. Spectroscopic Investigation for Oxygen Reduction and Evolution Reactions on Carbon Electrodes in Li-O2 Battery. *J. Phys. Chem. C* **2016**, *120* (15), 8033–8047. https://doi.org/10.1021/acs.jpcc.6b01784.

(158) Ganapathy, S.; Adams, B. D.; Stenou, G.; Anastasaki, M. S.; Goubitz, K.; Miao, X.; Nazar, L. F.; Wagemaker, M. Nature of Li 2 O 2 Oxidation in a Li − O 2 Battery Revealed by Operando. *J. Am. Chem. Soc.* **2014**, *136*, 16335–16344.

(159) Lim, H.; Yilmaz, E.; Byon, H. R. Real-Time XRD Studies of Li-O 2 Electrochemical Reaction in Nonaqueous Lithium-Oxygen Battery. *J. Phys. Chem. Lett.* **2012**, *3* (21), 3210–3215. https://doi.org/10.1021/jz301453t.

(160) Wang, Y.; Lu, Y. Isotopic Labeling Reveals Active Reaction Interfaces for Electrochemical Oxidation of Lithium Peroxide. *Angew. Chemie* **2019**, *131* (21), 7036–7040. https://doi.org/10.1002/ange.201901350.

(161) Lu, Y. C.; Crumlin, E. J.; Veith, G. M.; Harding, J. R.; Mutoro, E.; Baggetto, L.; Dudney, N. J.; Liu, Z.; Shao-Horn, Y. In Situ Ambient Pressure X-Ray Photoelectron Spectroscopy Studies of Lithium-Oxygen Redox Reactions. *Sci. Rep.* **2012**, *2*, 1–6. https://doi.org/10.1038/srep00715.

(162) Schroeder, M. A.; Kumar, N.; Pearse, A. J.; Liu, C.; Lee, S. B.; Rubloff, G. W.; Leung, K.; Noked, M. DMSO-Li2O2 Interface in the Rechargeable Li-O2 Battery Cathode: Theoretical and Experimental Perspectives on Stability. *ACS Appl. Mater. Interfaces* **2015**, *7* (21), 11402–11411. https://doi.org/10.1021/acsami.5b01969.

(163) Olivares-Marín, M.; Sorrentino, A.; Pereiro, E.; Tonti, D. Discharge Products of Ionic Liquid-Based Li-O2 Batteries Observed by Energy Dependent Soft x-Ray Transmission Microscopy. *J. Power Sources* **2017**, *359*, 234–241. https://doi.org/10.1016/j.jpowsour.2017.05.039.

(164) Zhong, L.; Mitchell, R. R.; Liu, Y.; Gallant, B. M.; Thompson, C. V.; Huang, J. Y.; Mao, S. X.; Shao-Horn, Y. In Situ Transmission Electron Microscopy Observations of Electrochemical Oxidation of Li2O2. *Nano Lett.* **2013**, *13* (5), 2209–2214. https://doi.org/10.1021/nl400731w.

(165) Kushima, A.; Koido, T.; Fujiwara, Y.; Kuriyama, N.; Kusumi, N.; Li, J. Charging/Discharging Nanomorphology Asymmetry and Rate-Dependent Capacity Degradation in Li-Oxygen Battery. *Nano Lett.* **2015**, *15* (12), 8260–8265. https://doi.org/10.1021/acs.nanolett.5b03812.

(166) Cao, R.; Walter, E. D.; Xu, W.; Nasybulin, E. N.; Bhattacharya, P.; Bowden, M. E.; Engelhard, M. H.; Zhang, J.-G. The Mechanisms of Oxygen Reduction and Evolution Reactions in Nonaqueous Lithium-Oxygen Batteries. *ChemSusChem* **2014**, *7* (9), 2436–2440. https://doi.org/10.1002/cssc.201402315.

(167) Van Overmeere, Q.; Nysten, B.; Proost, J. *In Situ* Detection of Porosity Initiation during Aluminum Thin Film Anodizing. *Appl. Phys. Lett.* **2009**, *94* (7), 074103. https://doi.org/10.1063/1.3081014.

(168) Çapraz, Ö. Ö.; Shrotriya, P.; Skeldon, P.; Thompson, G. E.; Hebert, K. R. Factors Controlling Stress Generation during the Initial Growth of Porous Anodic Aluminum Oxide. *Electrochim. Acta* **2015**, *159*, 16–22. https://doi.org/10.1016/j.electacta.2015.01.183.

(169) Capraz, O. O.; Hebert, K. R.; Shrotriya, P. In Situ Stress Measurement During Aluminum Anodizing Using Phase-Shifting Curvature Interferometry. *J. Electrochem. Soc.* **2013**. https://doi.org/10.1149/2.025311jes.

(170) Mukhopadhyay, A.; Sheldon, B. W. Deformation and Stress in Electrode Materials for Li-Ion Batteries. *Prog. Mater. Sci.* **2014**, *63*, 58–116. https://doi.org/10.1016/J.PMATSCI.2014.02.001.

(171) Stafford, G. R.; Bertocci, U. In Situ Stress and Nanogravimetric Measurements During Hydrogen Adsorption/Absorption on Pd Overlayers Deposited onto (111)-Textured Au. *J. Phys. Chem. C* **2009**, *113* (30), 13249–13256. https://doi.org/10.1021/jp902382q.

(172) Shin, J. W.; Stafford, G. R.; Hebert, K. R. Stress in Aluminum Induced by Hydrogen Absorption during Cathodic Polarization. *Corros. Sci.* **2015**, *98*, 366–371. https://doi.org/10.1016/J.CORSCI.2015.05.015.

(173) Ha, Y.; Zeng, Z.; Cohen, Y.; Greeley, J.; Gewirth, A. A. Electrochemical Surface Stress Development during CO and NO Oxidation on Pt. *J. Phys. Chem. C* **2016**, *120* (16), 8674–8683. https://doi.org/10.1021/acs.jpcc.6b00697.

(174) Mickelson, L. L.; Friesen, C. Direct Observation of Bifunctional Electrocatalysis during CO Oxidation at Ru $_{\Theta=0.37}$ /Pt{111} Surfaces via Surface Stress Measurements. *J. Am. Chem. Soc.* **2009**, *131* (41), 14879–14884. https://doi.org/10.1021/ja904432c.

(175) Ha, Y.; Oberst, J. L.; Zeng, Z.; Hoang, T. T. H.; Cohen, Y.; Wetzel, D. J.; Nuzzo, R. G.; Greeley, J.; Gewirth, A. A. In Situ Surface Stress Measurement and Computational Analysis Examining the Oxygen Reduction Reaction on Pt and Pd. *Electrochim. Acta* **2018**, *260*, 400–406. https://doi.org/10.1016/j.electacta.2017.12.039.

(176) Sethuraman, V. A.; Vairavapandian, D.; Lafouresse, M. C.; Adit Maark, T.; Karan, N.; Sun, S.; Bertocci, U.; Peterson, A. A.; Stafford, G. R.; Guduru, P. R. Role of Elastic Strain on Electrocatalysis of Oxygen Reduction Reaction on Pt. *J. Phys. Chem. C* **2015**, *119* (33), 19042–19052. https://doi.org/10.1021/acs.jpcc.5b06096.

(177) Klein, C. A. How Accurate Are Stoney's Equation and Recent Modifications. **2018**, *5487* (June 2000).

(178) Van Overmeere, Q.; Vanhumbeeck, J. F.; Proost, J. On the Use of a Multiple Beam Optical Sensor for in Situ Curvature Monitoring in Liquids. *Rev. Sci. Instrum.* **2010**, *81* (4). https://doi.org/10.1063/1.3385432.

(179) Aurbach, D.; Daroux, M.; Faguy, P.; Yeager, E. The Electrochemistry of Noble Metal Electrodes in Aprotic Organic Solvents Containing Lithium Salts. *J. Electroanal. Chem.* **1991**, *297* (1), 225–244. https://doi.org/10.1016/0022-0728(91)85370-5.

(180) Saito, T.; Uosaki, K. Surface Film Formation and Lithium Underpotential Deposition on Au(111) Surfaces in Propylene Carbonate. *J. Electrochem. Soc.* **2003**, *150* (4), A532. https://doi.org/10.1149/1.1557966.

(181) Moshkovich, M.; Gofer, Y.; Aurbach, D. Investigation of the Electrochemical Windows of Aprotic Alkali Metal (Li, Na, K) Salt Solutions. *J. Electrochem. Soc.* **2001**, *148* (4), E155. https://doi.org/10.1149/1.1357316.

(182) Seo, M.; Yamazaki, M. Changes in Surface Stress of Gold Electrode during Underpotential Deposition of Pb. *J. Electrochem. Soc.* **2004**, *151* (8), E276. https://doi.org/10.1149/1.1766310.

(183) Shin, J. W.; Bertocci, U.; Stafford, G. R. Underpotential Deposition of Tl on (111)-Textured Au: In Situ Stress and Nanogravimetric Measurements. *J. Phys. Chem. C* **2010**, *114* (41), 17621–17628. https://doi.org/10.1021/jp1034486.

(184) Seo, M.; Yamazaki, M. Changes in Surface Stress of Gold Electrode during Underpotential Deposition of Copper. *J. Solid State Electrochem.* **2007**, *11* (10), 1365–1373. https://doi.org/10.1007/s10008-007-0294-4.

(185) Hearne, S. J.; Floro, J. A. Mechanisms Inducing Compressive Stress during Electrodeposition of Ni. *J. Appl. Phys.* **2005**, *97* (1). https://doi.org/10.1063/1.1819972.

(186) Mo, Y.; Gofer, Y.; Hwang, E.; Wang, Z.; Scherson, D. A. Simultaneous Microgravimetric and Optical Reflectivity Studies of Lithium Underpotential Deposition on Au(111) from Propylene Carbonate Electrolytes. *J. Electroanal. Chem.* **1996**, *409* (1–2), 87–93. https://doi.org/10.1016/0022-0728(96)04633-5.

(187) Gasparotto, L. H. S.; Borisenko, N.; Bocchi, N.; Zein El Abedin, S.; Endres, F. In Situ STM Investigation of the Lithium Underpotential Deposition on Au(111) in the Air- and Water-Stable Ionic Liquid 1-Butyl-1-Methylpyrrolidinium Bis(Trifluoromethylsulfonyl)Amide. *Phys. Chem. Chem. Phys.* **2009**, *11* (47), 11140–11145. https://doi.org/10.1039/b916809e.

(188) Matsui, T.; Takeyama, K. Li + Adsorption on a Metal Electrode from Glymes. *Electrochim. Acta* **1998**, *43*, 1355–1360.

(189) Kwak, W. J.; Hirshberg, D.; Sharon, D.; Shin, H. J.; Afri, M.; Park, J. B.; Garsuch, A.; Chesneau, F. F.; Frimer, A. A.; Aurbach, D.; Sun, Y. K. Understanding the Behavior of Li-Oxygen Cells Containing LiI. *J. Mater. Chem. A* **2015**, *3* (16), 8855–8864. https://doi.org/10.1039/c5ta01399b.

(190) Jache, B.; Binder, J. O.; Abe, T.; Adelhelm, P. A Comparative Study on the Impact of Different Glymes and Their Derivatives as Electrolyte Solvents for Graphite Co-Intercalation Electrodes in Lithium-Ion and Sodium-Ion Batteries. *Phys. Chem. Chem. Phys.* **2016**, *18* (21), 14299–14316. https://doi.org/10.1039/c6cp00651e.

(191) Shin, J. W.; Chason, E. Compressive Stress Generation in Sn Thin Films and the Role of Grain Boundary Diffusion. *Phys. Rev. Lett.* **2009**, *103* (5), 1–4. https://doi.org/10.1103/PhysRevLett.103.056102.

(192) Fayette, M.; Bertocci, U.; Stafford, G. R. In Situ Stress Measurements during Cobalt Electrodeposition on (111)-Textured Au. *J. Electrochem. Soc.* **2016**, *163* (5), D146–D153. https://doi.org/10.1149/2.0511605jes.

(193) Wang, L.; Uosaki, K.; Noguchi, H. Effect of Electrolyte Concentration on the Solvation Structure of Gold/LITFSI-DMSO Solution Interface. *J. Phys. Chem. C* **2020**, *124* (23), 12381–12389. https://doi.org/10.1021/acs.jpcc.0c00827.

(194) Gittleson, F. S.; Ryu, W. H.; Schwab, M.; Tong, X.; Taylor, A. D. Pt and Pd Catalyzed Oxidation of Li2O2 and DMSO during Li-O2 Battery Charging. *Chem. Commun.* **2016**, *52* (39), 6605–6608. https://doi.org/10.1039/c6cc01778a.

(195) Mccloskey, B. D.; Garcia, J. M.; Luntz, A. C. Chemical and Electrochemical Di Ff Erences in Nonaqueous Li − O 2 and Na − O 2 Batteries. **2014**, 2–7.

(196) Kang, S.; Mo, Y.; Ong, S. P.; Ceder, G. Nanoscale Stabilization of Sodium Oxides: Implications for Na-O2 Batteries. *Nano Lett.* **2014**, *14* (2), 1016–1020. https://doi.org/10.1021/nl404557w.

(197) Li, M.; Lu, J.; Chen, Z.; Amine, K. 30 Years of Lithium-Ion Batteries. *Adv. Mater.* **2018**, *30* (33), 1–24. https://doi.org/10.1002/adma.201800561.

(198) Berckmans, G.; Messagie, M.; Smekens, J.; Omar, N.; Vanhaverbeke, L.; Mierlo, J. Van. Cost Projection of State of the Art Lithium-Ion Batteries for Electric Vehicles up to 2030. *Energies* **2017**, *10* (9). https://doi.org/10.3390/en10091314.

(199) Slater, M. D.; Kim, D.; Lee, E.; Johnson, C. S. Sodium-Ion Batteries. *Adv. Funct. Mater.* **2013**, *23* (8), 947–958. https://doi.org/10.1002/adfm.201200691.

(200) Kubota, K.; Dahbi, M.; Hosaka, T.; Kumakura, S.; Komaba, S. Towards K-Ion and Na-Ion Batteries as "Beyond Li-Ion." *Chem. Rec.* **2018**, *18* (4), 459–479. https://doi.org/10.1002/tcr.201700057.

(201) Song, J.; Xiao, B.; Lin, Y.; Xu, K.; Li, X. Interphases in Sodium-Ion Batteries. *Advanced Energy Materials*. Wiley-VCH Verlag June 2018. https://doi.org/10.1002/aenm.201703082.

(202) Xiang, K.; Xing, W.; Ravnsbæk, D. B.; Hong, L.; Tang, M.; Li, Z.; Wiaderek, K. M.; Borkiewicz, O. J.; Chapman, K. W.; Chupas, P. J.; Chiang, Y. M. Accommodating High Transformation Strains in Battery Electrodes via the Formation of Nanoscale Intermediate Phases: Operando Investigation of Olivine NaFePO4. *Nano Lett.* **2017**, *17* (3), 1696–1702. https://doi.org/10.1021/acs.nanolett.6b04971.

(203) Zhao, K.; Pharr, M.; Cai, S.; Vlassak, J. J.; Suo, Z. Large Plastic Deformation in High-Capacity Lithium-Ion Batteries Caused by Charge and Discharge. *J. Am. Ceram. Soc.* **2011**, *94* (SUPPL. 1), s226–s235. https://doi.org/10.1111/j.1551-2916.2011.04432.x.

(204) Bonilla, M. R.; Lozano, A.; Escribano, B.; Carrasco, J.; Akhmatskaya, E. Revealing the Mechanism of Sodium Diffusion in NaxFePO4 Using an Improved Force Field. *J. Phys. Chem. C* **2018**, *122* (15), 8065–8075. https://doi.org/10.1021/acs.jpcc.8b00230.

(205) Wang, C. M.; Li, X.; Wang, Z.; Xu, W.; Liu, J.; Gao, F.; Kovarik, L.; Zhang, J. G.; Howe, J.; Burton, D. J.; Liu, Z.; Xiao, X.; Thevuthasan, S.; Baer, D. R. In Situ TEM Investigation of Congruent Phase Transition and Structural Evolution of Nanostructured Silicon/Carbon Anode for Lithium Ion Batteries. *Nano Lett.* **2012**, *12* (3), 1624–1632. https://doi.org/10.1021/nl204559u.

(206) Gu, M.; Li, Y.; Li, X.; Hu, S.; Zhang, X.; Xu, W.; Thevuthasan, S.; Baer, D. R.; Zhang, J. G.; Liu, J.; Wang, C. In Situ TEM Study of Lithiation Behavior of Silicon Nanoparticles Attached to and Embedded in a Carbon Matrix. *ACS Nano* **2012**, *6* (9), 8439–8447. https://doi.org/10.1021/nn303312m.

(207) Liu, X. H.; Liu, Y.; Kushima, A.; Zhang, S.; Zhu, T.; Li, J.; Huang, J. Y. In Situ TEM Experiments of Electrochemical Lithiation and Delithiation of Individual Nanostructures. *Adv. Energy Mater.* **2012**, *2* (7), 722–741. https://doi.org/10.1002/aenm.201200024.

(208) Xie, H.; Tan, X.; Luber, E. J.; Olsen, B. C.; Kalisvaart, W. P.; Jungjohann, K. L.; Mitlin, D.; Buriak, J. M. β-SnSb for Sodium Ion Battery Anodes: Phase Transformations Responsible for Enhanced Cycling Stability Revealed by in Situ TEM. *ACS Energy Lett.* **2018**, *3* (7), 1670–1676. https://doi.org/10.1021/acsenergylett.8b00762.

(209) Lu, X.; Adkins, E. R.; He, Y.; Zhong, L.; Luo, L.; Mao, S. X.; Wang, C. M.; Korgel, B. A. Germanium as a Sodium Ion Battery Material: In Situ TEM Reveals Fast Sodiation Kinetics with High Capacity. *Chem. Mater.* **2016**, *28* (4), 1236–1242. https://doi.org/10.1021/acs.chemmater.6b00200.

(210) Yang, Z.; Sun, J.; Ni, Y.; Zhao, Z.; Bao, J.; Chen, S. Facile Synthesis and in Situ Transmission Electron Microscopy Investigation of a Highly Stable Sb2Te3/C Nanocomposite for Sodium-Ion Batteries. *Energy Storage Mater.* **2017**, *9*, 214–220. https://doi.org/10.1016/j.ensm.2017.07.010.

(211) Xia, W.; Xu, F.; Zhu, C.; Xin, H. L.; Xu, Q.; Sun, P.; Sun, L. Probing Microstructure and Phase Evolution of α-MoO3 Nanobelts for Sodium-Ion Batteries by in Situ Transmission Electron Microscopy. *Nano Energy* **2016**, *27*, 447–456. https://doi.org/10.1016/j.nanoen.2016.07.017.

(212) Wang, X.; Yao, Z.; Hwang, S.; Pan, Y.; Dong, H.; Fu, M.; Li, N.; Sun, K.; Gan, H.; Yao, Y.; Aspuru-Guzik, A.; Xu, Q.; Su, D. In Situ Electron Microscopy Investigation of Sodiation of Titanium Disulfide Nanoflakes. *ACS Nano* **2019**, *13* (8), 9421–9430. https://doi.org/10.1021/acsnano.9b04222.

(213) Tokranov, A.; Sheldon, B. W.; Li, C.; Minne, S.; Xiao, X. In Situ Atomic Force Microscopy Study of Initial Solid Electrolyte Interphase Formation on Silicon Electrodes for Li-Ion Batteries. *ACS Appl. Mater. Interfaces* **2014**, *6* (9), 6672–6686. https://doi.org/10.1021/am500363t.

(214) Demirocak, D. E.; Bhushan, B. In Situ Atomic Force Microscopy Analysis of Morphology and Particle Size Changes in Lithium Iron Phosphate Cathode during Discharge. *J. Colloid Interface Sci.* **2014**, *423*, 151–157. https://doi.org/10.1016/j.jcis.2014.02.035.

(215) Park, J.; Kalnaus, S.; Han, S.; Lee, Y. K.; Less, G. B.; Dudney, N. J.; Daniel, C.; Sastry, A. M. In Situ Atomic Force Microscopy Studies on Lithium (de)Intercalation- Induced Morphology Changes in LixCoO2 Micro-Machined Thin Film Electrodesq. *J. Power Sources* **2013**, *222*, 417–425. https://doi.org/10.1016/j.jpowsour.2012.09.017.

(216) Lacey, S. D.; Wan, J.; Cresce, A. V. W.; Russell, S. M.; Dai, J.; Bao, W.; Xu, K.; Hu, L. Atomic Force Microscopy Studies on Molybdenum Disulfide Flakes as Sodium-Ion Anodes. *Nano Lett.* **2015**, *15* (2), 1018–1024. https://doi.org/10.1021/nl503871s.

(217) Han, M.; Zhu, C.; Zhao, Q.; Chen, C.; Tao, Z.; Xie, W.; Cheng, F.; Chen, J. In Situ Atomic Force Microscopic Studies of Single Tin Nanoparticle: Sodiation and Desodiation in Liquid Electrolyte. *ACS Appl. Mater. Interfaces* **2017**, *9* (34), 28620–28626. https://doi.org/10.1021/acsami.7b08870.

(218) Chen, G.; Song, X.; Richardson, T. J. Electron Microscopy Study of the LiFePO 4 to FePO 4 Phase Transition. *Electrochem. Solid-State Lett.* **2006**, *9* (6), 4–8. https://doi.org/10.1149/1.2192695.

(219) Liu, Q.; He, H.; Li, Z. F.; Liu, Y.; Ren, Y.; Lu, W.; Lu, J.; Stach, E. A.; Xie, J. Rate-Dependent, Li-Ion Insertion/Deinsertion Behavior of LiFePO4 Cathodes in Commercial 18650 LiFePO4 Cells. *ACS Appl. Mater. Interfaces* **2014**, *6* (5), 3282–3289. https://doi.org/10.1021/am405150c.

(220) Wang, J.; Eng, C.; Chen-Wiegart, Y. C. K.; Wang, J. Probing Three-Dimensional Sodiation-Desodiation Equilibrium in Sodium-Ion Batteries by in Situ Hard X-Ray Nanotomography. *Nat. Commun.* **2015**, *6* (1), 1–9. https://doi.org/10.1038/ncomms8496.

(221) Ou, X.; Liang, X.; Zheng, F.; Wu, P.; Pan, Q.; Xiong, X.; Yang, C.; Liu, M. In Situ X-Ray Diffraction Investigation of CoSe2 Anode for Na-Ion Storage: Effect of Cut-off Voltage on Cycling Stability. *Electrochim. Acta* **2017**, *258*, 1387–1396. https://doi.org/10.1016/j.electacta.2017.11.198.

(222) Talaie, E.; Duffort, V.; Smith, H. L.; Fultz, B.; Nazar, L. F. Structure of the High Voltage Phase of Layered P2-Na2/3-z[Mn1/2Fe1/2]O2 and the Positive Effect of Ni Substitution on Its Stability. *Energy Environ. Sci.* **2015**, *8* (8), 2512–2523. https://doi.org/10.1039/c5ee01365h.

(223) Li, M.; Wang, Z.; Fu, J.; Ma, K.; Detsi, E. In Situ Electrochemical Dilatometry Study of Capacity Fading in Nanoporous Ge-Based Na-Ion Battery Anodes. *Scr. Mater.* **2019**, *164*, 52–56. https://doi.org/10.1016/j.scriptamat.2019.01.030.

(224) Karimi, N.; Varzi, A.; Passerini, S. A Comprehensive Insight into the Volumetric Response of Graphite Electrodes upon Sodium Co-Intercalation in Ether-Based Electrolytes. *Electrochim. Acta* **2019**, *304*, 474–486. https://doi.org/10.1016/j.electacta.2019.03.036.

(225) Özdogru, B.; Dykes, H.; Padwal, S.; Harimkar, S.; Çapraz, Ö. Electrochemical Strain Evolution in Iron Phosphate Composite Cathodes during Lithium and Sodium Ion Intercalation. *Electrochim. Acta* **2020**, *353*. https://doi.org/10.1016/j.electacta.2020.136594.

(226) Jones, E. M. C.; Silberstein, M. N.; White, S. R.; Sottos, N. R. In Situ Measurements of Strains in Composite Battery Electrodes during Electrochemical Cycling. *Exp. Mech.* **2014**, *54* (6), 971–985. https://doi.org/10.1007/s11340-014-9873-3.

(227) Wang, J.; Chen-Wiegart, Y. C. K.; Wang, J. In Operando Tracking Phase Transformation Evolution of Lithium Iron Phosphate with Hard X-Ray Microscopy. *Nat. Commun.* **2014**, *5* (1), 1–10. https://doi.org/10.1038/ncomms5570.

(228) Zhao, K.; Pharr, M.; Vlassak, J. J.; Suo, Z. Fracture of Electrodes in Lithium-Ion Batteries Caused by Fast Charging. *J. Appl. Phys.* **2010**, *108* (7). https://doi.org/10.1063/1.3492617.

(229) Cheng, Y. T.; Verbrugge, M. W. The Influence of Surface Mechanics on Diffusion Induced Stresses within Spherical Nanoparticles. *J. Appl. Phys.* **2008**, *104* (8). https://doi.org/10.1063/1.3000442.

(230) Cheng, Y.-T.; Verbrugge, M. W. Diffusion-Induced Stress, Interfacial Charge Transfer, and Criteria for Avoiding Crack Initiation of Electrode Particles. *J. Electrochem. Soc.* **2010**, *157* (4), A508. https://doi.org/10.1149/1.3298892.

(231) Cheng, Y. T.; Verbrugge, M. W. Evolution of Stress within a Spherical Insertion Electrode Particle under Potentiostatic and Galvanostatic Operation. *J. Power Sources* **2009**, *190* (2), 453–460. https://doi.org/10.1016/j.jpowsour.2009.01.021.

(232) Christensen, J.; Newman, J. A Mathematical Model of Stress Generation and Fracture in Lithium Manganese Oxide. *J. Electrochem. Soc.* **2006**, *153* (6), A1019. https://doi.org/10.1149/1.2185287.

(233) Li, G.; Monroe, C. W. Annual Review of Chemical and Biomolecular Engineering Multiscale Lithium-Battery Modeling from Materials to Cells. **2020**. https://doi.org/10.1146/annurev-chembioeng.

(234) Chen, J.; Thapa, A. K.; Berfield, T. A. In-Situ Characterization of Strain in Lithium Battery Working Electrodes. *J. Power Sources* **2014**, *271*, 406–413. https://doi.org/10.1016/j.jpowsour.2014.08.035.

(235) Heubner, C.; Heiden, S.; Matthey, B.; Schneider, M.; Michaelis, A. Sodiation vs. Lithiation of FePO4: A Comparative Kinetic Study. *Electrochim. Acta* **2016**, *216*, 412–419. https://doi.org/10.1016/j.electacta.2016.09.041.

(236) Heubner, C.; Heiden, S.; Schneider, M.; Michaelis, A. In-Situ Preparation and Electrochemical Characterization of Submicron Sized NaFePO4 Cathode Material for Sodium-Ion Batteries. *Electrochim. Acta* **2017**, *233*, 78–84. https://doi.org/10.1016/j.electacta.2017.02.107.

(237) Galceran, M.; Saurel, D.; Acebedo, B.; Roddatis, V. V.; Martin, E.; Rojo, T.; Casas-Cabanas, M. The Mechanism of NaFePO4 (de)Sodiation Determined by in Situ X-Ray Diffraction. *Phys. Chem. Chem. Phys.* **2014**, *16* (19), 8837–8842. https://doi.org/10.1039/c4cp01089b.

(238) Casas-Cabanas, M.; Roddatis, V. V.; Saurel, D.; Kubiak, P.; Carretero-González, J.; Palomares, V.; Serras, P.; Rojo, T. Crystal Chemistry of Na Insertion/Deinsertion in FePO 4- NaFePO 4. *J. Mater. Chem.* **2012**, *22* (34), 17421–17423. https://doi.org/10.1039/c2jm33639a.

(239) Saracibar, A.; Carrasco, J.; Saurel, D.; Galceran, M.; Acebedo, B.; Anne, H.; Lepoitevin, M.; Rojo, T.; Casas Cabanas, M. Investigation of Sodium Insertion-Extraction in Olivine Na: XFePO4 ($0 \leq x \leq 1$) Using First-Principles Calculations. *Phys. Chem. Chem. Phys.* **2016**, *18* (18), 13045–13051. https://doi.org/10.1039/c6cp00762g.

(240) Saurel, D.; Galceran, M.; Reynaud, M.; Anne, H.; Casas-Cabanas, M. Rate Dependence of the Reaction Mechanism in Olivine NaFePO4 Na-Ion Cathode Material. *Int. J. Energy Res.* **2018**, *42* (10), 3258–3265. https://doi.org/10.1002/er.4078.

(241) Galceran, M.; Roddatis, V.; Zúñiga, F. J.; Pérez-Mato, J. M.; Acebedo, B.; Arenal, R.; Peral, I.; Rojo, T.; Casas-Cabanas, M. Na-Vacancy and Charge Ordering in Na≈2/3FePO4. *Chem. Mater.* **2014**, *26* (10), 3289–3294. https://doi.org/10.1021/cm501110v.

(242) Zheng, H.; Yang, R.; Liu, G.; Song, X.; Battaglia, V. S. Cooperation between Active Material, Polymeric Binder and Conductive Carbon Additive in Lithium Ion Battery Cathode. *J. Phys. Chem. C* **2012**, *116* (7), 4875–4882. https://doi.org/10.1021/jp208428w.

(243) Chen, J.; Liu, J.; Qi, Y.; Sun, T.; Li, X. Unveiling the Roles of Binder in the Mechanical Integrity of Electrodes for Lithium-Ion Batteries. *J. Electrochem. Soc.* **2013**, *160* (9), A1502–A1509. https://doi.org/10.1149/2.088309jes.

(244) Lu, Z.; Liu, N.; Lee, H. W.; Zhao, J.; Li, W.; Li, Y.; Cui, Y. Nonfilling Carbon Coating of Porous Silicon Micrometer-Sized Particles for High-Performance Lithium Battery Anodes. *ACS Nano* **2015**, *9* (3), 2540–2547. https://doi.org/10.1021/nn505410q.

(245) Shpigel, N.; Levi, M. D.; Sigalov, S.; Girshevitz, O.; Aurbach, D.; Daikhin, L.; Jäckel, N.; Presser, V. Non-Invasive in Situ Dynamic Monitoring of Elastic Properties of Composite Battery Electrodes by EQCM-D. *Angew. Chemie - Int. Ed.* **2015**, *54* (42), 12353–12356. https://doi.org/10.1002/anie.201501787.

(246) McGee, Stuart; McCullough, R. L. Combining Rules for Predicting the Thermoelastic Properties of Particulate Filled Polymers, Polyblends, and Foams. *Polym. Compos.* **1981**, *2*, 149–161.

(247) Zhang, X.; Shyy, W.; Marie Sastry, A. Numerical Simulation of Intercalation-Induced Stress in Li-Ion Battery Electrode Particles. *J. Electrochem. Soc.* **2007**, *154* (10), A910. https://doi.org/10.1149/1.2759840.

(248) Woodford, W. H.; Chiang, Y.-M.; Carter, W. C. "Electrochemical Shock" of Intercalation Electrodes: A Fracture Mechanics Analysis. *J. Electrochem. Soc.* **2010**, *157* (10), A1052. https://doi.org/10.1149/1.3464773.

(249) Bucci, G.; Swamy, T.; Bishop, S.; Sheldon, B. W.; Chiang, Y.-M.; Carter, W. C. The Effect of Stress on Battery-Electrode Capacity. *J. Electrochem. Soc.* **2017**, *164* (4), A645–A654. https://doi.org/10.1149/2.0371704jes.

(250) Zhu, Y.; Wang, C. Strain Accommodation and Potential Hysteresis of LiFePO4 Cathodes during Lithium Ion Insertion/Extraction. *J. Power Sources* **2011**, *196* (3), 1442–1448. https://doi.org/10.1016/j.jpowsour.2010.08.008.

(251) Gaubicher, J.; Boucher, F.; Moreau, P.; Cuisinier, M.; Soudan, P.; Elkaim, E.; Guyomard, D. Abnormal Operando Structural Behavior of Sodium Battery Material: Influence of Dynamic on Phase Diagram of NaxFePO4. *Electrochem. commun.* **2014**, *38*, 104–106. https://doi.org/10.1016/j.elecom.2013.11.017.

(252) Soni, S. K.; Sheldon, B. W.; Xiao, X.; Bower, A. F.; Verbrugge, M. W. Diffusion Mediated Lithiation Stresses in Si Thin Film Electrodes. *J. Electrochem. Soc.* **2012**, *159* (9), A1520–A1527. https://doi.org/10.1149/2.009209jes.

(253) Sethuraman, V. A.; Srinivasan, V.; Bower, A. F.; Guduru, P. R. In Situ Measurements of Stress-Potential Coupling in Lithiated Silicon. *J. Electrochem. Soc.* **2010**, *157* (11), A1253. https://doi.org/10.1149/1.3489378.

(254) De Jong, M.; Chen, W.; Angsten, T.; Jain, A.; Notestine, R.; Gamst, A.; Sluiter, M.; Ande, C. K.; Van Der Zwaag, S.; Plata, J. J.; Toher, C.; Curtarolo, S.; Ceder, G.; Persson, K. A.; Asta, M. Charting the Complete Elastic Properties of Inorganic Crystalline Compounds. *Sci. Data* **2015**, *2*, 1–13. https://doi.org/10.1038/sdata.2015.9.

(255) Zhang, T.; Kamlah, M. Sodium Ion Batteries Particles: Phase-Field Modeling with Coupling of Cahn-Hilliard Equation and Finite Deformation Elasticity. *J. Electrochem. Soc.* **2018**, *165* (10), A1997–A2007. https://doi.org/10.1149/2.0141810jes.

(256) Chemical Book. Carboxymethyl Cellulose https://www.chemicalbook.com/ProductChemicalPropertiesCB5209844_EN.htm (accessed Apr 14, 2020).

(257) International Program on Chemical Safety. Carbon Black http://www.inchem.org/documents/icsc/icsc/eics0471.htm (accessed Jun 1, 2020).

APPENDICES

APPENDIX A

Supplemental Information for In Situ Stress Measurements on Thin Film Au Cathode during First Discharge of Li-O_2 Batteries

A1. Multibeam Optical Sensor (MOS) Technique

The kSA MOS system was used to measure the wafer curvature. The MOS system is composed of an AlGaInP Diode, two etalons, a lens, a mirror and a CCD camera as shown in Figure A1. Etalons were used to control the spot spacing, linearity of the beams, and the number of beams in the array. A mirror with servo control is used to reflect beam array towards the camera. A CCD camera is used to monitor change in position of the reflected beams. The custom cell was placed 26.67 ± 0.01 cm away from the camera and the cantilever is vertical to the optical table. A signal with a 660 nm wavelength was generated from the laser. The single beam passes through x- and y-etalon to generate the beam arrays with 3 by 2 beam matrix. An array of incident laser beams passes through the quartz window and electrolyte and collides on the back side of the cantilever.

The reflected beams from the surface of the substate are detected by the CCD camera. A diagram in Figure B1 demonstrates the example of the beam arrays on the CCD camera. In larger arrays, the spot spacing is measured between each beam in both the vertical and

horizontal direction and an average is taken to account for possible non-uniformities in the beam spacing. Changes in the distance between the laser beam array with time is recorded by the MOS system. The correlation between the distance between the beams and the wafer curvature that results is given by the following equation[178]:

$$\Delta\kappa = \frac{d(t)-d_i}{d_i}\frac{\cos(\alpha_i)}{2ln} \qquad (A1)$$

Where the distance between the beams at time t is given by d(t), the initial distance between the beams is given by d_i, the distance between the substrate and the CCD camera is given by l, the refractive index of the solution is given by n, and the incident angle is given by α_i[178].

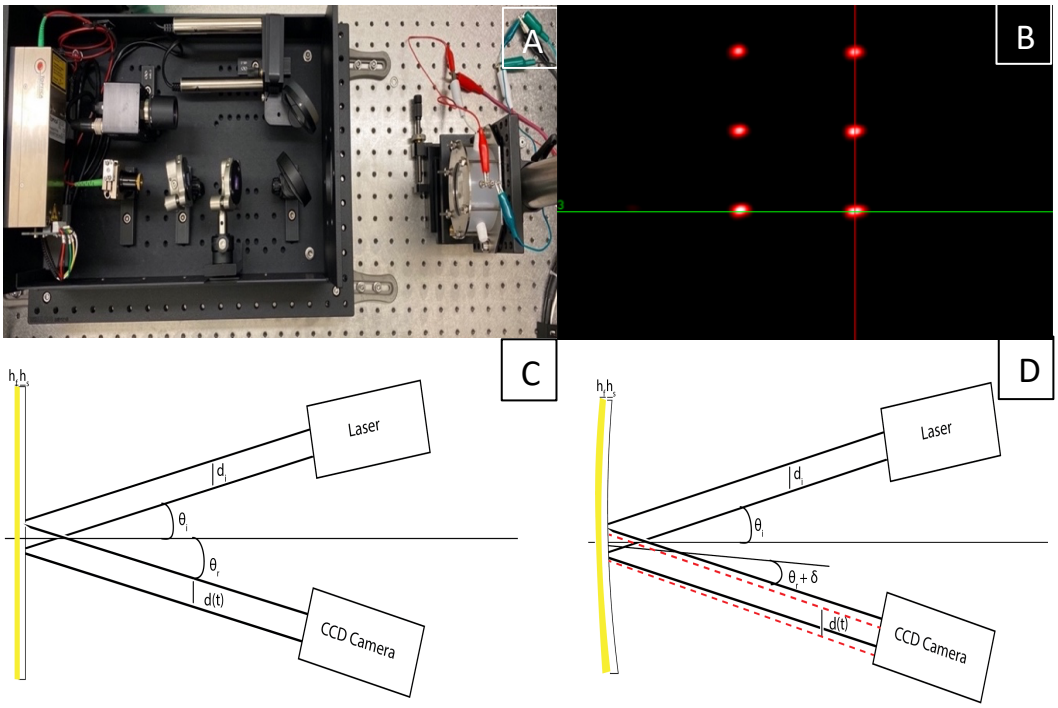

Figure A1: A) Representation of kSA MOS Components, B) Laser Beam Array, C, D) representation of the geometry associated with curvature measurements conducted on a flat and a curved substrate, respectively.

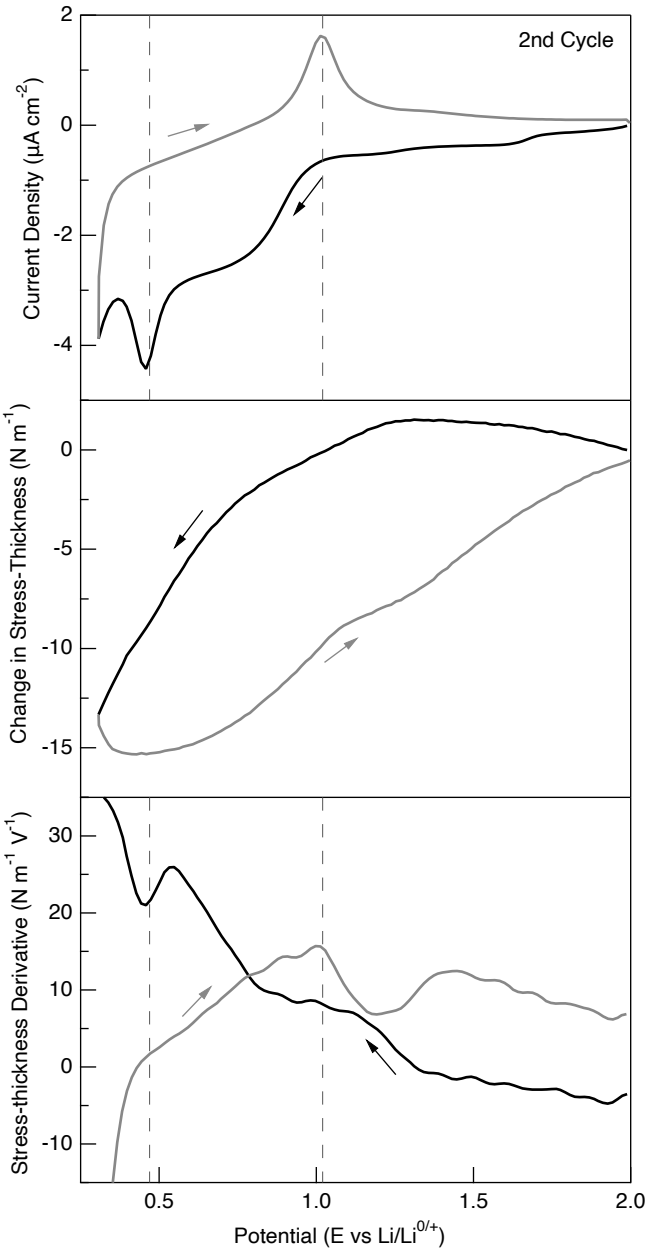

Figure A2: Cyclic Voltammetry of Au vs Li cycled in 1 M $LiClO_4$ in PC at 1mV/s during 2nd cycle. A) Current density, B) Stress generation C) derivative of the stress-thickness product versus the potential. (Argon environment).

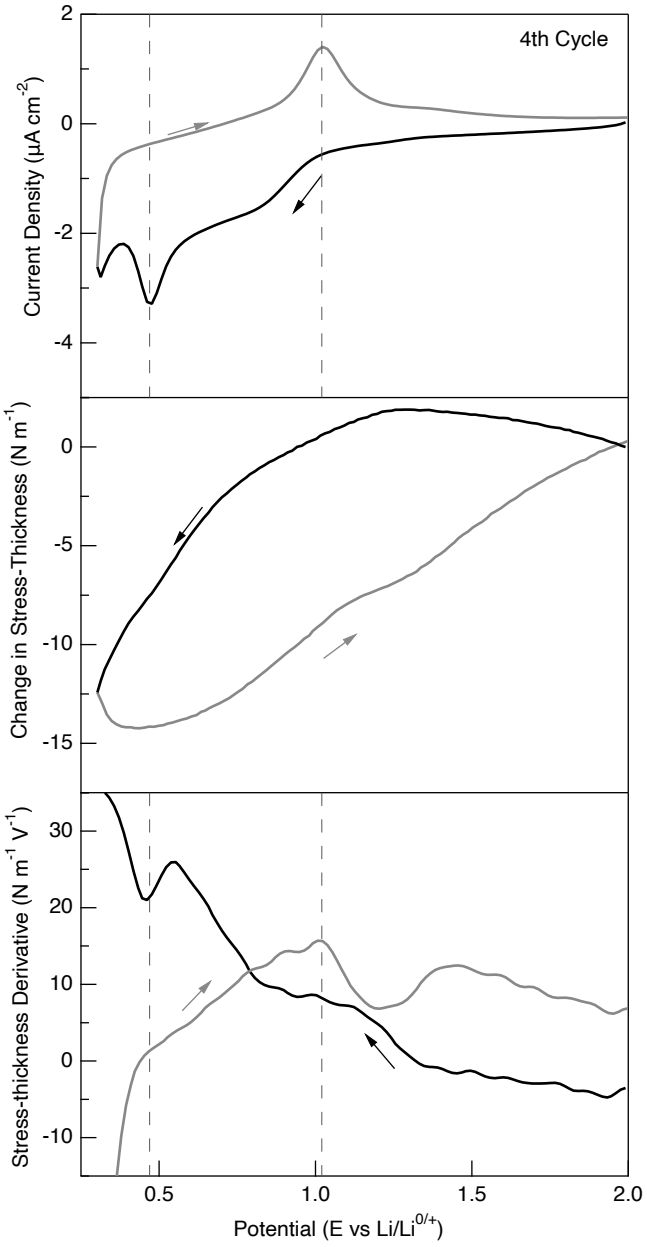

Figure A3: Cyclic Voltammetry of Au vs Li cycled in 1 M $LiClO_4$ in PC at 1mV/s during 4^{th} cycle. A) Current density, B) Stress generation C) derivative of the stress-thickness product versus the potential. (Argon environment).

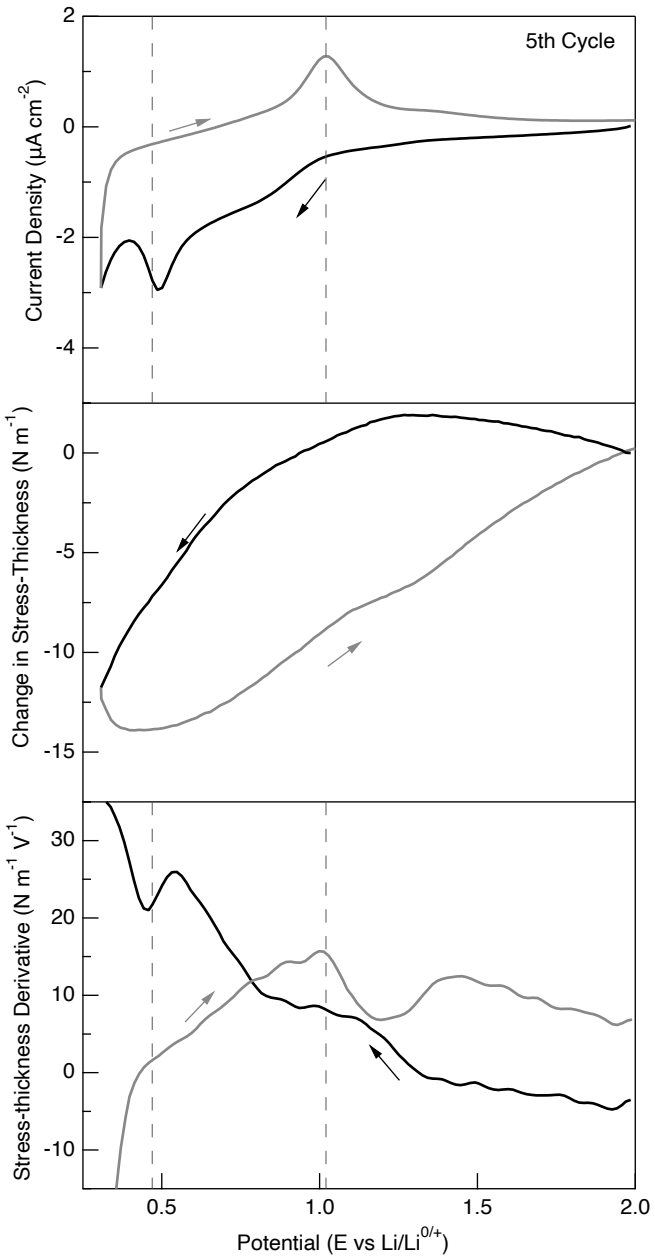

Figure A4: Cyclic Voltammetry of Au vs Li cycled in 1 M $LiClO_4$ in PC at 1mV/s during 5th cycle. A) Current density, B) Stress generation C) derivative of the stress-thickness product versus the potential. (Argon environment).

APPENDIX B

Elucidating Cycling Rate-Dependent Electrochemical Strains in

Sodium Iron Phosphate Cathodes for Na-ion Batteries

Note: The following article was published by the *Journal of Power Sources, 507, 230297, 202.1* The work concerning the modeling portion is shown here.

B1. Introduction

Recent concerns revolving around the relative scarcity and cost of lithium have resulted in increasing interest in rechargeable Na-ion batteries[197,198]. Sodium is a far more abundant material than lithium and is more evenly distributed throughout the earth crust [199]. However, Na-ion batteries suffer from low capacity retention due to chemo-mechanical degradations in the electrodes such as the decomposition of organic electrolytes on the surface of the electrode, continuous volumetric changes in the electrode constrained by current collectors, and mechanical damages in the electrodes [200,201]. Organic electrolytes decompose on the electrode surface during ion intercalation, causing the formation of a resistive surface layer on the electrode. Phase transitions commonly occur as Na ions intercalate into or out of the host lattice which creates volume mismatches. The

associated misfit strains can produce plastic deformation or amorphization in the electrode material and have negative impacts on reversible ion insertion and extraction processes [202,203]. These chemo-mechanical degradations can be further exacerbated by the larger ionic radius of Na cations (1.02 Å) and their reactivity towards electrolyte species [204]. Also, it is expected that a cathode electrode would be prone to mechanical deformations during Na-ion intercalation at faster rates due to kinetic limitation associated with slower Na-ion diffusion. Although these chemo-mechanical deformations have been intensively reported for Li-ion battery electrodes, the physical response of the electrode upon Na intercalation is expected to be different than ones during Li intercalation. Therefore, further studies are required to understand the impact of the Na ions on the mechanical stability of electrodes.

Structural and interfacial instabilities in Li-ion battery electrodes have been studied by using analytical mathematical models and various advanced characterization techniques such as electron microscopy[205–212], atomic force microscopy[213–217], in-situ XRD[218,219], and X-ray tomography[220–222], dilatometry[223,224], digital image correlation[225–227], and *in-situ* curvature measurements[137,145]. Transport-mechanics couplings in the electrified interfaces and bulk behavior of battery electrodes have been investigated by developing a continuum-based model for Li-ion batteries. These models enable the prediction of intercalation behavior of Li-ions under various factors such as surface tension, scan-rate, and morphology of the electrode[149,228–233]. The physical response of the Li-ion battery electrodes due to chemo-mechanical deformations has been characterized experimentally by monitoring stress and strain evolutions in the electrode via digital image correlation and curvature measurements. These in situ mechanical measurements shed light on complex reaction processes controlling the stability of electrode structure as well as its surface with electrolyte [137,145,225,226,234]. However, chemo-mechanical instabilities associated with interfacial and structural deformations in the cathode electrodes during Na ion intercalation are not well known.

Sodium iron phosphate was chosen as the cathode material to study rate-dependent and time-dependent deformations by utilizing in situ electrochemical strains, electrochemical techniques, and a mathematical model. Olivine-type sodium iron phosphate ($NaFePO_4$, NFP) is structurally analogous to the Lithium iron phosphate ($LiFePO_4$, LFP) electrode, which is an inexpensive and environmentally benign cathode material widely used in commercial Li-ion batteries. Due to the performance of the iron phosphate framework in Li-ion batteries, NFP has attracted attention as a cathode electrode for Na-ion batteries. NFP has a theoretical capacity of 154 mAh g^{-1}. The Michaelis group investigated the intercalation kinetics and electrochemical performance of NFP by using the electrochemical displacement technique [235,236]. The Casas-Cabanas group monitored reaction mechanisms and associated structural deformations in the NFP electrodes via in situ x-ray diffractions [237–241]. Previously, a methodology was developed to monitor the in situ electrochemical strain evolution in sodium iron phosphate electrodes using digital image correlation [225].

The goal of the study is to explore the rate and time effect on the mechanical behavior of the composite sodium iron phosphate cathode. To achieve this, the in situ strain evolution was experimentally monitored in the electrode at different rates. In situ strains were monitored using the optical, full-field digital image correlation (DIC) technique. As expected, sodium intercalation causes volumetric expansion in the composite electrode and the volume of the electrode shrinks during the removal of Na ions. Although a large amount of the irreversible strain was detected during the first cycle, strains become reversible in the subsequent cycles. Noticeably larger expansions are observed in the composite electrode when cycled at faster scan rates. Strain evolution in the composite electrode is predicted based on the elastic properties of the composite electrode and atomic-scale changes in the crystal structures. Concentration gradients and mismatch strains inside the particles are also predicted based on the transport model. The experimental and modeling studies demonstrate the mechanical penalty in the $NaFePO_4$ composite electrode at faster rates.

B2. Predicted Strains in Composite Electrode

A typical composite electrode consists of active materials, conductive carbon, and polymeric binders. Conductive carbon and polymeric binders do not intercalate with ions, their function is to provide conductive network and mechanical strength in the composite electrodes [242,243]. During battery operation, electrochemical strains in the active materials during ion intercalation (e.g. $NaFePO_4$) governs the volumetric changes in the composite electrode. Previously, the expansions in the Li-ion battery composite electrodes were estimated by considering the volumetric changes in the active particles and calculating the elastic properties of the composite electrode [244,245]. The model assumes that lithium ions are uniformly distributed in the active particles. The model only considers elastic and reversible deformations upon reversible Li^+ ion intercalation. Also, the impact of side reactions, defect formations, plastic deformations, and the formation of the cathode-electrolyte interface are not included in the model calculation. The individual active materials might show anisotropic behaviors, however, the randomly distributed active materials in the composite network leads to isotropic behaviors in the composite electrodes at the length scales considered in the model. The predicted strains showed good correlations with the experimentally measured composite strains in Li-ion batteries when the electrodes were cycled at slow scan rates [244,245]. Sodium-intercalation induced strain in the composite $NaFePO_4$ electrode is calculated by adjusting the previous composite model for Na-ion batteries. Strains in composite electrode, ϵ_{ce} is computed as,

$$\varepsilon_{ce} = \varepsilon_{NFP}\phi_{NFP} + \left(\frac{\varepsilon_{NFP}}{\frac{1}{K_{pm}} - \frac{1}{K_{NFP}}}\right)\left(\frac{1}{K_e} - \frac{1}{K_{average}}\right) \quad \text{(B1)}$$

Elastic properties of the composite electrode such as bulk modulus, K, are calculated by using open cell theory for anisotropic porous solid end S-combining rule [246]. The volumetric fraction of the NFP particles, ϕ_{NFP}, in the composite electrode is calculated by measuring the porosity of the composite electrode. The model and porosity calculations are described later. The calculation of

the strain in composite electrodes requires information about the linear strains in the NFP particles, ε_{NFP}, during Na^+ ion intercalation. Changes in the lattice parameters can be used to calculate linear strains in the NFP particles. Previously, the Casas-Cabanas group intensively investigated the

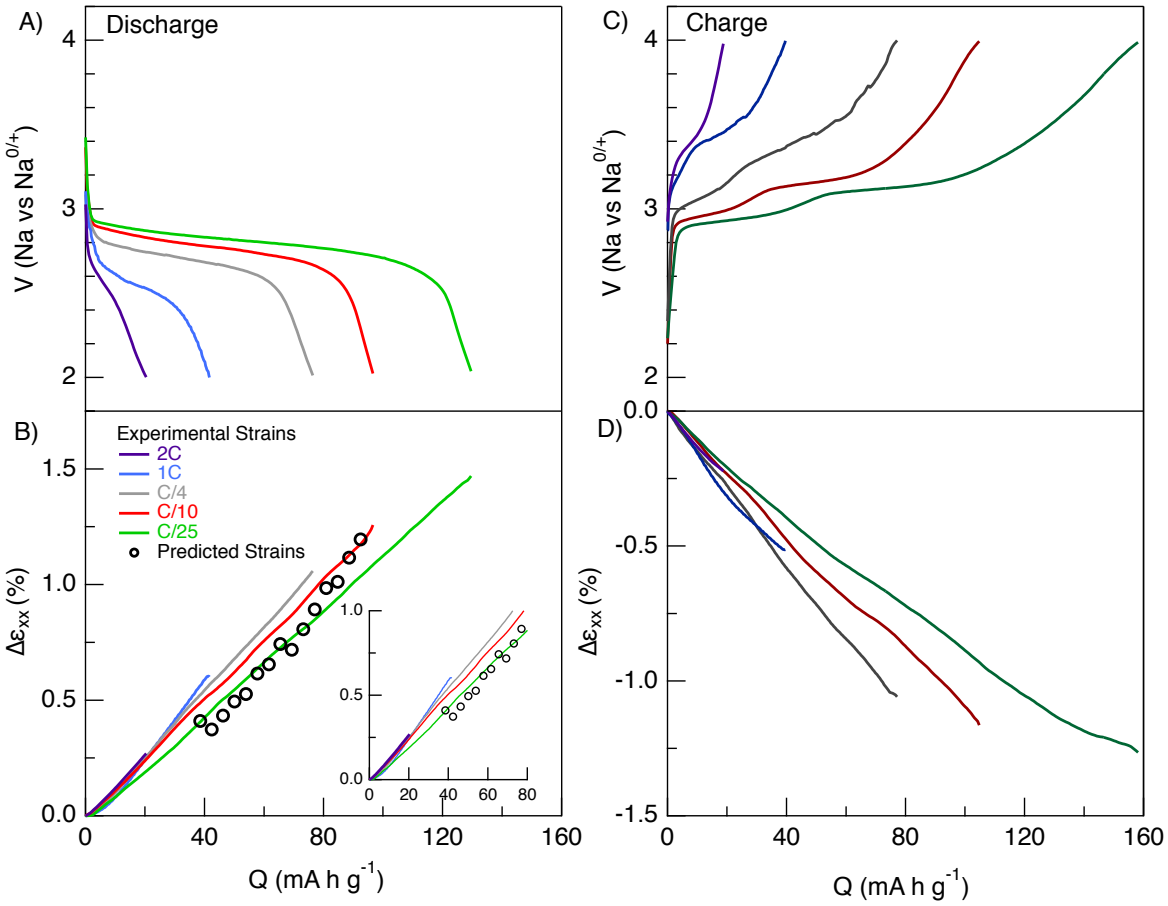

Figure B1: Voltage and strain evolution in iron phosphate composite electrode during sodium intercalation in 1 M $NaClO_4$ in EC/DMC electrolyte at different scan rates during the 4th cycle. Dotted points indicate the predicted strains calculated from the mathematical model.

structural changes in the olivine $NaFePO_4$ during charging / discharging by using synchrotron X-ray diffraction experiments [237–241]. The intensity of the low angle diffraction peaks of the phases, unit cell parameters and cell volumes is plotted with respect to Na content in the electrode discharged at C/66 rate in Figures B3 and B4 using the previously published XRD study [240].

Linear strain in the sodium iron phosphate electrodes was calculated from the changes in the cell volume of the electrode particles with respect to SOD. The predicted strains in the unconstrained composite electrode are compared with the experimentally measured strains during discharging at different scan rates in Figure 1B. In the calculations, the predicted strains were calculated between SOD of 0.25 – 0.65 to avoid the three-phase region at around 0.65 state of discharge. The corresponding discharge capacity at 0.25 SOD is 38.5 mAh g^{-1}. The predicted strains were shifted by 0.41% to provide a better comparison with the experimentally measured strains. The model predictions resemble the experimentally measured strains at slow scan rates until discharge capacity becomes 80 mAh g^{-1}. Note that the model assumes uniform sodiation of the sodium iron phosphate electrode and it is incapable of incorporating possible mismatch strains associated with large concentration gradients at faster scan rates. We hypothesize that the diffusion-limited concentration profile of Na ions in the electrode particles causes mismatch strains at faster scan rates. To further investigate, we calculate the concentration gradients and mismatch strain profiles in the electrode particle using Fick's law.

B3. Predicted Na Concentration and Mismatch Strains in the Electrode Particle

An analytical model based on Fick's law and elastic deformation was developed to stimulate the concentration profile of Li ions and stress generation in various shapes and orientations of Li-ion battery electrodes[203,228,230,231,247–249]. We adopted previous diffusion-mechanics models of Li-ion batteries into Na-ion batteries to compute the Na concentration gradient and mismatch strains in spherical $NaFePO_4$ particles. In the olivine $NaFePO_4$ structure, FeO_6 octahedra connect with neighbor FeO_6 by sharing corner in the ab plane, whereas PO_4 tetrahedra shares corners and edges with the FeO_6 octahedra. The structure provides open channels along the a-axis and b-axis for Na ions. We consider a simple problem of diffusion of Na ions within the sphere shape of particles with the radius, r. From SEM images, the average radius of the particles was around 125 nm. The concentration of sodium in the particle is governed by time-dependent Fick's law [231];

$$\frac{\partial c}{\partial t} = \frac{D}{r^2}\frac{\partial}{\partial r}\left(r^2 \frac{\partial c}{\partial r}\right) \tag{B2}$$

The primary driving force for sodium diffusion is the concentration gradient. GITT measurements were performed to calculate the diffusion coefficient of the sodium in the $NaFePO_4$ particles (Supp. Information). The diffusion coefficient varies between $1 \times 10^{-14}\ cm^2/s$ and $1 \times 10^{-17}\ cm^2/s$ during intercalation of Na ions. In the calculations, we assume constant diffusivity of $2 \times 10^{-15}\ cm^2/s$ and the stress-induced diffusion is neglected. Initial and boundary conditions are given by;

$$C(r, 0) = 0 \text{ for } 0 \leq r \leq R \tag{B3}$$

$$D\frac{\partial C(0,t)}{\partial t} = 0 \text{ for } t \geq 0 \tag{B4}$$

$$D\frac{\partial C(R,t)}{\partial t} = \frac{I}{F} \text{ for } t \geq 0 \tag{B5}$$

At the surface of the electrode, current density, I is constant under galvanostatic discharging and it can be defined with the galvanostatic discharge rate as $I = (C - rate)\frac{\alpha\rho R}{3}$ where α and ρ denote theoretical capacity and density of the electrode, respectively. The C-rate represents the amount of time it takes to discharge the battery with respect to its theoretical capacity. C_{max} is the maximum concentration of sodium in the $NaFePO_4$. In Figure 1B, the state of discharge at the end of the discharge was 0.27, 0.50, 0.62, and 0.84 when the electrode was cycled at 1C, C/4, C/10, and C/25 rates, respectively. To simulate the concentration gradients and mismatch strains, the electrode particles are discharged until the average SOD in the particle reached the experimentally observed SOD for four different scan rates in Figure B2.

As a reference point, the concentration profile of sodium is also computed when cycled at C/100 until 0.95 SOD. The concentration profile of sodium inside the electrode particles is estimated by solving the partial differential diffusion equation using the MATLAB PDEPE toolbox.

Figure B2 shows the distribution of sodium at different C-rates. At slower rates (C/100 and C/25), sodium is almost uniformly distributed along the particle radius. When the scan rate increased further, the concentration of sodium near the particle surface differs significantly from the concentration in the center of the particles. As a result, a large sodium concentration gradient is observed near the electrode surface at faster rates. The deformation mismatch due to the inhomogeneous distribution of sodium inside the electrode particle was also calculated by following the previous elastic model developed for Li-ion batteries [228]. Mismatch strains are calculated as:

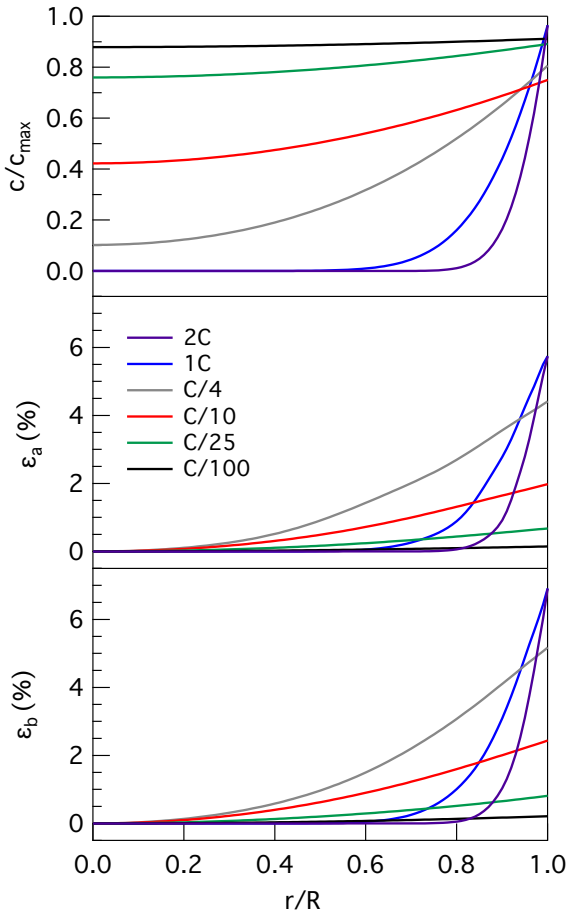

Figure B2: Na Concentration and Mismatch Strains in Electrode Particle: The sodium concentration profiles and the mismatch strains at five different scan rates. In the calculations, it is assumed that the electrode particles are discharged until 0.15, 0.27, 0.50, 0.62, 0.84 and 0.9% state of discharge for 2C, 1C, C/4, C/10, C/25 and C/100. The state of discharge values for each rate is chosen based on experimentally measured electrode capacity in Figure 5.

$$\varepsilon(r) = \frac{l(r) - l|_{r=0}}{l|_{r=0}} \tag{B6}$$

Concentration dependent-lattice parameters among the a-axis and b-axis are used to calculate strains. Shortly, the estimated concentration profiles throughout the radius of the electrode particle were converted into radius and time-dependent SOD and match with the lattice parameter in the a-axis and b-axis from the Figure 3B. Steep concentration gradients at faster scan rates result in the generation of large mismatch strains in the electrode particle.

The average concentration in the electrode particle ($\bar{C}_{ave}$, where $\bar{C}_{ave} = C/C_{\max}$), average mismatch strains in the particle along a-axis ($\varepsilon_{a,ave}$) and b-axis ($\varepsilon_{b,ave}$) are calculated from the simulation and tabulated in Table 1B. Average values are calculated via $\Phi_{ave} = \frac{\int_0^R \Phi dr}{\int_0^R \overline{dr}}$ where $\Phi = \bar{C}_{ave}, \varepsilon_a \; or \; \varepsilon_b$. The average predicted Na concentrations in the electrode particle at different rates are in good agreement with the experimentally measured Na content in the composite electrode in Figure 2B. The average mismatch strain evolution per charge is greater in magnitude when the electrode is cycled at faster rates. These mismatch strains in the electrode particle leads to additional macroscopic expansions of the composite electrode at faster rates.

Table B1: Average concentration in the electrode particle $\bar{C}_{ave}$, and mismatch strains in the particle along a-axis ($\varepsilon_{a,ave}$) and b-axis ($\varepsilon_{b,ave}$).

C-rates	2C	1C	C/4	C/10	C/25	C/100
$\bar{C}_{ave}$	0.15	0.30	0.53	0.63	0.84	0.89
$\varepsilon_{a,ave} / \bar{C}_{ave}$	6.17	6.19	5.21	2.08	0.53	0.10
$\varepsilon_{b,ave} / \bar{C}_{ave}$	6.91	7.00	5.95	2.55	0.63	0.14

B4. Discussion

Rate-dependent strain rates with respect to the capacity in Figure B1 are associated with the generation of mismatch strains in the electrode. Mismatch strains, $\varepsilon_M(v)$, can be generated due to rate-dependent concentration gradients in the electrode particle and volume mismatch between two separate phases in the electrode. The energy accommodation during mechanical deformations in the electrode widens the potential gap between the electrochemical redox reactions, which leads to higher potential hysteresis[170]. Zhu and Wang calculated the strain accommodation energy for $LiFePO_4$ electrodes with 40-nm and 100-nm particle sizes. The bigger particles require large potential hysteresis to accommodate the volume differences between Li-rich and Li-poor phases [250]. Synchrotron X-ray diffraction and pair distribution function analysis suggest $NaFePO_4$ accommodates discontinuous volume changes in the electrode by forming short-range amorphous phases [202]. Operando synchrotron study also suggested the formation of mismatch strains on $NaFePO_4$ cathodes induces cost of mechanical energy, which causes larger potential hysteresis between redox reactions [251]. The analytical model predicted sharper concentration gradients and localized strain generation near the electrode surface during Li-ion intercalation electrode [149,228–233]. In situ stress measurements and finite strain model demonstrated local stress gradients near the Si thin film electrode surface due to sharp concentration gradients near surface [252,253]. The transport model only simulates the rate-induced concentration gradient within the solid solution (Figure B2). The model predicts sharp concentration gradients of Na near the electrode surface at higher rates, which contributes to greater mismatch strains (Table B1). It should be noted that large concentration gradients impede the volume mismatch between two separate phases in the electrode. Although predicted strain values do not incorporate the phase separation factor, it demonstrates the contribution of sharp concentration gradients at faster rates on the mismatch strains.

B5. Conclusions

A better understanding of the rate effect on electrode mechanics is required to develop new electrodes with better rate-capabilities. In this work, the impact of scan rate on electrochemical strain generations in the $NaFePO_4$ composite cathode for Na-ion batteries was studied. Digital image correlation was used to monitor strain generation in the composite cathode during cycling at different scan rates. Experimental strain measurements were compared with the predictions from an analytical model for composite electrodes based on uniform elastic deformations and intercalation-induced structural changes in the NFP particles. A transport-mechanics model is developed to predict the concentration profile of Na in the electrode particles and associated mismatch strains at different scan rates. When considering commercial electrodes being constrained by current collectors and battery packing, these constrained electrodes will be more prone to mechanical degradations at faster rates due to larger electrochemical strains. Mechanical instabilities in the electrode particles will shorten the lifetime and worsen the performance of the battery electrodes.

Acknowledgments: This work was supported by the U.S. Department of Energy, Office of Science, Basic Energy Sciences (Award number DE-SC0021251). MCC and DS are grateful to the Basque Government through the Elkartek grants CICe2019 and CICe2020 (KK 2020/00078), to Ministerio de Economía y Competitividad through NIB-MOVE grant (PID2019-107468RB-C22).VM acknowledges funding as part of the Joint Center for Energy Storage Research, an Energy Innovation Hub funded by the U.S. Department of Energy, Office of Science, Basic Energy Science.

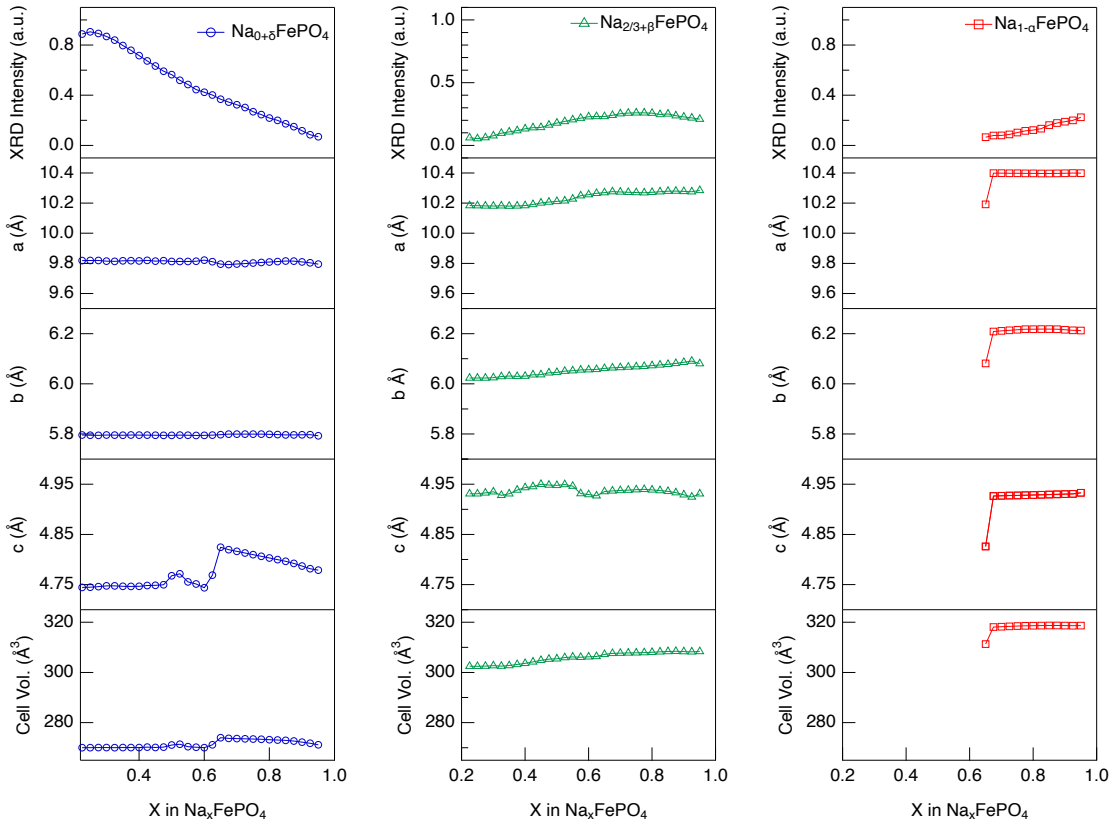

Figure B3: The lattice parameters for each direction of the unit cell, as well as the total change in the unit cell volume were calculated by using *in-situ* XRD during the sodiation of Na_xFePO_4 at C/66. The figure is regenerated from the previous publication [240].

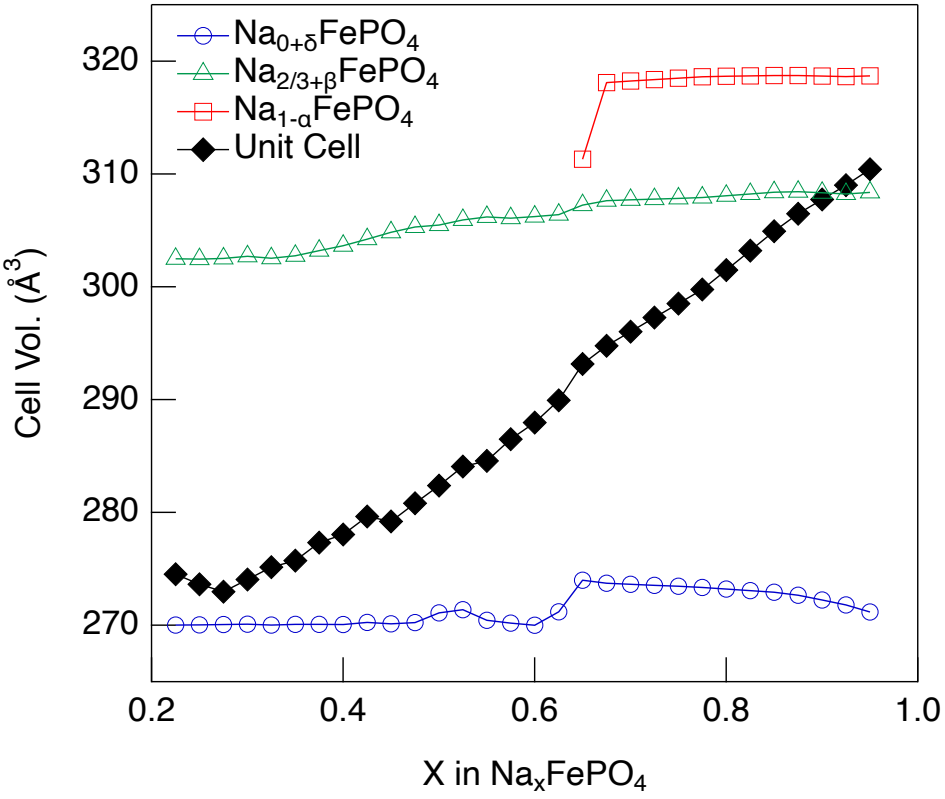

Figure B4: The change in the total unit cell volume during sodiation at C/66 is compared to the change in the unit cell volume change for each phase of Na_xFePO_4. This figure is regenerated from a previous publication[240].

B6 Predicting Strains in Composite Electrode

To investigate the strain on an unconstrained $NaFePO_4$ electrode during sodiation, the properties of the composite electrode were analyzed by assuming that the $NaFePO_4$ composite consists of a porous matrix of conductive carbon, Super P, and CMC binder [226].

Table B2: Material Properties of the Composite Electrode Matrix

Material Properties of the Composite Electrode Matrix				
Material	Fraction of Total Mass	Density (g/cm^3)	Elastic Modulus (GPa)	Poisson's Ratio
$NaFePO_4$	0.8	3.53 [254]	$84x10^9$	0.25 [255]
CMC binder	0.1	1.6 [256]	$1.2x10^9$	0.45 [226]
Super P	0.1	1.9 [257]	$32.47x10^9$	0.315 [226]

The lower bound of the effective shear modulus containing both carbon black particles and CMC binder where K_m is the bulk modulus of the matrix of carbon black and CMC binder particles. The bulk modulus of the carbon black is K_{cb} and that of the CMC binder is K_{cmc}. G_m is the shear modulus of the matrix of carbon black and CMC binder particles. The shear modulus of the carbon black is G_{cb} and that of the CMC binder is G_{cmc}.

$$\frac{1}{K_m} = \frac{\phi_{m,cc}}{K_{cc}} + \frac{\phi_{m,cmc}}{K_{cmc}} \tag{B7}$$

Lower bound of the bulk modulus containing both carbon black particles and CMC binder is:

$$\frac{1}{G_m} = \frac{\phi_{m,cc}}{G_{cc}} + \frac{\phi_{m,cmc}}{G_{cmc}} \tag{B8}$$

Where:

$$\phi_{m,cmc} = \frac{\phi_{cmc}}{\phi_{cmc}+\phi_{cc}} \tag{B9}$$

$$\phi_{m,cb} = \frac{\phi_{cc}}{\phi_{cmc}+\phi_{cc}} \tag{B10}$$

K_{pm} is the bulk modulus of a porous matrix of with solid components carbon black and CMC binder.

$$K_{pm} = \left(\frac{1}{3(1-2\nu_{pm})}\right)\left(\frac{K_m G_m}{3K_m+G_m}\right)\left(\frac{\rho_{pm}}{\rho_m}\right)^2 \tag{B11}$$

Where the densities of the porous and solid matrices are:

$$\rho_m = \phi_{m,cc}\rho_{cc} + \phi_{m,cmc}\rho_{cmc} \tag{B12}$$

$$\rho_{pm} = \phi_{pm,cc}\rho_{cc} + \phi_{pm,cmc}\rho_{cmc} \tag{B13}$$

The volume fractions of the conductive carbon and the CMC binder in the porous matrix is given by:

$$\phi_{pm,cmc} = \frac{\phi_{cmc}}{\phi_{pm}} \tag{B14}$$

$$\phi_{pm,cb} = \frac{\phi_{cc}}{\phi_{pm}} \tag{B15}$$

The total volume fraction of the CMC, conductive carbon, and the porosity in the composite electrode is:

$$\phi_{pm} = \phi_{cc} + \phi_{cmc} + \phi_p = 1 - \phi_{NFP} \tag{B16}$$

The bulk modulus of the composite electrode [246] for $NaFePO_4$ particles, K_e is:

$$K_{ce} = \frac{K_{pm}(1+\phi_{NFP}\xi_l\chi)}{1-\phi_{NFP}\Psi\chi} \tag{B17}$$

Where:

$$\chi = \frac{K_{NFP}-K_{pm}}{K_{NFP}-\xi_l K_{pm}} \tag{B18}$$

$$\Psi = 1 + \frac{\phi_{NFP}\phi_{pm}(1-\gamma\phi_{pm})(K_{NFP}-K_{pm})\left(\frac{2(1-2\nu_{pm})}{(1+\nu_{pm})} - \frac{2(1-2\nu_{NFP})K_{NFP}}{(1+\nu_{NFP})K_{pm}}\right)}{K_{NFP}+\frac{2(1-2\nu_{NFP})K_{NFP}}{(1+\nu_{NFP})K_{pm}}(\phi_{NFP}K_{NFP}+\phi_{pm}K_{pm})} \tag{B19}$$

$$\gamma = \frac{2\lambda^*-1}{\lambda^*} \tag{B20}$$

The linear strain during sodiation of the composite electrode is:

$$\varepsilon_{ce} = \epsilon_{NFP}\phi_{NFP} + \left(\frac{\varepsilon_{NFP}}{\frac{1}{K_{pm}}-\frac{1}{K_{NFP}}}\right)\left(\frac{1}{K_e} - \frac{1}{K_{average}}\right) \tag{B21}$$

Where the average linear strain during sodiation is:

$$\varepsilon_{average} = \varepsilon_{NFP}\phi_{NFP} + \phi_{pm}\varepsilon_{pm} \tag{B22}$$

And the average bulk modulus of the composite electrode is:

$$\frac{1}{K_{average}} = \frac{\phi_{NFP}}{K_{NFP}} + \frac{\phi_{pm}}{K_{pm}} \tag{B23}$$

Table B3: Nomenclature for Equations

Abbreviation	Definition
NFP	Sodium Iron Phosphate ($NaFePO_4$)
ce	Composite Electrode
cc	Conductive carbon
cmc	Carboxymethyl cellulose binder
pm	Porous matrix

APPENDIX C

Standard Operating Procedure for the Operation of the kSA Multi-beam Optical Sensor (MOS) Curvature Measurement Technique

Brief Experimental Study

The kSA MOS system will be used to monitor the stress-induced curvature of a reflective substrate. An example of a cathode material used is a 50 nm Au thin film that has been deposited onto borosilicate glass.

Procedure Description

The kSA MOS system consists of a laser (AIGaInP Diode) with a focusable lens, an x etalon, a y etalon, a mirror with servo control, a lens, and a CCD camera. Each of these components are contained within the kSA MOS chamber.

Procedure

- Verify that all power cables connected into the back of the MOS are secure and also connected to the computer.

- Verify that the optical table is balanced by using the balancing tool. The balancing tool should be moved along the front and the side of the table and to make sure it is completely balanced.
- The power supply to the MOS box should then be turned on (red switch on the back of the box) and the top cover of the MOS should be removed.
- Using the kSA MOS software, the laser and the CCD camera should be turned on by using the input/output devices tab shown in Figure C1.
- The maximum power that the laser can operate at is 75 mW, but a maximum of 70 mW is recommended. For the CCD camera, the exposure time can be controlled. The maximum exposure time is 5.00 ms, but an exposure time below 1.00 ms is recommended to increase the life of the CCD camera. The camera exposure is set to 1.00 ms, but when taking a curvature reference, the exposure time automatically adjusts to the optimized exposure level.

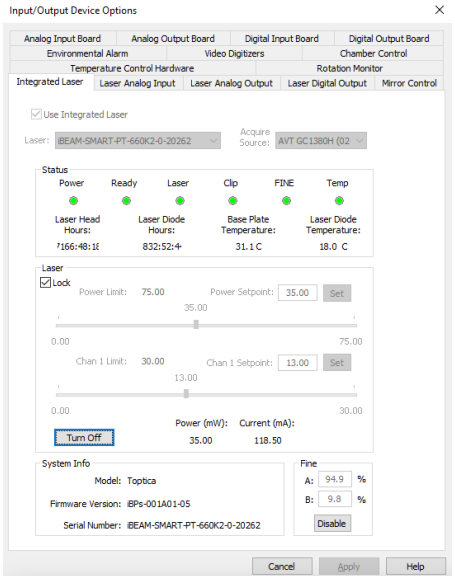

Figure C1: Turning on and Setting Laser Power

- The custom cell should be completely secured to the aluminum breadboard on the optical table. Information about the custom cell can be found in Appendix D.
- After the laser power and the CCD camera have been turned on, using Figure C1 as a reference, remove the x etalon to increase the intensity of the beam that will reflect off the cantilever surface. The x etalon is shown below in Figure C2.

  ***Note:** Decrease the laser power to 20 mW or less after removing the x-etalon to decrease the intensity.

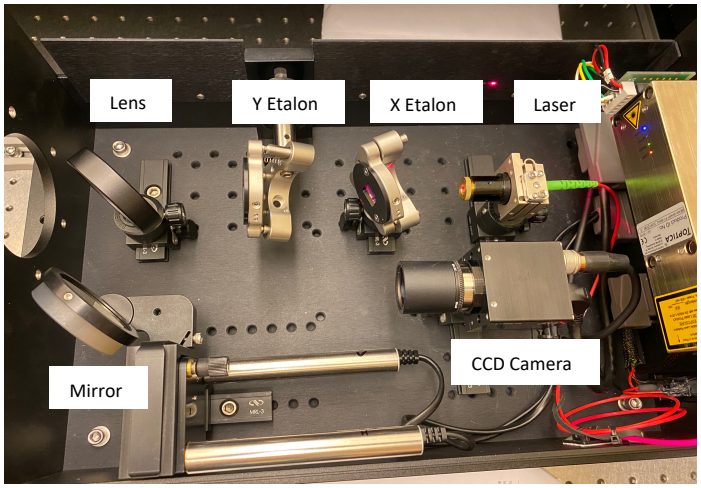

Figure C2: kSA MOS board layout

- Align the custom cell so the laser beam is hitting the center of the cantilever. The microscope slide can be used to help with this.
- The translation stage, along with the knobs located on the tilt/rotation stage can be used to position the 3 by 2 beam array into the center of the CCD camera. After the 3 by 2 beam array is in the center of the CCD camera and is shown on the MOS program (as shown in Figure C3), the x etalon should be placed back onto the MOS.

  *The x etalon should always remain at around a 45 degree angle from the laser so the laser beam does not reflect back into the laser (this could cause damage to the laser).

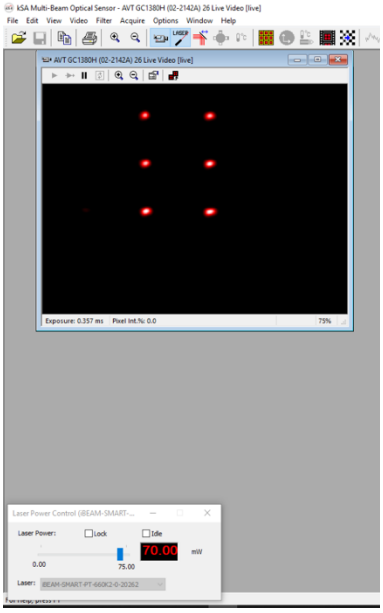

Figure C3: Turning on the CCD Camera

- The x etalon should be positioned so that two beams (horizontal to each other) are passing through it by using the microscope slide.
- After positioning the x etalon, focus mode should be used as shown in Figure C5. The beams should be aligned by using the steps below:
    - A on the x etalon adjusts the horizontal spacing between the beams.
    - B on the x etalon rotates the angle of the beam array so the beam array will align in the horizontal direction.
    - A on the y etalon rotates the angle of the beam array so the beam array will align in the horizontal direction.
    - B on the y etalon adjusts the vertical spacing between the beams.

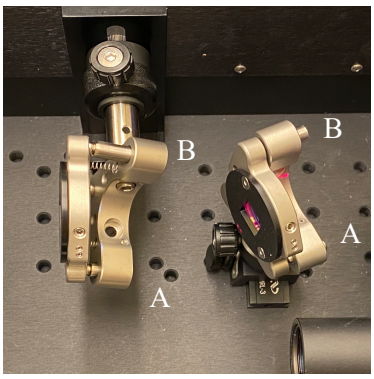

Figure C4: X and Y Etalon adjustments

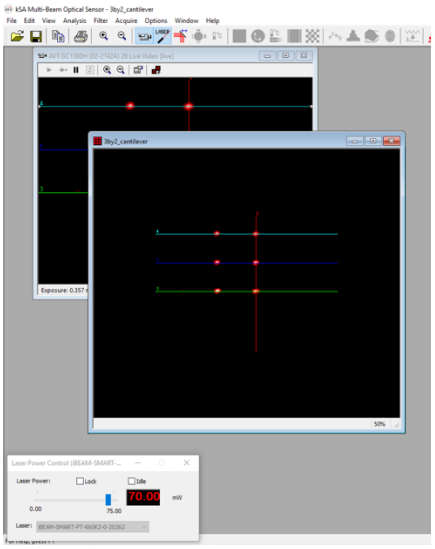

Figure C5: Focus Mode

- The MOS box should always be covered. To accomplish this, two screws should be placed (one in the center hole on both sides) on the side of the top cover of the MOS box and the Arbin cables should be placed on the custom cell. The optical table should be covered with the foam top cover and the black curtain should be placed over it before calibrating the mirror. Small changes like these can influence the position and clarity of the beams slightly.
- The beam array should be aligned in both the vertical and horizontal directions by using focus mode. The mirror can be calibrated by selecting the mirror icon. The beams should resemble the beam array shown in Figure C3.

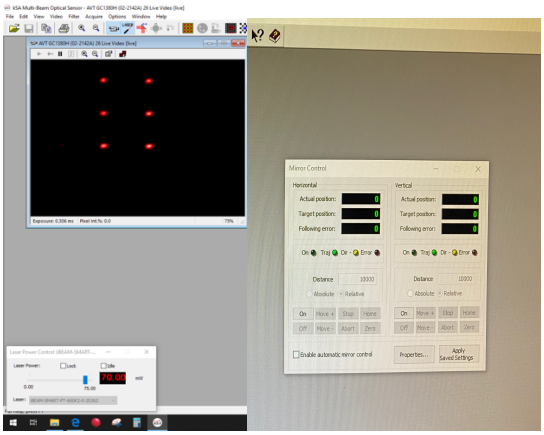

Figure C6*:* Mirror Calibration

- The servo control for the mirror in both the vertical and horizontal directions should be turned on.
- A snapshot of the beam array in the CCD Camera should be taken.

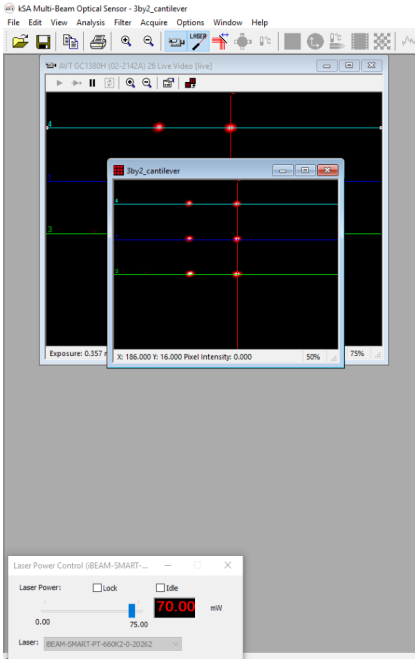

Figure C7: Mirror Calibration

- After taking a snapshot of the beams, the "Histograms and Statistics" should be used to record the centroid location of the most intense beam (both the x and y coordinates). The

intensity of the beams only varies slightly. After the (x,y) coordinate is recorded, the snapshot can be closed.

- The horizontal direction of the mirror should then be moved by 10,000 units (using the Move+ icon) and another snapshot should be taken.
- After taking the snapshot, “Histogram and Statistics” should be selected again and the new centroid location of the beam should be recorded (x value only, the y value does not change).
- The absolute value of the difference between the x values between the original centroid location and the new centroid location should be recorded. Label the difference X.
- To obtain the units/pixel(x), calculate -10,000/X and record this value. It should be a negative number.
- The “Home” should then be selected on the horizontal direction of the mirror to return the mirror to its original position.
- The vertical position of the mirror should then be moved 10,000 units (using the Move+ icon) and another snapshot should be taken.
- After taking the snapshot, “Histogram and Statistics” should be selected again and the new centroid location of the beam should be recorded (y value only, the x value does not change).
- The absolute value of the difference between the x values between the original centroid location and the new centroid location should be recorded. Label the difference Y.
- To obtain the units/pixel(y), calculate 10,000/Y and record this value. It should be a positive number.
- The “Home” should then be selected on the vertical direction of the mirror to return the mirror to its original position.

- The “Properties” icon in the mirror control tab (Figure C6) should then be selected the units/pixel for both x and y should be inputted.
- The Mirror Control should then be closed and Curvature Mode should be opened.

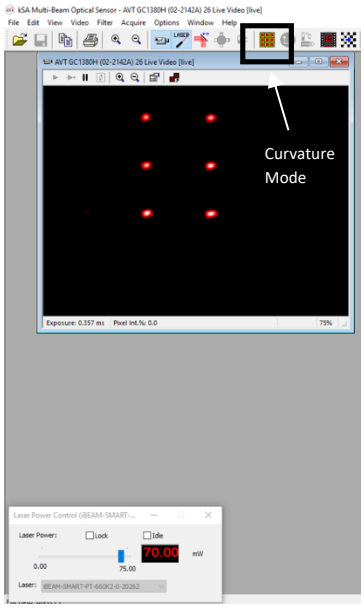

Figure C8: Curvature Mode Tab

- Under “Run Name” on the Curvature Mode screen (shown in Figure C9), name the experiment.
- “Detect” should be selected on the curvature tab (a box should surround each laser beam).
- “Reference” should then be selected (as shown on Figure C9), followed by “Acquire new reference”. Then select “okay” to close the reference window.

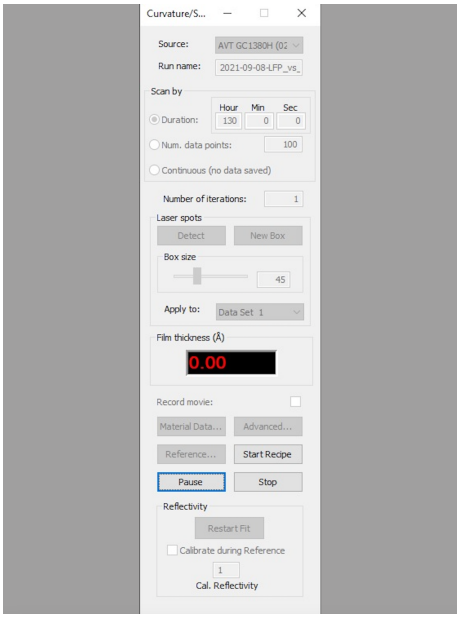

Figure C9: Curvature Mode Screen

- The “continuous” icon should be selected followed by “start”.
- Taking the reference lasts approximately 8 seconds. After the reference is taken, the “reference” icon should be selected again and the reference file should be loaded.
- The “acquire new reference” icon should not be selected after loading the new refernce file.
- The duration of the experiment can then be set and the experiment can then be started.
- After the experiment has started, the “Spot Spacing Plot” and the “Real-Time Averaged MOS Data” can be viewed under the “View tab”.

Important Notes

- The MOS program should be started 10 seconds before the Arbin computer by setting a timer for ten seconds after the stress measurements begin so the time delay between the two computers is clearly documented.
- The MOS should always be covered with its top cover and two screws should be placed (one in the center on both sides) on the MOS box. The optical table should also be

covered with the foam covering and the black curtain should be placed over it before calibrating the mirror. Small changes like these can influence the position and clarity of the beams slightly.

- The intensity of the laser should be turned down to 20 mW or lower when the x etalon has been removed due to the high intensity of the beam and the class of the laser.
- The "Laser is on sign" should be placed on both doors before running an experiment.
- The optical components often become contaminated with dust particulates. NEVER attempt to clean the optical surface alone. Clean the surface of the CCD Camera, mirror, etalons, and lens with either ultra-high purity (UHP) nitrogen or argon if any dust particulates build up on the surface. Never use any chemicals, Kimwipes, or compressed air to clean optics.

Work Location/Precautions

Never overextend the cables or place anything on top of them. A Class 3B laser diode will be used for the duration of the experiment. Always wear laser goggles when working with the laser and place the "laser is on" sign on the door before starting an experiment. The maximum output power is 70 mW and the wavelength is 660 nm. According to the Oklahoma State Institutional Laser Policy, having a Class 3B laser requires approval from the OSU laser safety committee and the proper training must be administered.

Important Safety Note:

- Properly fitting laser safety goggles should be worn at all times when working with the laser. The laser beam should never be looked at directly and the laser safety goggles located beside the optical table in room 238 should be worn when working with the laser. The laser beam should always be contained within the optical table walls in order to avoid possible exposure to incident beams. Exposure to laser beams could cause permanent eye damage.

Equipment

AIGaInP Laser Diode- 660 nm wavelength, 70 mW

- **GHS categories**: Laser Radiation, Avoid Exposure
- **GHS Symbols:** Laser Radiation Hazard

CCD Camera

- **GHS categories**: Electrical Shock Hazard
- **GHS Symbols:** Electrical Shock Hazard

APPENDIX D

Standard Operating Procedure for the Assembly of the Custom Electrochemical Cell

Brief Experimental Study

A custom electrochemical cell will be used to perform in situ curvature measurements. An optical window is used so that a laser beam array can penetrate the surface of the cathode electrode and monitor the curvature. This custom cell will be mounted onto a breadboard and placed on the optical table in room 238. The kSA MOS system will be used to monitor the stress-induced curvature of the cathode sample that is used.

Description of Procedure

The custom electrochemical cell will be assembled in room 236 and will then be placed on the optical table in room 238. The cathode electrode will be placed in the cell outside of the argon-filled glovebox. Then the cell will be vacuumed and the electrolyte along with the anode material (typically lithium foil) will be placed inside the cell inside the glovebox. The custom cell will be sealed inside the glovebox and will then be removed.

Procedure

- Verify that the correct O-rings and the current collectors are being used. This can be determined by looking at material compatibility charts. The current collectors used for the working and counter electrodes are different widths. The reason behind this will be discussed further below. The O-rings used must be compatible with the choice of solvent. There are two different sizes of O-rings that will be used for the custom cell.
- Verify that all components of the custom cell have been cleaned by using a triplicate washing procedure (acetone, isopropyl alcohol, and ultrapure water respectively). After all components have been cleaned, the cell will be placed in the oven and heated to 100 °C for one hour to make sure that all the components have been thoroughly dried.
- After all the components have been cleaned, place the O-rings inside the custom cell. One O-ring will be placed inside each current collector as shown below in Figure D1. Two O-rings will be placed inside the O-ring groove that is located on both sides of the custom cell. The optical window will be placed above these O-rings on each side of the cell. Also, an O-ring will be placed inside the O-ring groove on the front stainless-steel plate (that secures the top optical window closest to the cantilever) and the back stainless-steel plate (that secures the optical window closest to the lithium foil at the back of the cell).

Figure D1: Images of the O-rings used for the current collectors (top), the cell (bottom), and the stainless steel plates (bottom)

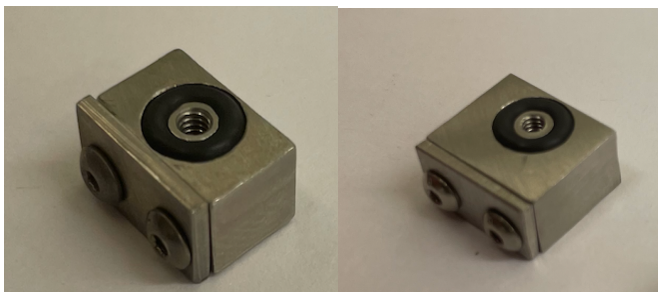

Figure D2: Images of current collector that will be used for the lithium foil (left) and for the cantilever (right)

- After the O-rings are placed inside the cell, the cantilever should be prepared. The dimensions of the cantilever should be 3.9 mm wide and 22 mm long. These dimensions should be measured using a vernier caliper. The cantilever samples are 22 mm by 22 mm squares. They will be cut to 3.9 mm by 22 mm samples by using a diamond point pen shown below. The samples should be cut with the diamond tip pen on a clean surface. If the surface of the cantilever gets scratched during preparation, discard the sample and repeat the process.

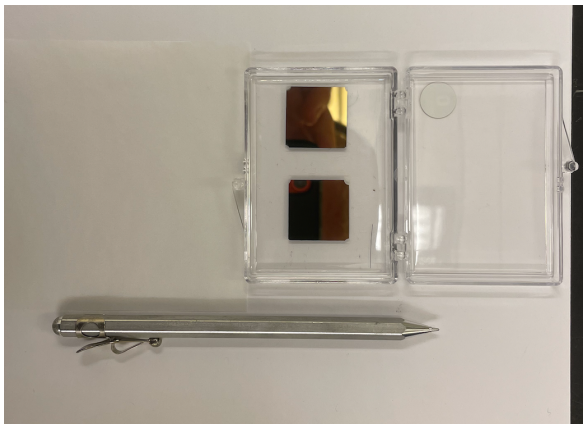

Figure 3D: Image of the Au cantilever samples and the diamond tipped pen

- After cutting the cantilever, place it inside the wide current collector as shown in Figure D6. The screws should be slightly loosened so the cantilever can be placed under the top cover of the current collector. The side containing the Au thin film should face away from the screws on the current collector. After the Au cantilever is positioned inside the two

screws, the screws should be tightened with a similar amount of force. Examine the current collector to make sure it is properly tightened.

- The stainless-steel rod for the current collector should then be screwed into the top of the current collector from the outside of the cell. This will require the current collector to be held inside the cell while the stainless-steel rod is being screwed into the top. After the stainless-steel rod has been screwed in, a stainless-steel cap will be placed over the rod on the outside of the cell to hold the current collector into place.
- The Au thin film should face the back of the cell where the lithium foil will be placed. After placing the cantilever inside the cell, the PTFE filler should be placed inside as shown in Figure D6. The PTFE filler is used to decrease the volume of electrolyte that is required to immerse the cantilever inside the cell.
- After placing the cantilever and PTFE filler inside the cell, place the PTFE tape shown in Figure D4 onto either the PTFE plug (for Li-ion) or the PTFE barbed adapter (for Li-O_2). This provides an extra seal to make sure that no ambient air enters the cell.

Figure D4: Image of the PTFE tape used to wrap the PTFE plugs or barbed adapters

- For the Li-O_2 battery, fluorinated ethylene propylene (FEP) tubing is placed inside the barbed adapter for better control of the oxygen inside the cell. Polypropylene tubing will be placed on the outside of the cell over the barbed adapters as shown in Figure D5. This tubing is not exposed to the electrolyte. It is only exposed to oxygen.

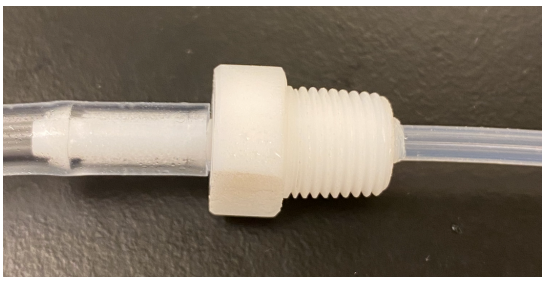

Figure D5: Image of the PTFE barbed adapter with tubing

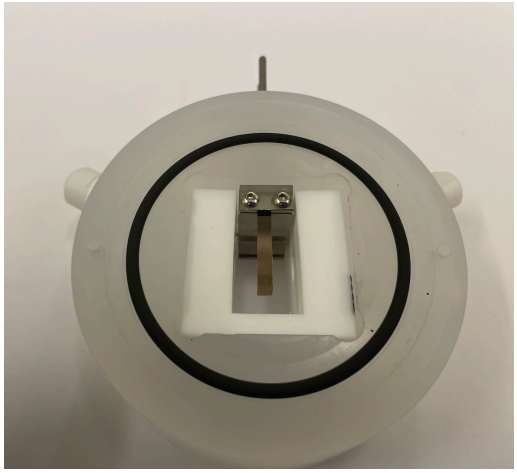

Figure D6: Image of the assembled cell outside of the glovebox in lithium-ion battery configuration (due to the PTFE plugs)

- After placing the PTFE adapter or plug into the cell, all cell components will be placed inside of the argon-filled glovebox. This includes the stainless-steel front and back plates (with the O-rings inserted), the two quartz windows, the tubing and the tube clamps (for Li-O_2 only), the stainless-steel rods that are attached to the top plate and connect to the bottom plate to seal the cell, and one PTFE plug or adapter (only one has been screwed into the cell). This piece will be screwed inside the cell after the electrolyte is inserted.
- After vacuuming the custom cell components inside of the glovebox antechamber, the components should be taken out of the antechamber by opening the antechamber door while inside the glovebox.

  *Nitrile gloves should always be worn before using the glovebox

- After the components are removed from the antechamber, the lithium foil will be placed inside the cell. The lithium foil will be placed inside the current collector and will face the Au cantilever.
- The lithium foil will be cut using the scissors that labeled “Lithium”. The length and width of the piece of lithium foil should be measured to make sure it is 3.9 mm wide by 22 mm long. Then it will be placed inside the current collector.
- After the lithium foil is screwed into the current collector, it should be bent halfway to the end of the current collector and fold it down so it is parallel with the Au cantilever using the tweezers labeled “Lithium”. The lithium foil is very malleable and should be bent in the shape of an upside down “L”. This decreases the distance from the Au cantilever to the lithium foil.
- The quartz window should then be placed over the side of the cell closest to the lithium foil followed by the back stainless-steel plate.
- Another quartz window will be placed over the side of the cell closest to the Au cantilever, followed by the front stainless-steel plate.
- The cell should resemble the one in Figure D7, but it will not have the electrolyte inside. It should also only have one PTFE barbed adapter (or PTFE plug).
- The electrolyte will be inserted into the cell after this. All the electrolytes in the glovebox are labeled with the concentration of the salt/solvent used and the date that it was made. They are also wrapped in aluminum foil to prevent oxidation of the salts. Electrolytes are discarded after three months.
- Place a 10 mL syringe into the electrolyte of interest. There will be an exposed inlet on the side that no PTFE plug or adapter was screwed into the cell. The tip of the syringe should be placed into this hole and fill the cell with 10 mL of electrolyte solution.

- After the cell has been filled with electrolyte solution, the PTFE barbed adapter or plug should be screwed into the cell. If the PTFE barbed adapters are used, the tubing should be placed over the adapters and use the tube clamps to seal the tubing. If the cell is being used in a Li-O_2 configuration, it should resemble the cell in Figure D7 below.

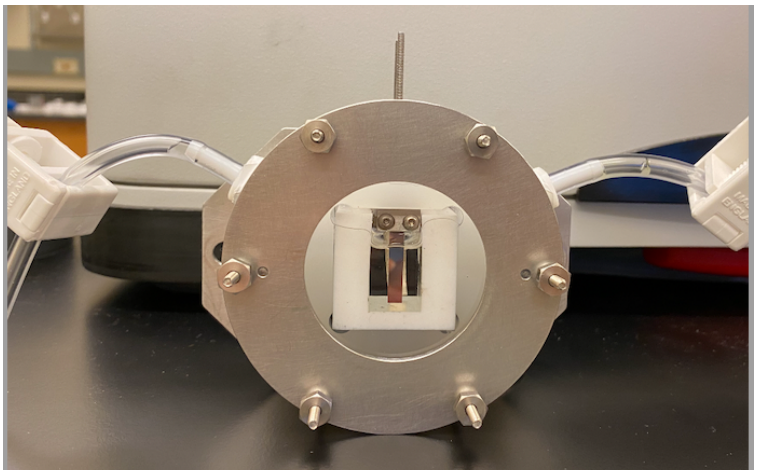

Figure D7: Image of assembled cell

- Remove the custom cell and the used syringe form the glovebox by opening the small antechamber door.

  *After vacuuming the glovebox, the antechamber will still contain argon unless it was opened from the outside after vacuuming the components.

- Open the small antechamber door from outside the glovebox. If the cell is being used in Li-ion configuration, then the area of the cantilever immersed in the electrolyte solution level can be determined. This will be discussed in detail later. If it is being used in Li-O_2 configuration, it will be saturated with oxygen first.

Oxygen Saturation for the Li-O_2 Battery Configuration

- Before saturating the cell with oxygen, the compressed gas training certification should be up to date. The custom cell, a beaker with water, and two 10 mL plastic pipet tips should then be taken into room 238.
- The custom cell should be placed onto the table located by the oxygen regulator.

- The custom cell, the flowmeter, and the oxygen regulator all have the same size tubing and connections to match this tubing size. Before turning on the oxygen, a plastic pipet tip should be placed into the tubing connected to the oxygen regulator. This should be connected to the inlet of the flowmeter. Another pipet tip should be placed into the outlet tubing of the flowmeter and be placed into the beaker full of water as shown in Figure D8. This prevents excess oxygen from accumulating in room 238.

Figure D8: Image of the flowmeter inlet and outlet tubing

- To turn on the oxygen tank, the valve connected to the ultra-high purity oxygen tank should be opened. The pressure of the regulator should be increased to approximately 5 psig by using the blue dial on the regulator as shown in Figure D9. After doing this, the small valve under the regulator should be opened to release oxygen. The flowmeter will begin to measure the oxygen flowrate.
- Once the oxygen begins to be released, the pressure will begin to drop. The outflow pressure can be monitored by looking at the pressure gauge in Figure D9 labeled “A”. The pressure gauge in Figure D9 labeled “B” monitors the pressure inside the tank.
- The pressure gauge should be increased to approximately 2 to 3 psig to make sure the oxygen is slightly above atmospheric pressure. This is required for the oxygen to flow out

of the tank. The flowmeter should be monitored to make sure that the oxygen outflow pressure on the regular remains around 2 to 3 psig and the oxygen flowrate is 45 mL/min.

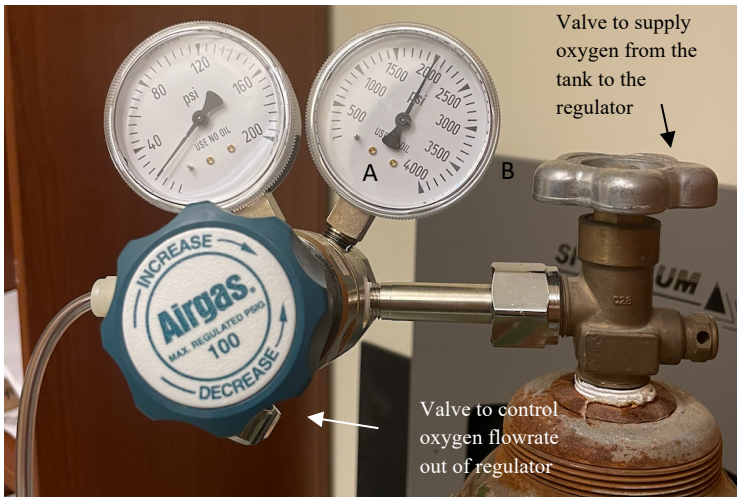

Figure D9: Image of ultra-high purity oxygen tank with regulator

- After the oxygen flowrate becomes stable at 45 mL/min, the plastic pipet tip should be removed from the tubing connected to the flowmeter and placed into the tubing connected to the custom cell.
- After the pipet tip has been placed in the tubing connected to the custom cell, the top of the tube clamp connected to the tubing with the plastic pipet tip should be slowly unscrewed.
- After the tube clamp has been opened at least halfway, bubbles should begin to form inside the electrolyte. Then the tube clamp connected to the outlet tubing should be slightly unscrewed. This should release pressure associated with the oxygen flow inside the cell.
- The opening of both the tube clamps connected to the inlet and outlet tubing should be tuned until the oxygen bubbling is very controlled and the bubbles are forming very slowly (1 bubble formed every 2-3 seconds).
- Throughout this process the flowrate of the oxygen is still at 45 mL/min and the tube clamp connected to the outlet tubing has been opened slightly to prevent pressure from accumulating from inside the cell.

- The process of opening the tube clamps to make sure the flow of oxygen is consistent (as seen by the bubble formation) should take approximately 1 minute at most.
- A timer should be started to completely saturate the electrolyte solution with oxygen for 45 minutes. Do not walk away from the cell after this or anytime that the tank is releasing oxygen.
- After 45 minutes, both tube clamps should be tightened completely and the plastic pipet tip should be removed from the inlet tubing (can be either side of the cell- they are the same). The plastic pipet tip should be placed back into the inlet tubing for the flowmeter and another pipet tip should be placed into the outlet tubing. The outlet tubing should be connected to the beaker full of water.
- The valve used to control the flowrate of oxygen out of the regulator should be closed, and the regulator pressure should be decreased using the dial on the regulator. After this, the valve on top of the oxygen tank should be closed. The flowrate on the flowmeter should be at 0 mL/min.

Determination of the Active Area of the Cantilever immersed in the Electrolyte

- There are two aluminum breadboards that are being used for the custom cell. One is on the optical table while the other is beside the computer and is attached to a steel rod and is shown in Figure D10.
- The custom cell should be screwed into the aluminum breadboard connected to the steel rod by the computer.
- Then, the USB camera should be connected to the computer and the camera application should be opened.
- After this, images should be taken of the cantilever using the camera. These images are usually split between two separate images. One image is of the top of the cantilever to the

bottom of the electrolyte inlet/outlet hole. The other image is from the bottom of the electrolyte inlet/outlet hole to the bottom of the cantilever. The electrolyte inlet/outlet hole is very visible and is a good reference point for the camera.

- The camera has been calibrated to obtain the pixel to length ratio by using a calibration card. This will supply the length to pixel ratio. The camera is calibrated every two weeks.
- The pixel to length ratio should be used to obtain the length of the cantilever immersed in the electrolyte solution.

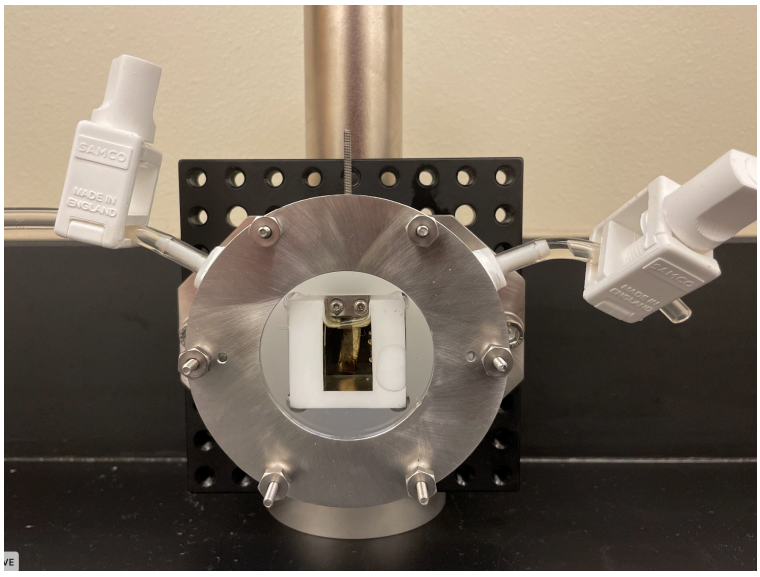

Figure D10: Image of assembled cell on aluminum breadboard

Placing the Custom Electrochemical Cell on the Optical Table

- As mentioned previously, there are two aluminum breadboards used for the custom cell. One always remains on the optical table and is not moved.
- The custom cell should be screwed into the aluminum breadboard on the optical table. The fourth screw hole from the top of the breadboard should be used.
- Then, the kSA MOS software should be turned on and the beams should be aligned onto the surface of the cantilever as defined in the kSA MOS SOP in Appendix C.
- There are three fine adjustments that will be used to align the beams onto the surface of the cantilever: the Z translator that controls the position of the custom cell which respect to the

optical table, and the Tip/Tilt and Rotation Stage. This stage is able to tip, tilt, and rotate the cell at a maximum angle of 4 degrees. The rotation knob is not needed since the cantilever should be perpendicular to the optical table.

- The Y axis is controlled by the fine adjustment knob in Figure D11 and the X axis is controlled by the fine adjustment knob also shown in Figure D11.

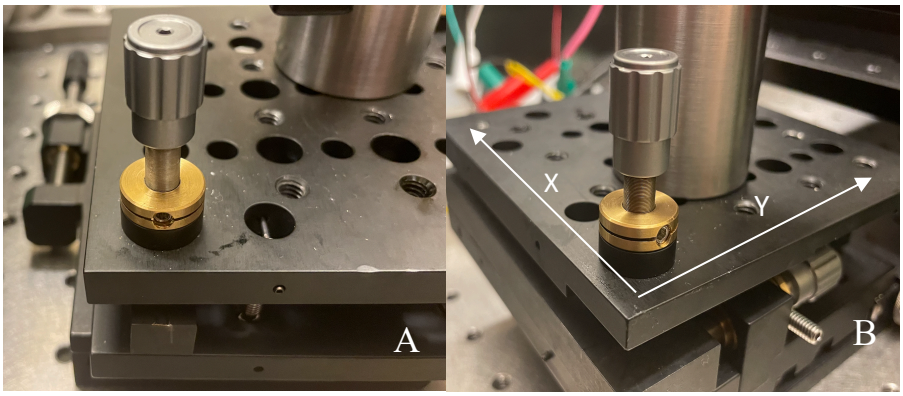

Figure D11: Image of fine adjustments knobs on tip/tilt and rotation stage

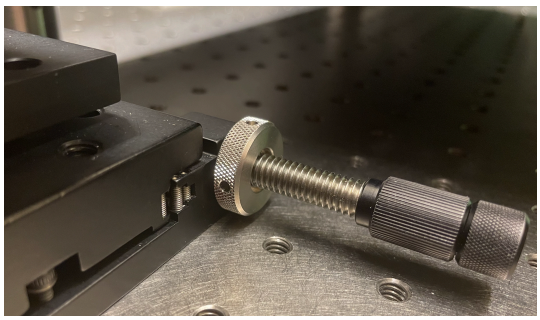

Figure D12: Image of the z translator

- After each of these knobs are used to align the beam array onto the surface of the cantilever, they should be locked. This is accomplished by tightening the screw on each of the screws on each of the knobs with a hex key.
- After the beams are aligned and the knobs are locked, the banana clips should be placed on the electrical connections. The electrical connections are the stainless-steel rods sticking out of the cell as shown in Figure D13.
- The red banana clip is the positive electrical connection and will be placed on the stainless-steel rod connected to the cantilever since the cantilever is the working

electrode. The green banana clip is the negative connection and will be attached to the stainless-steel rod connected to the lithium foil.

- After the connections are placed, the experiment can be started.

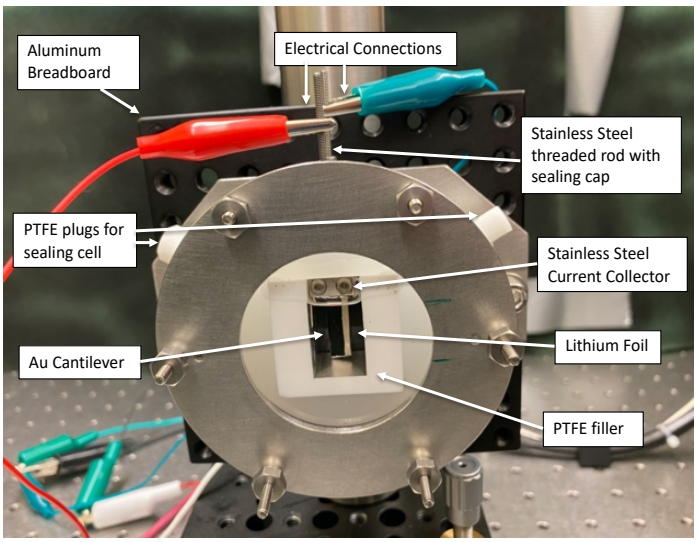

Figure D13: Image of the assembled cell on the optical table

Important Notes:

- The optomechanics should always be locked before starting the experiment.
- Always make sure that the banana clips are far enough away from each other so they do not come into contact and short-circuit the cell during the experiment.
- Make sure that the laser is on sign is placed on both doors before running an experiment
- **Never** touch the surface of the quartz window without gloves.

Chemicals

- Organic Solvents and lithium salts will be used to make the electrolyte solution. All solvents and salts are stored in the glovebox and are not removed. The lithium salts should never be exposed to moisture. The lithium salts and organic solvents used for Li-O_2 experiments are listed below.

Diethylene glycol dimethyl ether (Diglyme)

- **GHS categories**: Flammable Liquid (Category 3), Reproductive Toxicity (Category 1B)
- **GHS Symbols:** Flammable liquid, may damage fertility or cause harm to an unborn child

Dimethyl sulfoxide (DMSO)

- **GHS categories**: Flammable Liquid (Category 4)
- **GHS Symbols:** Flammable liquid

Lithium nitrate salt

- **GHS categories**: Oxidizing Solids (Category 3), Oral Acute Toxicity (Category 4), Eye Irritation (Category 2A)
- **GHS Symbols:** Oxidizer (may intensify a fire), harmful if swallowed, could cause serious eye irritation

Bis(trifluoromethane)sulfonimide lithium salt

- **GHS categories**: Skin Corrosion (Category 1B), Acute Oral Toxicity (Category 3), Acute Dermal Toxicity (Category 3), Eye Damage (Category 1), Specific Target Organ Toxicity-Repeated Exposure: Oral and Nervous System (Category 2), both Short and Long Term Aquatic Hazard (Category 3).
- **GHS Symbols:** Toxic if swallowed or if it comes into contact with skin, can cause severe burns and eye damage, can cause damage to organs through prolonged exposure if swallowed, harmful to aquatic life.

Equipment

Compressed Ultra-High Purity Oxygen Tank

- **GHS categories**: Compressed gas, oxidizing gas

- **GHS Symbols:** May cause or could intensify a fire

Custom Electrochemical Cell- PCTFE body with a stainless-steel front and back plate

- **GHS categories**: No hazardous components
- **GHS Symbols:** None

Storage

Always make sure that all solvents and salts used remain in the glovebox at all times and nitrile gloves are always used.

Diethylene glycol dimethyl ether (Diglyme)

Incompatibility: Keep away from heat and all ignition sources.

Storage Conditions: Keep in a dry, cool, and well-ventilated place. Keep container tightly closed. Take measures to avoid static discharge. Always wear gloves when using this and dispose of it in the solvent container labeled diglyme. These containers are stored in the glovebox and under the fume hood.

Dimethyl sulfoxide (DMSO)

Incompatibility: Keep away from heat and all ignition sources.

Storage Conditions: Keep in a dry, cool, and well-ventilated place. Keep container tightly closed. Take measures to avoid static discharge. Always wear gloves when using this and dispose of it in the solvent container labeled DMSO. These containers are stored in the glovebox and under the fume hood.

VITA

Hannah Dykes

Candidate for the Degree of

Master of Science

Thesis: IN SITU STRESS EVOLUTION ON AN Au THIN FILM CATHODE ELECTRODE DURING DISCHARGING/CHARGING IN LITHIUM-OXYGEN BATTERIES

Major Field: Chemical Engineering

Biographical:

Education:

Completed the requirements for the Master of Science in Chemical Engineering at Oklahoma State University, Stillwater, Oklahoma in December, 2021.

Completed the requirements for the Bachelor of Science in Chemical Engineering at University of Kentucky, Lexington, Kentucky in 2019.

Experience:

August 2021-Present	Process Engineer at CP Kelco
August 2019-Present	Graduate Research Assistant at Oklahoma State University
October 2017-June 2019.	Undergraduate Research Assistant at the University of Kentucky
May 2017-August 2017	Research and Development Intern at Valspar Paint Corporation

Professional Memberships:
American Institute of Chemical Engineers and The Electrochemical Society